HARVARD UNIVERSITY
Graduate School of Arts and Sciences

DISSERTATION ACCEPTANCE CERTIFICATE

The undersigned, appointed by the

School of Engineering and Applied Sciences

have examined a dissertation entitled

"Imaging and manipulation of nanoscale materials with coaxial and triaxial AFM probes"

presented by Keith A. Brown

candidate for the degree of Doctor of Philosophy and hereby certify that it is worthy of acceptance.

Signature Howard A Stone

Typed name: Prof. H. Stone

Signature R M Westervelt

Typed name: Prof. R. Westervelt

Signature Vinothan N. Manoharan

Typed name: Prof. V. Manoharan

Date April 22,2011

Imaging and Manipulation of Nanoscale Materials with Coaxial and Triaxial AFM Probes

A dissertation presented

by

Keith Andrew Brown

to

The School of Engineering and Applied Sciences

in partial fulfillment of the requirements
for the degree of
Doctor of Philosophy
in the subject of
Applied Physics

Harvard University
Cambridge, Massachusetts

May 2011

ProQuest LLC
789 East Eisenhower Parkway
P.O. Box 1346
Ann Arbor, MI 48106-1346

Thesis advisor

Robert M. Westervelt

Author

Keith Andrew Brown

Imaging and Manipulation of Nanoscale Materials with Coaxial and Triaxial AFM Probes

Abstract

The atomic force microscope is a powerful tool that allows a user to position a sharp tip with molecular-scale resolution and measure forces 1000× smaller than a single covalent bond. The strength of this technique comes from the combination of high spatial resolution from a nearly atomically sharp tip and exquisite force sensitivity from a flexible cantilever. While this technique is widely applied, the large size of the cantilever and cone present limitations. The spatial resolution of imaging is hindered by long range interactions, especially in the presence of electrostatic forces. Manipulation of particles is limited as particles tend to cluster and become irreversibly adhered to the probe.

Coaxial AFM probes improve the imaging and manipulation capabilities of AFM by creating a highly confined dipolar electric field. A coaxial AFM probe consists of a core electrode with a grounded shell. The capacitor created on the cantilever by these electrodes provides a method to electrostatically drive the mechanical mode of the cantilever with high fidelity, enabling high frequency driving. The improvement in spatial resolution when imaging is apparent when imaging work function by Kelvin probe force microscopy. We demonstrate an order of magnitude improvement in spatial resolution over conventional probes. Coaxial probes also generate strong

forces through dielectrophoresis (DEP), the force on an induced electric dipole. We demonstrate enhanced spatial resolution non-contact imaging using DEP to image sample topography and dielectric properties. DEP can also be used for manipulation, we perform pick-and-place assembly of microscopic objects using a coaxial probe.

We developed triaxial AFM probes for non-contact manipulation of nanoparticles as contact would lead to particle sticking. Triaxial probes with three concentric electrodes can trap a single nanoparticle using negative DEP in an attractive region surrounded by a repulsive region to avoid clustering. We used a triaxial probe as a nanoscale hand to grab a single nanoscale particle out of suspension, hold it without contact, move it relative to the probe, and release it. Triaxial probes are promising candidates for nanoassembly and imaging with interchangeable tip functionality.

Contents

List of Figures

List of Variables

Variable	Description
a	Radius of a spherical particle
A	Mechanical oscillation amplitude of a cantilever
C	Capacitance
D	Insulating layer thickness of a capacitor
δ	Deflection profile of a cantilever
$\boldsymbol{E}$	Electric field
E_{BD}	Maximum electric field possible before dielectric breakdown
ϵ_0	Permittivity of free space, 8.85×10^{-12} F/m
ϵ	Relative permittivity
$\tilde{\epsilon}$	Complex permittivity
f	Frequency
f_0	Principle mechanical resonance frequency of a cantilever
$\boldsymbol{F}$	Force
G_S	Surface conductance of a nanoparticle
η	Voltage ratio in triaxial AFM tweezers
H	Cantilever thickness
k	Spring constant
k_B	Boltzmann's constant, 1.38×10^{-23} J/K
K	Classius-Mosotti factor
L	Cantilever length
λ	Insulator thickness of a coaxial or triaxial probe
μ	Dynamic viscosity of a fluid

ν	Poisson's ratio
$\boldsymbol{p}$	Electric dipole moment
ϕ	Electrostatic potential
Φ	Work function
q	Electric charge
Q	Quality factor of a resonantor
R	Resistance
σ	Conductivity
t	Time
T	Temperature
$\overline{u}$	Cauchy strain tensor
U	Potential energy
$\boldsymbol{v}$	Velocity of a particle
V	Voltage
W	Cantilever width
x	Position coordinate
y	Position coordinate
z	Tip-sample separation
ω	Angular frequency, $\omega = 2\pi f$

Acknowledgments

I am enormously grateful for everyone that has contributed to my PhD.

First and foremost, I would like to thank my advisor, Bob Westervelt. I hope his deep physical intuition, appreciation for clarity, and relentless support continue to shape my experience in science. I also benefited greatly from interactions and support from Howard Stone, Vinny Manoharan, and Kit Parker.

I consider David Issadore, Jesse Berezovsky, and Will Oliver to be mentors as they taught me how to approach problems. The support and friendship of Erin Boyd, Alex Nemiroski, and Halvar Trodahl was indispensable. I am also indebted to those I worked with, including Jonathan Aguilar, Sarah Griesse-Nascimento, Joshua Bridger, Joe Childs, Kevin Satzinger, and Ben Yang who is taking up the cause.

The staff at Harvard is the greatest resource I took advantage of in my time there. Jim MacArthur has been a constant source of wisdom and friendship. JD Deng taught me everything I know about atomic force microscopy. Naomi Brave, Kathryn Hollar, Noah Clay, and the staff at CNS have helped greatly.

I have benefited greatly from numerous collaborations, including Keith Jones, Ryan Fuierer, and Maarten Rutgers at Asylum Research, Donna Hurley and Jason Killgore at NIST, Christophoros C. Vassiliou and Michael Cima at MIT, and Rafael Jaramillo at Harvard.

None of this would be possible without the funding that has supported my research. I would like to acknowledge the Air Force for support through the NDSEG fellowship program, the National Cancer Institute who funds the MIT-Harvard Center of Cancer Nanotechnology Excellence and the Department of Energy through grant number DE-FG02-07ER46422.

I could not possibly have lasted through graduate school without the constant support of my family and friends. My parents, Robert and Beverly, have unconditionally stood by me and let passion be my guide. My friends, Pals, and Free Parking kept me sane. Finally to my future wife Rebecca, you have helped me in more ways than I can list and I owe much to your contributions.

For Rebecca

Chapter 1

Introduction

Semiconductor technology represents a triumph of nanotechnology as the steadily improving state of the art has permeated every aspect of daily life.[1] In addition to the miniaturization and acceleration of CMOS logic from Moore's law, nanotechnology has given rise to structures whose quantum properties at the nanoscale provide novel functions. Exquisite nanoscale building blocks such as colloidal semiconductor quantum dots[2] and semiconductor nanowires[3] offer promising avenues to new classes of devices. The primary reason these quantum structures have not achieved the wide adoption of semiconductor technologies is that limitations persist in imaging and manipulating nanoscale materials on the length scales comparable with their size. One tool that has been enormously successful in imaging and manipulating nanoscale materials is the atomic force microscope (AFM).[4]

In this section, we overview the role of atomic force microscopy in nanotechnology and the limitations in imaging and manipulation with AFM. We present coaxial and triaxial AFM probes and show how they can be used to overcome limitations in AFM-based imaging and manipulation.

1.1 Imaging and Manipulation with Atomic Force Microscopy

The atomic force microscope (AFM) is an indispensable tool for imaging and manipulating nanoscale materials. Since its invention in 1986,[5] applications of atomic force microscopy have expanded from measuring topography to many other measurement modalities that measure properties such as such as contact potential difference,[6] chemical composition,[7] and local magnetic resonance.[8]

A central reason for the success of the AFM its simplicity and versatility. Figure 1.1 shows the operation of an AFM. A sharp tip (typical radius $\sim$ 5 nm) is brought close to the sample (typical tip-sample separation $\sim$ 50 nm) and experiences a force $\boldsymbol{F}$.[4] The force mechanically deflects the cantilever and this deflection is measured with an optical lever in which the deflection of a laser spot is measured with a 4-quadrant photodiode. Part of the reason for the extensive use of AFM is that it provides a simple way to position a nanoscale tip near a sample with nm-scale precision in all three dimensions while measuring and applying pN-scale forces.[4] A further reason why AFM is so versatile is it can operate in many environments such as ambient, ultra high vacuum, and in liquid.

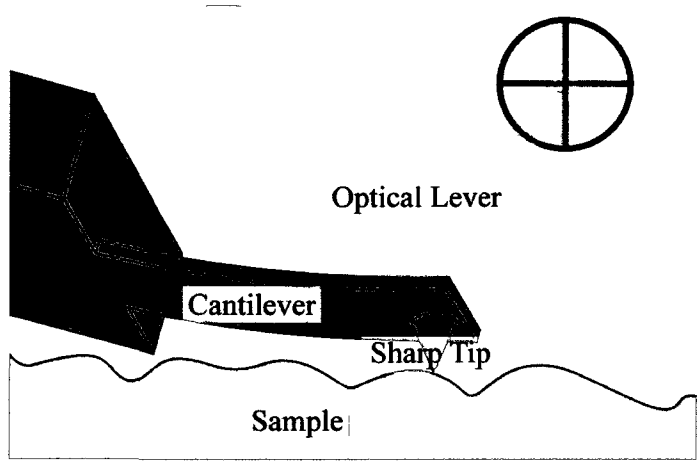

Figure 1.1: Schematic depicting operation of an atomic force microscope (AFM). A sharp tip is brought near a sample and the interaction force is measured by monitoring the deflection of a cantilever with an optical lever in which a laser spot is focused on the cantilever and the motion of the reflected beam is detected by a four quadrant photodiode.

1.1.1 Long range of the electrostatic interaction

One area where AFM has been particularly successful is in measuring electrical properties of samples.[9, 10, 11] Measuring electrostatic forces with AFM is considered electrostatic force microscopy (EFM), a term which encompasses many subdivisions and applications.[9] Many measurement modalities have been developed such as Kelvin probe force microscopy (KPFM) to measure local work function,[6] piezoresponse force microscopy (PFM) to measure the local piezoelectric constants,[12] and scanning impendence microscopy (SIM) to measure the local impedance of a sample.[13]

The limitations inherent in AFM-based electrical measurements are illustrated by the electrostatic simulation in Figure 1.2(a).[14, 15] Here, we use an an axisymmetric finite element simulation to find the electrostatic potential ϕ near a conducting AFM probe above a conducting sample. The probe is held at 1 V while the sample at the

bottom of the image is grounded. The color scale shows the electrostatic potential ϕ. The image shows spatial variations of ϕ in all parts of the image, which indicates the presence of local electric fields $\boldsymbol{E}$. This picture highlights the challenge of performing high spatial resolution EFM with an AFM probe. The long-range nature of the electrostatic interaction dictates that there will be contributions from the entire cone as well as the cantilever. The net result is that the spatial resolution of a measurement will not be given by the tip radius of the probe, the dimension that can be made the smallest, but by the macroscopic geometry.

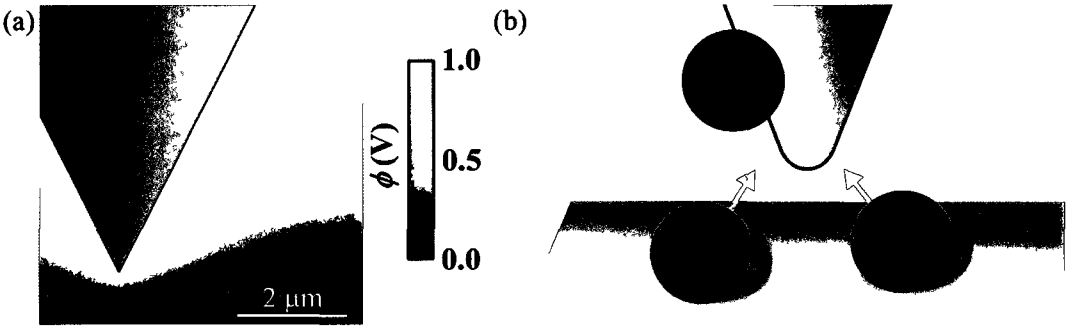

Figure 1.2: (a) Electrostatic simulation depicting the long range of the electrostatic interaction. The electrostatic potential ϕ is found with axisymmetric finite element simulation (Maxwell 2D – Ansys). The probe is held at 1 V and the sample at the bottom of the image is grounded. The spatial variation of ϕ indicates the presence of electric field in the entire region. (b) Illustration of the challenges in AFM-based nanoassembly. Particles adhered to the probe will be difficult to remove due to the "sticky finger" problem while long range attractive forces will lead to clustering of nearby particles preventing single particle manipulation.

1.1.2 Sticking and clustering of nanoparticles

In addition to imaging materials, AFM has proved to be a powerful tool for manipulation of nanoscale materials. A famous example of tip-based assembly was the demonstration of single-atom assembly in which Don Eigler and Erhard Schweizer

patterned the letters 'IBM' in adsorbed xenon atoms using a scanning tunneling microscope (STM).[16] In addition, many people have performed assembly with AFMs in ambient conditions by pushing and sliding particles along surfaces.[17, 18, 19, 20] AFM has also been used to pattern materials by scanning probe lithography[21] and to directly deposit materials directly with techniques like dip pen nanolithography.[22, 23] More recently, two coordinated AFM probes have been used as tweezers to pick-and-place single microscopic beads.[24, 25]

Despite successes, two challenges, illustrated in Figure 1.2(b), limit pick-and-place assembly by AFM to microscale particles or larger. Firstly, adhesive forces such as the surface tension from a capillary neck and van der Waals attraction have magnitudes proportional to the particle radius.[26, 27, 28, 29] In contrast, body forces such as di-electrophoresis, the force on an induced electric dipole, have magnitudes proportional to particle volume. As particles get smaller, adhesive forces dominate and particles tend to become irreversibly attached to surfaces. This is known as the "sticky finger" problem and for nanoparticles, non-contact assembly methodologies are necessary. The second problem is that attractive forces such as van der Waals will act on all local particles which will lead to clustering and prevent precision manipulation of a single particle.

1.2 Coaxial and Triaxial AFM Probes for Nanotechnology

Coaxial and triaxial probes can overcome the challenges inherent in imaging and manipulating nanoscale particles. Figure. 1.3 illustrates coaxial and triaxial AFM probes and defines the nomenclature we use to refer to them. A coaxial probe consists of a core electrode separated from a shell electrode by an insulating layer. A triaxial probe has three concentric electrodes: a core electrode surrounded by inner and outer shell electrodes.

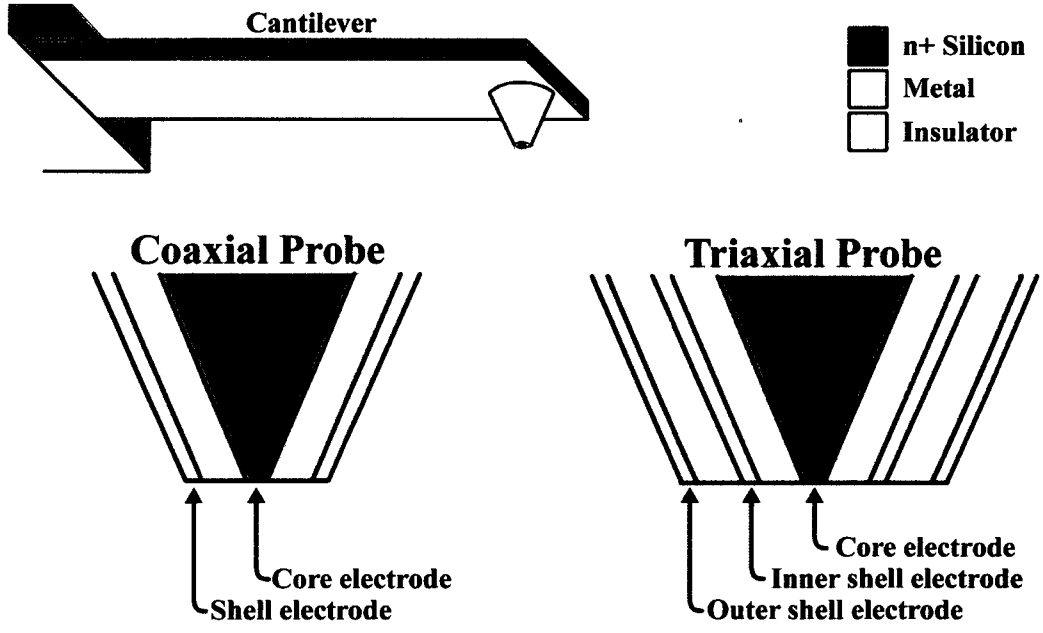

Figure 1.3: Schematic diagram of coaxial and triaxial AFM probes. Coaxial or triaxial electrodes are created on a conical tip at the end of a cantilever. Cross sections of coaxial and triaxial probe are shown along with the naming convention for the electrodes. The colors correspond to different materials with grey representing heavily doped silicon, gold corresponding to metal, and cyan corresponding to an insulating layer.

Coaxial probes address the long range of the electrostatic interaction by shielding the electrostatic interaction, as shown in Figure 1.4(a). The shell electrode confines the electric field causing the electric field to be strongly localized to the region at the tip of the probe. Further, the size of the coaxial probe can be chosen through fabrication to address a specific application.

Triaxial probes can trap and hold single nanoscale objects without contact using negative dielectrophoresis (nDEP), as shown in Figure 1.4(b). A triaxial probe acts analogously to a nanoscale hand that can grab, hold, image with, and release a specified nanoparticle. The non-contact nature of the trapping allows the sticky finger problem to be avoided. The particle is held in an attractive trap surrounded by a repulsive region, preventing clustering of many particles.

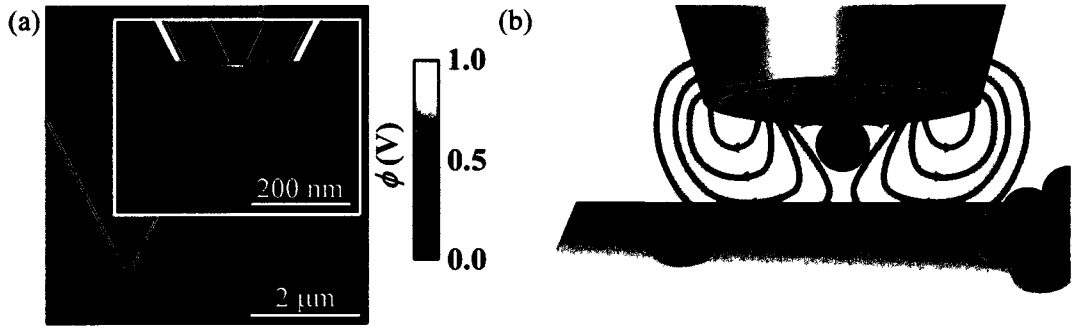

Figure 1.4: (a) Coaxial AFM probes create a highly localized electric field, as shown by the spatial confinement of the electrostatic potential ϕ. This axisymmetric electrostatic simulation shows a coaxial probe where the core electrode is held at 1 V and the shell electrode is grounded. Coaxial probes completely remove the electrostatic effect of the cone and cantilever and can be made in different sizes for a specific application. (b) Schematic of a triaxial probe holding a single nanoparticle without contact with negative dielectrophoresis (nDEP). A voltage is applied to the inner shell electrode while the core and outer shell electrodes are grounded. The resulting electric field has a zero in which a particle less polarizable than the medium will rest. Further particles are held away from the nDEP trap as the interaction is repulsive.

1.2.1 Previous use of coaxial AFM probes

AFM probes with a ground shield have been employed for a number of years for their ability to create spatially confined electric fields. The earliest use of such probes has been high frequency applications such as scanning near-field microwave microscopy and near field optical microscopy.[30, 31, 32, 33] Shielded probes have also been used for electrochemical imaging.[34, 35, 36, 37] Probes with a core-shell geometry have been used as a system to deliver materials with electroosmosis, a tool named the nanofountain probe.[38] The idea of using coaxial probes for dielectrophoresis originated from a similar device in which opposing sides of a glass capillary were coated in metals and cells were trapped at its tip.[39] The first demonstration of dielectrophoresis with coaxial probes was performed in liquid where yeast cells were trapped at the tip of a coaxial AFM probe.[40]

1.2.2 Outline of the thesis

This thesis contains six Chapters which describe our design, development, and use of coaxial and triaxial AFM probes to image and manipulate nanoscale systems.

Chapter 2 "Electrostatics and Mechanics of Coaxial AFM Probes" provides a theoretical basis for the work done in this thesis. We present an overview of cantilever dynamics, an electrostatic model of coaxial probes, and derivation of the dielectrophoretic and capacitive forces.

Chapter 3 "Fabrication of Coaxial and Triaxial AFM Probes" outlines the fabrication and testing of coaxial and triaxial AFM probes. The chip holder based

fabrication is described along with an example fabrication protocol and variants of the protocol.

Chapter 4 "Self-Driving Capacitive Cantilevers" explores the use of the capacitor on the surface of a cantilever to actuate the mechanical mode of a cantilever electrostatically. The mechanical mode is driven with high fidelity owing to the local nature of the driving. We find the characteristics of electrostatic driving to agree with our model of the effect and we demonstrate topographic imaging while driving the cantilever electrostatically.

Chapter 5 "High Resolution Kelvin Probe Force Microscopy with Coaxial Probes" demonstrates how coaxial AFM probes can be used to perform electrostatic force microscopy with enhanced spatial resolution. The field confinement imposed by coaxial probes affords enhanced spatial resolution by completely removing the electrostatic effect of the cone and cantilever. We demonstrate high spatial resolution electrostatic imaging by performing Kelvin probe force microscopy (KPFM) with coaxial probes.

Chapter 6 "Dielectrophoretic Imaging and Manipulation with Coaxial Probes" explains how coaxial probes can be used to image and manipulate materials with dielectrophoresis. We find the electric field produced by a coaxial probe to be well approximated by the electric field of an electric dipole. We demonstrate imaging with dielectrophoresis and discuss how this can be used to image topography and dielectric properties with high resolution. We also show that coaxial probes can function as nanoscale pick-and-place tool and demonstrate three dimensional assembly of microscale objects.

Chapter 7 "Triaxial AFM Probes for Non-Contact Trapping and Manipulation"

demonstrates how triaxial probes can trap single nanoparticles in suspension using negative dielectrophoresis. Triaxial probes avoid the sticky finger problem by holding a nanoparticle without contact and by surrounding a trapped particle with a repulsive region, clustering is avoided.

Chapter 2

Electrostatics and Mechanics of Coaxial AFM Probes

2.1 Introduction

In order to understand the effect of applying voltages to the electrodes of a coaxial or triaxial AFM probe, it is necessary to consider both electrostatic and mechanical effects. In this Chapter, we describe the electrical and mechanical theory of coaxial and triaxial probes. We begin by presenting a mechanical model of a cantilever. Then, we describe a circuit element model of a coaxial probe. Next, we discuss the electrostatic forces relevant to coaxial probes, including the force on capacitors and the dielectrophoretic force. Finally, we overview other effects pertinent to coaxial and triaxial probes including adhesive forces, electrohydrodynamic effects, and dielectric breakdown.

2.2 Cantilever Dynamics

Cantilevers, such as the cantilever of a coaxial probe, are the force sensing element in an AFM. The dynamics of cantilever motion can be solved by applying the Euler-Bernoulli theory of beam deflection to find the deflection δ at a location x on the cantilever,[41]

$$YI\frac{\partial^4\delta}{\partial x^4} + \rho A_C \frac{\partial^2\delta}{\partial t^2} = 0, \tag{2.1}$$

were Y is the Young's modulus of the material, I is the area moment of inertia, ρ is the density, and A_C is the cross sectional area of the cantilever. For a cantilever of length L with a rectangular cross section of width W and thickness H as depicted in Figure 2.1(a), $I = WH^3/12$ and $A_C = HW$. The deflection profile $\delta(x)$ shown schematically in Figure 2.1(b) can be found by solving Eq. (2.1) with the boundary conditions $\delta(0) = 0$, $\delta'(0) = 0$, $\delta''(L) = 0$, and $\delta'''(L) = 0$. The presence of thin film coatings on an AFM cantilever do not seriously affect the dynamics.[35] If the cantilever is operating in fluid. there are additional considerations due to the viscosity of the medium and the added mass effect but we do not consider cantilever dynamics in fluid in this thesis.[42]

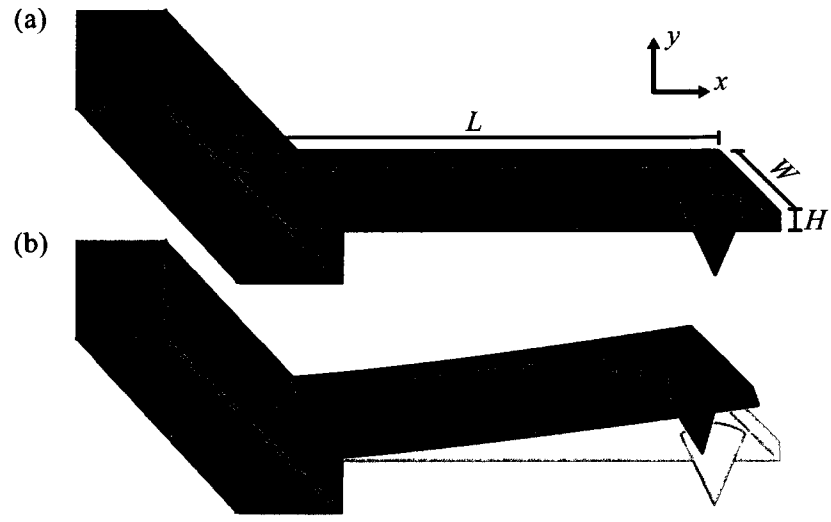

Figure 2.1: (a) An AFM cantilever with rectangular cross section of width W, length L and thickness H. (b) The cantilever deflects in response to an applied force, the deflection profile is given by $\delta(x)$.

Static deflections are rarely used in AFM experiments as they are subject to drift and wear the tip considerably. Instead, operating at AC near a mechanical resonance of the cantilever is preferred. While a cantilever is host to an infinite number of mechanical resonances, the principle harmonic is most convenient to use as mechanically driving becomes more challenging at higher frequencies. The deflection profile of the first mechanical mode is given by,[41]

$$\delta(x) = \delta_0 \left([\cos \kappa_1 x - \cosh \kappa_1 x] - \frac{\cos \kappa_1 L + \cosh \kappa_1 L}{\sin \kappa_1 L - \sinh \kappa_1 L} [\sin \kappa_1 x - \sinh \kappa_1 x] \right), \quad (2.2)$$

where the wavenumber $\kappa_1 = 1.875/L$. The angular frequency of the first mechanical resonance is given by,[41]

$$\omega_1 = \left(\frac{1.875}{L} \right)^2 \sqrt{\frac{YH^2}{12\rho}}. \quad (2.3)$$

Throughout this thesis we will use both frequency f and angular frequency ω, with the understanding that $\omega = 2\pi f$.

The interaction between an AFM probe and a sample is examined by considering the motion of the tip as a simple harmonic oscillator. The cantilever is modeled as a linear spring with spring constant,[41]

$$k = \frac{YH^3W}{4L^3}. \tag{2.4}$$

The effective mass $m^\star$ of the cantilever is found by equating $\omega_1 = \sqrt{\frac{k}{m^\star}}$ and is found to be $m^\star \approx 0.25m$ where $m = LWH\rho$ is the mass of the cantilever. The mass m_{tip} of the tip must also be included, giving rise to the resonance angular frequency of the tip,[41]

$$\omega_0 = \sqrt{\frac{k}{m_{tip} + 0.25LWH\rho}}. \tag{2.5}$$

Dissipative forces are also present in the form of mechanical dissipation in the cantilever, and more importantly, viscous drag in the air. These forces give rise to a finite quality factor $Q \approx 500$ in ambient conditions. If the tip is driven with a sinusoidal force given by, $F = F_0 \cos\omega t$, the resulting amplitude A of the tip motion is given by,

$$A = \frac{F_0}{k}\left[\left(1 - \frac{\omega^2}{\omega_0^2}\right)^2 + \left(\frac{\omega}{\omega_0 Q}\right)^2\right]^{-1/2}. \tag{2.6}$$

ω_0 is slightly shifted by the presence of dissipative forces manifesting as a finite Q, in practice with $Q \approx 500$, this is a 1 part in 10^6 correction.

The motion of the tip in amplitude-modulation (AM) AFM experiments can be understood by considering the effect of a tip-sample force F_{TS}.[43] In an AM-AFM experiment, the probe is driven with $F_0 \cos(\omega_0 t)$ and is observed to oscillate with a free space amplitude A_0 given by $A_0 = \frac{QF_0}{k}$. The tip-sample distance z is decreased until the amplitude decreases to a set point amplitude A_S. The effect of F_{TS} can be understood as adding a spring with a spring constant equal to $-\frac{dF_{TS}}{dz}$. The addition

of this spring will shift the resonance frequency of the probe and lower the amplitude as described in Eq. (2.6). If the probe is driven directly on resonance, the amplitude will be lowered by both attractive and repulsive forces, therefore the probe is typically driven slightly above or below resonance so that only forces of the appropriate sign will lower the amplitude, as depicted in Figure 2.2.

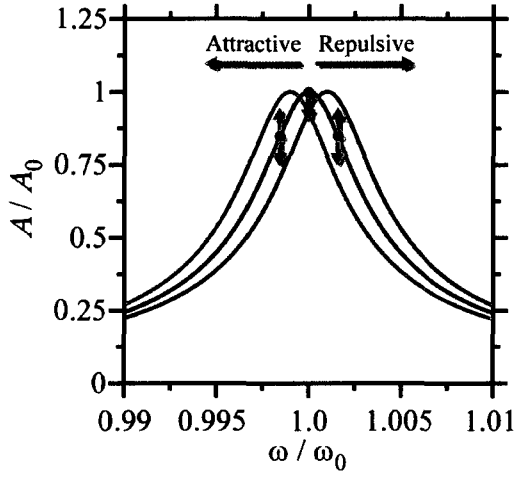

Figure 2.2: AFM amplitude as a function of detuning from the free space resonance frequency ω_0. The black curve represents the free space amplitude. If the tip is subjected to a repulsive or attractive force, the resonance frequency is shifted slightly up or down, respectively. If the tip is being driven on resonance, represented by the middle dot, both attractive and repulsive forces result in a decrease in amplitude. If the tip is driven at a frequency slightly lower than its resonance, represented by the left dot, only a repulsive force creates a decrease in amplitude, making this an ideal set point for operating in tapping mode. Consequently, driving at a frequency slightly higher than the resonance frequency is ideal for non-contact mode imaging.

The set point in AM-AFM, along with parameters of the probe, can provide an estimate for the maximum value of the tip-sample force F_{TS}. In cases when the force is conservative and only takes a significant value at the point in an oscillation closest

to the sample, the maximum tip-sample force can be written as,

$$F_{TS} \approx \frac{kA_0}{2Q}\sqrt{1 - \frac{A_S^2}{A_0^2}}. \tag{2.7}$$

The seemingly restrictive conditions for this estimate to be valid are very common in AM-AFM, particularly in tapping-mode AFM in which the amplitude is large and the dominant interaction is elastic indentation. This equation does not specify if the force is attractive or repulsive, so this must be inferred from other imaging conditions.[43]

2.3 Lumped Circuit Element Model of Coaxial Probes

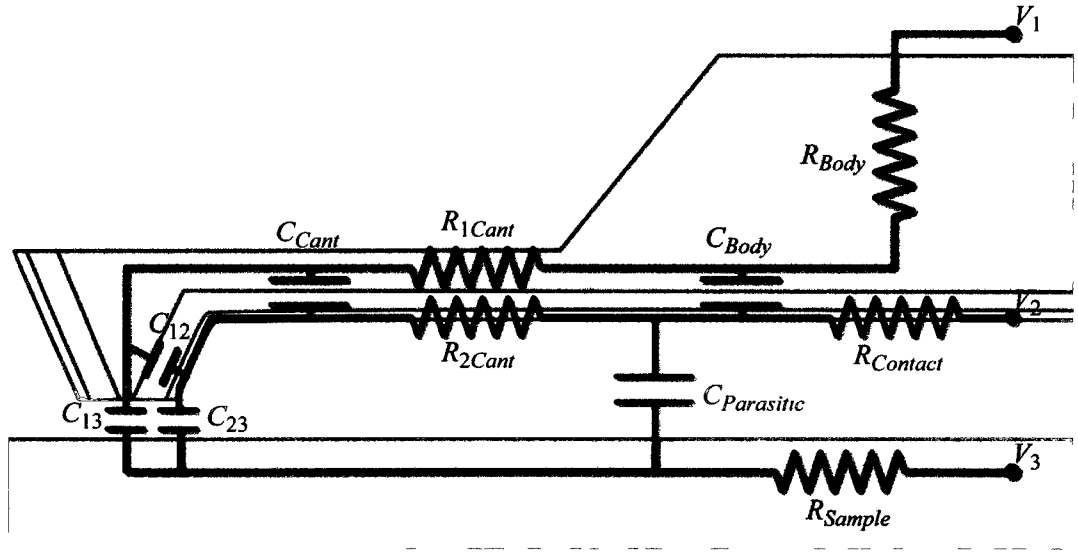

Figure 2.3: Lumped element circuit schematic of a coaxial probe near a sample. Voltages V_1, V_2, and V_3 are applied to the core electrode, shield electrode, and sample respectively. The system is parameterized by a network of resistors R and capacitors C whose values depend on the details of the system. The schematic is not to scale.

The electrical response of a coaxial probe to an applied voltage may be estimated using a lumped circuit model of the probe as shown in Figure 2.3. Electrical contact

to the core conductor is made through the body of the probe, which corresponds to the resistance R_{Body}. Voltage must also pass through the cantilever, which may be modeled by resistance R_{1Cant}. Contact to the shell electrode is made through the top metal film which must pass through the film on the body of the probe and cantilever which have resistances $R_{Contact}$ and R_{2Cant} respectively. The conductivity of the doped silicon that makes up the AFM probes is $\sigma_{Si} \approx 4 \times 10^3$ Sm^{-1}. Using σ_{Si} and typical dimensions for these probes, $R_{Body} \approx 10$ mΩ and $R_{1Cant} \approx 200$ Ω. Similarly, the gold of the shell electrode has a conductivity of $\sigma_{Au} \approx 5 \times 10^7$ Sm^{-1} and therefore a 30 nm thick layer has a sheet resistance of ~ 1 $\Omega\square^{-1}$. Typical gold films have $R_{Contact} \approx R_{2Cant} \approx 5$ Ω. Because the resistance of the metal film is so much lower, metalized probes are preferred for high frequency applications.

The capacitance between electrodes determines the maximum frequency that may be applied to the coaxial electrodes. The capacitance between the core and shell electrodes may be broken into three pieces:

1. C_{Body} - the capacitance from films on the body of the AFM chip.

2. C_{Cant} - the capacitance from films on the cantilever.

3. C_{12} - the capacitance from the films on the apex of the tip.

The total capacitance is dominated by C_{Body} which is typically ≈ 1 nF. This capacitance together with the total resistance determines the maximum frequency f_{RC} that will reach the coaxial probe through the RC-network that is formed by the lumped capacitor circuit. Steps should be taken to minimize this capacitance such as mini-

mizing the width of the metal pad on the AFM chip and using a thick low-k insulating layer. $f_{RC} = (2\pi RC)^{-1} \approx 15$ MHz for a typical probe.

The core-shell capacitance C_{Cant} from the cantilever has the interesting feature that it depends slightly on the deflection of the cantilever. This coupling between electrostatics and mechanics is what allows coaxial probes to mechanically oscillate by application of an electric field, an effect that will be explored further in Chapter 4. The core-shell C_{12} capacitance near the tip, along with the core-sample capacitance C_{13} and shell-sample capacitance C_{23}, is important in performing Kelvin probe force microscopy (KPFM) with coaxial probes and will be explored in further in Chapter 5. Triaxial probes may also be described by a lumped circuit element model by simply including another electrode and corresponding capacitors and resistors with parameters similar to those of the shell electrode.

2.4 Electrostatic Forces

Coaxial probes create strong and localized electric fields at their tip. This field can be used to image samples (Chapters 5-6) and to manipulate particles at the probe tip (Chapters 6-7). In addition, the field creates internal forces in the cantilever (Chapter 4). Here, we present the theoretical basis of the relevant forces that arise from an applied electric field.

Electric fields used in this work are applied at frequencies below 10 MHz, which corresponds to wavelengths greater than 30 m. Since the smallest wavelength is so much larger than the system, it is appropriate to use the electrostatic approximation. In the electrostatic approximation, electric fields instantly propagate through space.

Further, in the absence of a time-varying magnetic field, the electric field is curl-free and described by an electrostatic potential ϕ, defined such that $\mathbf{E} = -\boldsymbol{\nabla}\phi$.[44]

Electric fields $\boldsymbol{E}$ produce a myriad of effects, but the forces pertinent to this thesis are second order in $\boldsymbol{E}$. First order effects exist, such as the Lorentz force, electroosmosis, and the peizoelectric effect, but there are two ways in which first-order effects are mitigated. (1) By using an AC electric field in which $\langle \boldsymbol{E} \rangle = \mathbf{0}$, the time average of any first order effect is 0. If the period of the applied electric field is faster than the response time of the system, the system will not be able to react quickly enough for first order effects to contribute. This effect is most useful when considering motion of small particles in an electric field. (2) By looking at higher harmonics of the force, it is possible to exclude the possibility that first order effects are present. If a voltage $V = V_{DC} + V_{AC} \sin \omega t$ is applied to a system, linear effects will occur at DC and ω. Effects quadratic in V will also have a component at 2ω so by looking at 2ω, the presence of linear effects is ruled out.[45]

In a system of linear dielectrics with relative permittivity ϵ, the work required to assemble a system of charges is given by,[46]

$$U = \frac{1}{2} \int \epsilon_0 \epsilon \mathbf{E} \cdot \mathbf{E} dV, \tag{2.8}$$

where ϵ_0 is the permittivity of free space and the integral is a volume integral over all space. The integral only depends on the local electric field magnitude E as $\mathbf{E} \cdot \mathbf{E} = E^2$. The force acting on a particular degree of freedom, such as the z-coordinate of an object, is given by,

$$F_z = -\frac{1}{2} \frac{\partial}{\partial z} \int \epsilon_0 \epsilon E^2 dV. \tag{2.9}$$

It is usually intractable to approach Eq. (2.9) directly; alternatively two methods are commonly used to calculate the forces in electrostatic systems. The first method is to parameterize the system using the capacitive matrix formalism and examine forces in terms of changing capacitances. This method is most useful in examining the forces on macroscopic electrodes. We will discuss the capacitive method in Section 2.4.1. The second method is to examine the local forces on induced dipoles, which is referred to as dielectrophoresis (DEP). This method is most useful for analyzing the motion of small objects in macroscopic electric fields. We will discuss the dielectrophoretic method in Section 2.4.2.[47]

2.4.1 The capacitive force

The electrostatic energy in Eq. (2.8) may be expressed using the capacitance matrix formalism. A system of n electrodes is characterized by the capacitance matrix $\overline{C}$ is given by,[48]

$$C_{ij} = \begin{cases} -C_{ij} & i \neq j \\ C_{ii} + \sum_{k \neq i} C_{ik} & i = j \end{cases} \tag{2.10}$$

where C_{ij} is the capacitance between the ith and jth electrode and C_{ii} is the self capacitance of the ith electrode. Self capacitance is present whenever the field has a boundary condition infinitely far away and it can be thought of as the capacitance to a ground plane at infinity. If each electrode is now held at voltage V_i, the energy stored in the system is given by,

$$U = \frac{1}{2} \sum_{ij} V_i \overline{C}_{ij} V_j. \tag{2.11}$$

Here, $\overline{C}$ carries all the geometric information in Eq. (2.8) and U is completely specified by the voltages V_i.[48]

The capacitance matrix formalism is convenient for finding forces on electrodes or the macroscopic geometry. A given system is completely characterized by $\overline{C}$ and once this is calculated, the energy may be found for any voltages V_i. The capacitances can be solved analytically or by finite-element methods.

Subtlety of the capacitive force

While the capacitive matrix formalism is quite useful for describing the forces on macroscopic electrodes, care must be taken to correctly account for the sign of the forces.[46] If we consider a simple two-electrode system with capacitance C, the energy required to charge the capacitor to a voltage V is given by,

$$U = \frac{1}{2}CV^2. \tag{2.12}$$

This work is done by the battery or equivalent voltage source. The easiest way to derive the z-directed force on a system of electrodes is to hold charge q fixed, apply the transformation $q = CV$, and take the derivative with respect to z,

$$F_z = -\frac{\partial}{\partial z}\frac{1}{2}\frac{q^2}{C} = \frac{1}{2}\frac{q^2}{C^2}\frac{\partial C}{\partial z} = \frac{1}{2}V^2\frac{\partial C}{\partial z}. \tag{2.13}$$

If instead we hold V fixed, we get a result different by a sign from the above,

$$F_z = -\frac{\partial}{\partial z}\frac{1}{2}CV^2 = -\frac{1}{2}V^2\frac{\partial C}{\partial z}. \tag{2.14}$$

Of course, the instantaneous force on the electrodes cannot depend on the future state of q or V so this must be reconciled. The correct answer can be found by reasoning

that the positive and negative charges on opposing electrodes attract each other so the force should pull the electrodes together, as in Eq. (2.13). The reason Eq. (2.14) is incorrect is that holding V constant implies that the battery will do work on the system so it is insufficient to only consider the energy of the capacitor.

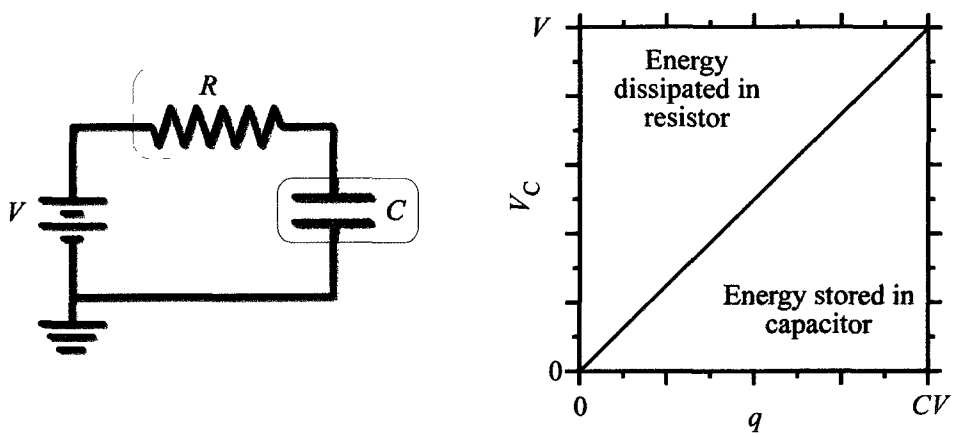

Figure 2.4: (left) Schematic of an RC system. (right) The energy liberated from the battery is broken into two equal parts, the energy dissipated in the resistor (orange), and the energy stored in the capacitor (cyan).

The constant-voltage system is reconciled by considering the energy change of the voltage source as well as the energy of capacitor. A simple RC system, as shown in Figure 2.4, is useful for explaining this. If the battery is connected at time $t = 0$, the charge on the capacitor can be found to follow $q = CV\left(1 - e^{-t/RC}\right)$ and the total energy dissipated in the resistor is found with $U_R = \int_0^\infty \frac{1}{R}\left(\frac{dq}{dt}\right)^2 dt$ to be $U_R = \frac{1}{2}CV^2$, independent of R. Since the energy stored in the capacitor is also found to be $\frac{1}{2}CV^2$, the total energy change in the battery is therefore $\Delta U_{batt} = -CV^2$. Therefore the appropriate energy for the battery-capacitor system becomes,

$$U = -\frac{1}{2}CV^2, \tag{2.15}$$

reconciling the sign difference between the forces of Eqs. (2.14) and (2.13).

2.4.2 Dielectrophoresis of microscale particles

When examining the motion of particles much smaller than the electrodes, it is useful to consider the electrostatics of a particle in an external electric field $\mathbf{E}_0(\mathbf{x})$. A linear dielectric in an external field will become polarized with a dipole moment such that $\mathbf{p} \propto \mathbf{E}_0$. A dipole in an electric field will experience a force,[49, 46, 45]

$$\mathbf{F}_{DEP} = (\mathbf{p} \cdot \boldsymbol{\nabla})\, \mathbf{E}_0 \tag{2.16}$$

and a torque,

$$\boldsymbol{\tau} = \mathbf{p} \times \mathbf{E}_0. \tag{2.17}$$

For a static field, $\boldsymbol{\tau} = \mathbf{0}$ and the force is parameterized by ϵ_P and ϵ_M, the permittivities of the particle and medium respectively. A dielectric sphere of radius a will be polarized with a moment,

$$\mathbf{p} = 4\pi\epsilon_0 a^3 \left(\frac{\epsilon_P - \epsilon_M}{\epsilon_P + 2\epsilon_M} \right) \mathbf{E}_0 \tag{2.18}$$

and experience a force,

$$\mathbf{F}_{DEP} = 2\pi a^3 \epsilon_M \left[\frac{\epsilon_P - \epsilon_M}{\epsilon_P + 2\epsilon_M} \right] \boldsymbol{\nabla} E_0^2. \tag{2.19}$$

The movement of a particle along $\boldsymbol{\nabla} E_0^2$ is known as dielectrophoresis (DEP). The term in square brackets is the Classius-Mosotti factor K. It is sometimes convenient to describe DEP by the energy of a particle in an electric field,

$$U_{DEP} = -2\pi a^3 \epsilon_M \,\mathrm{Re}\left[\frac{\epsilon_P - \epsilon_M}{\epsilon_P + 2\epsilon_M} \right] E_0^2. \tag{2.20}$$

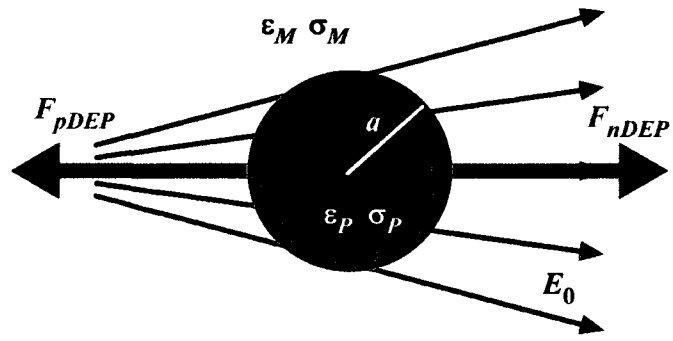

Figure 2.5: Schematic showing a spherical particle of radius a in an electric field $\boldsymbol{E}_0$. If the particle is more polarizable than the medium, it is attracted towards field maximum with positive dielectrophoresis (pDEP). If the particle is less polarizable than the medium, it is pushed into field minima with negative dielectrophoresis (nDEP).

Positive, negative, and traveling wave DEP

The situation becomes more interesting when the external electric field is oscillating at an angular frequency ω.[45] Now the field is given by $\mathbf{E}_0(\mathbf{x}, t) = \mathbf{E}_0(\mathbf{x}) \cos(\omega t + \chi(\mathbf{x}))$. The permittivities of the particle and medium are complex and given by $\tilde{\epsilon}_P = \epsilon_P - \frac{i\sigma_P}{\omega}$ and $\tilde{\epsilon}_M = \epsilon_M - \frac{i\sigma_M}{\omega}$ where σ_P and σ_M are the electrical conductivities of the particle and medium respectively. One of the consequences of applying a time-varying electric field is that the induced dipole moment is no longer necessarily in phase with the applied field. The phase lag between $\boldsymbol{p}$ and $\boldsymbol{E}_0$ is given by the relative magnitudes of the real and imaginary components of the complex Classius-Mosotti factor K,

$$K = \frac{\tilde{\epsilon}_P - \tilde{\epsilon}_M}{\tilde{\epsilon}_P + 2\tilde{\epsilon}_M}. \tag{2.21}$$

Two distinct types of DEP act due to the in-phase and out-of-phase components. Re$[K]$ (in-phase component) gives rise to conventional DEP, a force acting along ∇E_0^2 while Im$[K]$ (out-of-phase component) gives rise to traveling-wave DEP,[50] a force that acts along $\nabla\chi$. While both forces are useful in manipulating nano- and

microscale materials, conventional DEP is exclusively used in this work so we will focus our discussion on that effect.

The time-averaged conventional DEP force on a spherical particle is given by,

$$\langle \mathbf{F}_{DEP} \rangle = \pi a^3 \epsilon_M \,\mathrm{Re}\left[\frac{\tilde{\epsilon}_P - \tilde{\epsilon}_M}{\tilde{\epsilon}_P + 2\tilde{\epsilon}_M}\right] \nabla E_0^2. \tag{2.22}$$

The relative polarizabilities of the particle and medium affect the character of the DEP force. In particular, Re[K] can vary between 1 and -0.5. If Re[K] > 0, the particle is more polarizable than the medium and it is attracted to the maximum of E_0^2 by positive dielectrophoresis (pDEP). If Re[K] < 0, the particle is less polarizable than the medium and it is pushed to minima of E_0^2 by negative dielectrophoresis (nDEP).

Small dielectric particles often exhibit a crossover frequency f_C where at $f < f_C$, they experience pDEP and at $f > f_C$ they experience nDEP. While dielectric particles typically do not have appreciable body conductivity, the Stern layer of screening ions can move in response to an applied field resulting in a conductivity of the form $\sigma_P = \frac{2G_S}{a}$ where G_S is the surface conductance and a is the particle radius. In this circumstance, the crossover frequency is given by,[51]

$$f_C = \frac{1}{2\pi}\sqrt{\frac{\left(2G_S a^{-1}\right)^2 + 2G_S\sigma_M a^{-1} - 2\sigma_M^2}{2\epsilon_M^2 - \epsilon_M\epsilon_P - \epsilon_P^2}}. \tag{2.23}$$

Scaling of dielectrophoresis with electrode size

The scaling of the DEP force can be approximated by considering a voltage V applied across electrodes with spacing λ.[45] The typical electric field is $E \sim V/\lambda$ and typical gradients are $\nabla \sim \lambda^{-1}$ The DEP-force on a particle of radius a with $K \approx 1$ is

approximated by,

$$F_{DEP} \approx \pi \epsilon_M a^3 V^2 \lambda^{-3}. \tag{2.24}$$

For $\lambda = 1$ μm, $a = 100$ nm, $\epsilon_1 = 80\epsilon_0$, and $V = 10$ V, $F_{DEP} \approx 200$ pN. Further terms in the multipole expansion may offer contributions to dielectrophoresis when the particle size is large compared to variations in the electric field. The next order correction is due to an induced quadrupole moment, which is approximated by,[47]

$$F_{DEP}^{(2)} \approx \frac{1}{6}\pi \epsilon_M a^5 V^2 \lambda^{-5}. \tag{2.25}$$

For the parameters listed above, $F_{DEP}^{(2)} \approx 0.4$ pN and so it is appropriate to consider only the dipole term.

2.5 Other Considerations

2.5.1 Adhesive forces

Particles experience attractive forces holding them to surfaces resulting in what is known as the "sticky-finger" problem. There are two attractive forces that must be taken into consideration.[17, 18, 52, 19, 20] The van der Waals attractive forces between a particle of radius a and a substrate are described by the Derjaguin-Muller-Toporov (DMT) model of elastic contact. Here, the pull-off force is given by,

$$F_{DMT} = 4\pi \gamma_{SV} a, \tag{2.26}$$

where γ_{SV} is the solid-vapor interfacial energy, typically $\gamma_{SV} \approx 0.02$ Jm^{-2}. A typical pull off force for a glass particle with $a = 100$ nm is $F_{DMT} \approx 25$ nN. This force decreases with increasing surface roughness.[27] Capillary bridges also provide an

attractive interaction. In an ambient environment there is typically an adsorbed layer of water on all surfaces and its thickness depends on the relative humidity (RH). Objects in contact with the surface will be pulled together by the surface tension of the capillary bridge connecting them. This force is give by,

$$F_{capillary} = 4\pi a \gamma_L \cos(\theta_C), \tag{2.27}$$

where $\gamma_L \approx 0.072$ Jm^{-2} is the surface tension of the water and θ_C is the contact angle. Capillary forces between a hydrophillic particle with $a = 100$ nm and a substrate is typically $F_{capillary} \approx 100$ nN. This force is mitigated by working in RH$<$ 20%.

The adhesive forces present a problem to nanoassembly because the magnitude of adhesive forces are $\propto a$ while body forces, such as DEP, are $\propto a^3$. The consequence of this scaling is that as a decreases, body forces will not be able to overcome adhesive forces, which leads to the conclusion that non-contact trapping methodologies are necessary for nanoassembly.

2.5.2 Electric fields in fluid

Employing electrostatic forces in fluid is complex due to the multitude of electro-hydrodynamic phenomena that arise.[45] The fluid can either behave as a dielectric or as a conductor, depending on the frequency f of the applied electric field. The dielectric relaxation frequency is given by,

$$f_{RC} = \frac{1}{2\pi}\frac{\sigma_M}{\epsilon_M}, \tag{2.28}$$

analogous to an "RC" time from circuit theory. If $f < f_{RC}$, the applied field will be screened by ions and not penetrate into the fluid. To effectively apply DEP forces

f must be greater than f_{RC}. Another restriction is due AC electroosmosis (ACEO), or fluid flows due to the movement of the double layer in response to an AC electric field.[53] The characteristic frequency of ACEO is given by,

$$f_{ACEO} = \frac{\sigma_M \left(C_S \lambda_D + \epsilon_M\right)}{\lambda \pi^2 \epsilon_M C_S}, \tag{2.29}$$

where λ_D is the Debye length, $C_S \approx 0.007$ Fm^{-2} is the capacitance per unit area of the Stern layer of the double layer, and λ is the electrode separation. For a physiological buffer with $\sigma_M \approx 1$ Sm^{-1}, $\epsilon_M = 80\epsilon_0$, and $\lambda = 1$ μm, we find $\lambda_D \approx 1$ nm, $f_{RC} \approx 10$ GHz, and $f_{ACEO} \approx 15$ MHz. In contrast, for deionized (DI) water with $\sigma_M \approx 10^{-5}$ Sm^{-1}, we find $\lambda_D \approx 400$ nm, $f_{RC} \approx 100$ kHz, and $f_{ACEO} \approx 700$ Hz.[45]

Joule-heating can lead to fluid flows from electrothermal effects, but these effects are reduced in a low-conductivity solution. The change in temperature above ambient can be estimated as $\Delta T \sim \frac{\sigma_M V^2}{2\kappa_T}$ where κ_T is the thermal conductivity of the fluid and $\kappa_T = 0.58$ W/(mK) for water.[45] For an applied voltage of $V = 10$ V, $\Delta T \sim 150$ K in physiological buffer and $\Delta T \sim 2$ mK in DI water. The dominant electrothermal effect is buoyancy in which heating a liquid changes its density and resulting in gravitational which is proportional to V^2. In addition, local variations in temperature create variations in dielectric properties which lead to electrothermal effects proportional to V^4. These effects must be considered for high-conductivity media, but can be ignored in low-conductivity media.

2.5.3 Dielectric breakdown

The practical limitation to the maximum electric field that can be applied in a dielectric medium is given by the dielectric breakdown field E_{BD} in that medium.

The mechanisms that control this effect differs for solids, liquids, and gases

Breakdown in solids

Dielectric solids present the simplest system in which E_{BD} is scale invariant and depends on the field required to ionize the atoms of the solid For example, low-stress silicon nitride deposited by plasma enhanced chemical vapor deposition has $E_{BD} \approx 3 - 5$ MVcm^{-1} [54]

Breakdown in gases

Gases have E_{BD} that is determined by the pressure and electrode separation according to Paschen's law in which breakdown occurs when enough ions have sufficient mean-free-path to accelerate to an energy large enough to cause an ionization avalanche The Paschen law leads to $E_{BD} \approx 30$ kVcm^{-1} for air at 1 atm For gaps less than 5 μm, Paschen's law breaks down and field emission becomes the dominant cause of breakdown, giving $E_{BD} \approx 750$ kVcm^{-1} [55]

Breakdown in liquids

Dielectric breakdown in liquids is the most complicated variety of dielectric breakdown E_{BD} of a given liquid depends on the electrode composition, duration of applied field quantity of dissolved gas, among other factors While there is no clear consensus on the physics of dielectric breakdown in liquids, one model attributes the onset of streamers, or avalanches of charge carriers, to the formation of gas bubbles on the electrodes E_{BD} of water in response to a steady state electric field is com-

monly $E_{BD} \approx 1$ MVcm^{-1}, but the dynamic processes lead to strong dependance on pulse-duration, which raises E_{BD} at $f > 1$ MHz.[56]

Chapter 3

Fabrication of Coaxial and Triaxial AFM Probes

3.1 Introduction

In this Chapter, we present the fabrication procedure for creating coaxial and triaxial AFM probes. We begin by discussing the methodology of using an aluminum chip carrier and shadow masks to pattern films. Then, we step through a tip fabrication protocol from commercial probes to finished coaxial probes. Next, we discuss the variations in the fabrication protocol that are used to make different probes such as triaxial probes. Finally, we discuss film characterization and how the probes are integrated with a commercial AFM system.

3.2 Chip Holder Based Fabrication

Patterning films on the delicate 3D geometry of an AFM cantilever can be accomplished by mounting them on an aluminum chip carrier as shown in Figure 3 1(a) The holder has grooves that the probes fit snugly into as well as set screws that serve as alignment posts for shadow masks such as those shown in Figures 3 1(b)-(c) A scale schematic of how probes fit and align with a mask is shown in Figure 3 2 With these techniques, it is possible to deposit films with $\sim$ 100 μm alignment between masks and probes while not damaging the cantilevers Two principle varieties of masks are used aluminum masks for chemical vapor deposition and Kapton masks for physical vapor deposition (PVD)

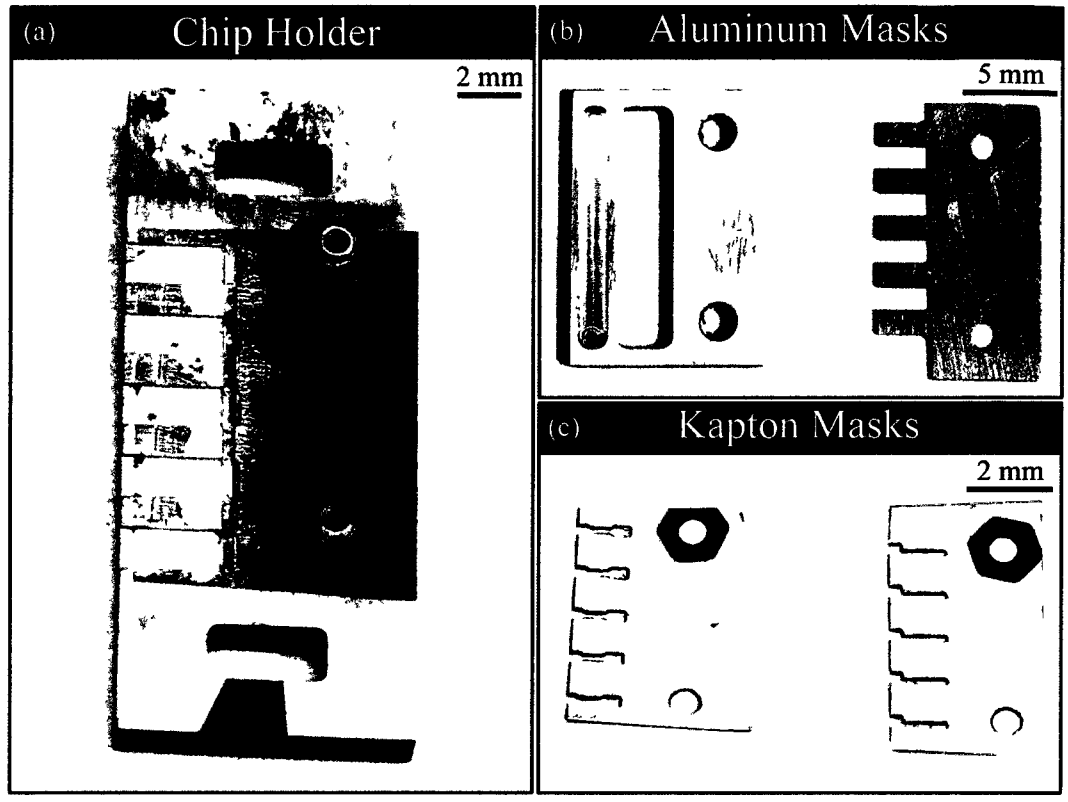

Figure 3.1: (a) Aluminum chip carrier which holds five AFM probes during processing. The AFM probes fit in the fives grooves on the left and the two alignment posts on the right allow shadow masks to be aligned to the probes. (b) Aluminum machined masks for masking CVD processes. (left) A mask that protects the cantilevers in the groove on the left while allowing material to be deposited through the hole to the body of the probes (right) A mask that is used to mask one side of the chips (c) Laser cut Kapton shadow masks for masking PVD processes. (left) A mask for coaxial probes that creates a single strip of metal on the cantilever and body (right) A mask for triaxial probes that creates an electrode and bond pad on one side of the chip.

3.2.1 Aluminum machined masks for CVD

Machined aluminum masks, such as those shown in Figure 3.1(b), are used to mask chemical vapor deposition (CVD). The omnidirectional deposition in CVD makes these masks of limited use as the film is still deposited at a decreased rate beneath

the mask. For complete masking of CVD, it is necessary to also coat the desired area in a thin layer of thermal grease or photoresist. Aluminum masks are designed in AutoCAD (Autodesk Inc.) and manufactured by the SEAS machine shop.

3.2.2 Kapton laser cut masks for PVD

Masking evaporation is simple as it is a directional process. Pieces of Kapton are cut with a laser cutter (VersaLaser VLS3.50 - Universal Laser Systems, Inc.) into shadow masks such as those shown in Figure 3.1(c). 0.005" thick Kapton film is purchased from McMaster-Carr Inc. and masks are designed in AutoCAD (Autodesk Inc.) and redrawn in CorelDraw (Corel Corp.) for use with the laser cutter.

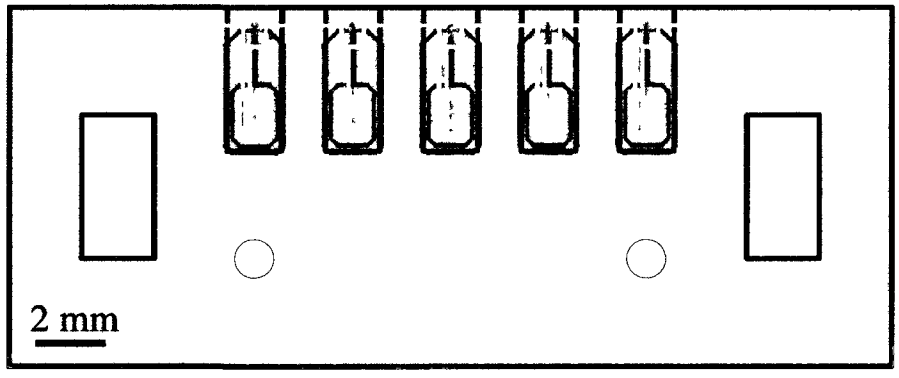

Figure 3.2: Scale schematic of the chip holder (grey) with five probes (blue) and a shadow mask (red).

3.3 Fabrication Protocol

This section describes a typical coaxial probe fabrication. The procedure described here produces probes with $\lambda \approx 50$ nm insulating layer of low stress silicon nitride on metalized probes. Variations of this protocol are discussed in Section 3.4.

3.3.1 Probe cleaning and mounting

Fabrication began by cleaning and mounting commercial, conducting AFM probes (Arrow-NCPt – Nanoword AG) on a chip carrier. The probes are monolithic silicon heavily n-doped to a resistivity of 0.01 to 0.025 Ωcm. The front and back of the probes come coated in a 25 nm thick layer of PtIr5 (an alloy of platinum and iridium) to provide a low resistance path to the tip. The cantilevers have specified length L = 160 μm, width W = 45 μm, thickness H = 4.6 μm, spring constant $k \approx 42$ N/m, and resonance frequency $f_0 \approx 285$ kHz.

The probes must be very clean before processing can begin. Small particulate matter can disrupt the insulating layer and compromise the electrical integrity of the probes. For this reason, a package of probes for fabrication is never opened outside the cleanroom. The probes must be chemically cleaned before they are mounted on the chip carrier. The small size and fragility of the probes makes any processing difficult, so we designate one pair of tweezers for nothing but manipulating AFM probes. It is cumbersome to move them in and out of disposable beakers, so using shallow petri dishes for soaking steps is preferable. First, the glassware and the chip holder is sonicated for 5 min. in acetone, rinsed in deionized (DI) water, rinsed in isopropyl alcohol (IPA), and then blown dry with N_2.

The probe chemical cleaning procedures contains the following steps:

1. Probes are soaked in acetone bath in a pretri dish on a hot plate at 80 °C for 10 min. The acetone will boil off and needs to be refilled every few minutes.

2. Each probe is held in an acetone filled disposable beaker in the sonicator for 10 s. The probes cannot be sonicated loosely or they will move around and

destroy the cantilever.

3. Probes are soaked in a DI water bath in a petri dish for 10 min.

4. Probes are soaked in an IPA bath in a petri dish for 10 min.

5. While the probes are soaking in the IPA, a thin coating of AOS silicone XT thermal grease is painted on the grooves of the chip holder.

6. Each probe is blown dry with nitrogen and placed in a groove. Care must be taken to ensure the probe is aligned parallel with the groove and flush with the back of the holder. It is also crucial that no thermal grease ends up on the top surface of the probes.

7. The mounted probes are inspected in a microscope and stored in the dry box.

3.3.2 Film deposition

Film deposition proceeds as depicted schematically in Figure 3.3. First, a 30 nm sticking layer of titanium is deposited on the probes with electron beam evaporation (EE) using EE-4. The probe holder is held on the stage with a small piece of carbon tape which has been tapped a few times to make it less sticky. The stage is set to rotate at 25% and once the chamber pressure reaches $\sim 5 \times 10^{-7}$ Torr, 30 nm of titanium is deposited.

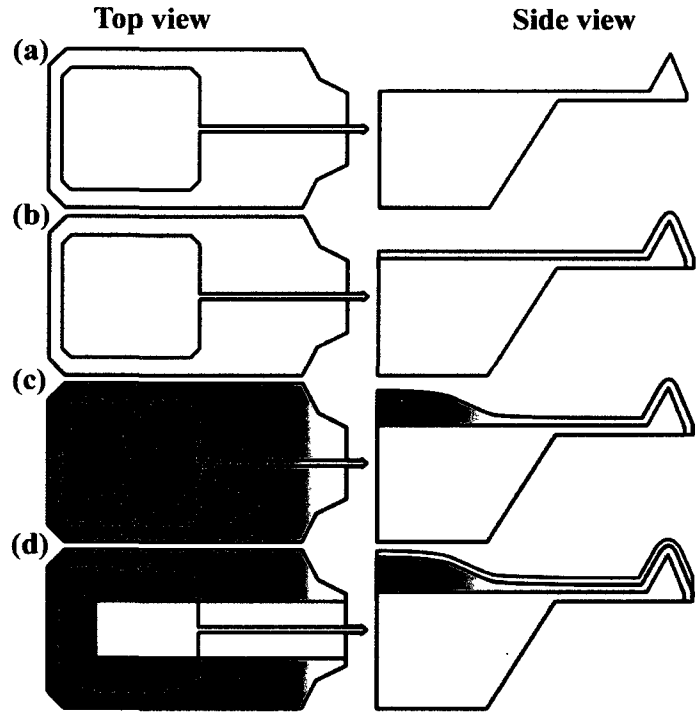

Figure 3.3: Schematic of films deposited on a coaxial probe depicted from the top (left column) and side (right column). (a) A cleaned, conducting probe is coated in an adhesive metal, such as Ti. (b) The probe is coated with a thin insulating layer, typically $\sim$ 50 nm of low-stress SiN_x. (c) The cantilever is masked with an aluminum mask and a thick insulating film is deposited on the back of the chip for mechanical and electrical stability. (d) Finally, the conducting shell is deposited through a shadow mask.

To deposit an insulating layer on the probes, a $\sim$ 50 nm layer of low stress silicon nitride is deposited by plasma enhanced chemical vapor deposition (Cirrus 150 – Nexx Systems), as depicted in Figure 3.3(b). After running the burn-in and pre-clean for 10 min. each, the chip holder is mounted on the chuck with thermal grease. The process to deposit silicon nitride is named "SiNLST" and it consists of 5.8 sccm of N_2, 40 sccm of 3% SiH_4 in Ar, and 20 sccm Ar, is run for 500 s at 10 mTorr with 265 W of microwave power. The backside helium is pressurized to 10 Torr of He, attention should be payed to ensure that there isn't a He leak which would manifest

as a backside helium rate above 1 sccm or the chamber pressure being above 10 mTorr despite the turbo valve being fully open. If the helium is leaking, the chuck must be recentered. When the probes emerge from this step, they should appear a bright blue color.

Next, an additional insulating layer is deposited on the body of the probes to mechanically and electrically protect them, as shown in Figure 3.3(c). In this step, the aluminum mask shown on the left in Figure 3.1(b) is placed over the chip holder, covering the cantilevers and leaving a hole through which the body of the chips are visible. Now $\sim$ 1.4 μm of silicon dioxide and $\sim$ 500 nm of low stress silicon nitride are deposited by running the process titled "KB-KPFM" which consists of 60 min. of a recipe titled "SiO2HR", a two minute cooling step with 10 mTorr of Ar, then 60 min. of SiNLST. The SiO2HR recipe is 20 sccm of O_2, 100 sccm of 3%SiH_4 in Ar, and 10 sccm Ar at 20 mTorr 300 W of microwave power. A bilayer SiO_2 and SiN_x is used to minimize the possibility of pinhole defects. While the oxide process is faster, the nitride process creates a film that is less permeable to water and ions. The entire PECVD process takes 3 hours when at the fastest so booking 3.5 hours is usually prudent.

To deposit the shell electrode, EE is used to deposit 30 nm of titanium as a sticking layer followed by 50 nm of gold to lower the resistivity, as shown in Figure 3.3(d). This step also uses EE-4 but includes the Kapton mask shown on the left of in Figure 3.1(c) to minimize the area of the electrode. It is important to minimize the area of the electrode to lower the capacitance, reduce the chance of pinhole defects, and keep the shell conductor away from the edges of the chip where defects in the insulating layer

are most likely. A probe with films patterned is shown in Figure 3.4

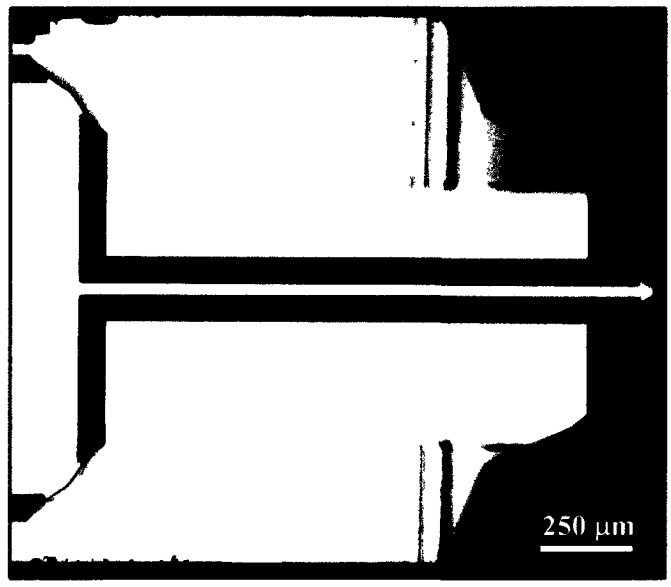

Figure 3.4: Optical micrograph of a AFM cantilever and chip with films necessary to become a coaxial probe. The gold strip running across the probe body is connected to the shell electrode and the bands of color are from the changing thickness of the insulating layer.

3.3.3 Liftoff and testing

Finished probes are removed from the chip carrier, briefly chemically cleaned to remove the thermal grease, and electrically tested. Before removing them from the chip carrier, a petri dish and disposable beaker are cleaned and filled with acetone. The beaker is put in the sonicator. Probes are individually pulled off the chip carrier and held in the acetone in the sonicator for 10 s to remove the majority of the thermal grease. A 5 min. soak in the acetone will remove the rest. The probes are soaked in IPA for 5 min. then blown dry with N_2 and placed in labeled a gel box.

Before focused ion beam (FIB) processing, probes are electrically tested to ensure

that the insulating layer is robust. To test the probes, they are placed on a strip of aluminum tape which is connected to a Fluke multimeter. The other probe of the multimeter is pressed against the contact pad of the shell electrode with the multimeter is in ohmmeter mode. Robust probes will register as overloads or the resistance will begin as several MΩ gradually rise, indicating a capacitive load.

3.3.4 Exposing the coaxial electrodes

Coated probes are milled in the focused ion beam (FIB) to expose the coaxial electrodes. Two custom machined SEM stubs are used for this, one of which is shown in Figure 3.5. One stub is milled so that the surface is raised 36° to make the cantilever parallel with the path of the ion beam in the FIB. The other stub, shown in Figure 3.5 with two probes mounted on it, is at 47°, to account for the 11° angle between the cantilever and substrate in the Asylum AFM systems. Probes are mounted on these by pressing the into a thin layer of silver paint on the shelf of the stubs, as shown in Figure 3.5.

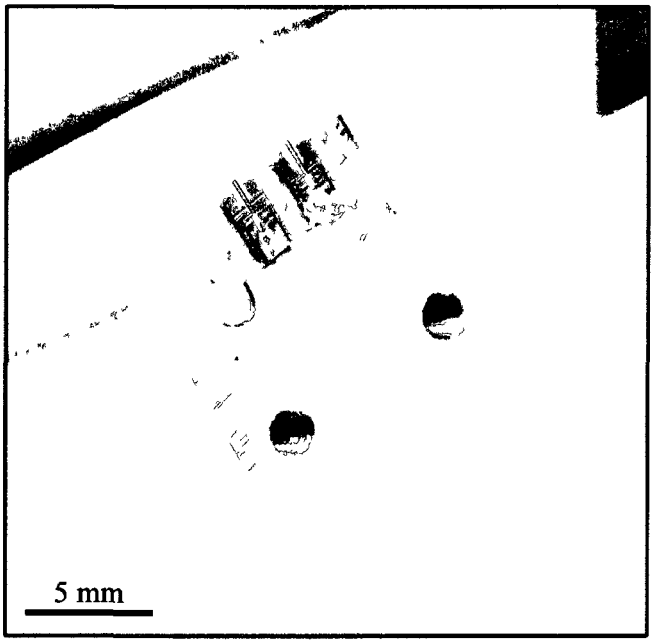

Figure 3.5: An angled probe holder for processing. This stub holds probes at 47° to account for the 36° angle of the ion beam and 11° angle in the AFM system. Two coaxial probes are visible silver painted to the stub.

The coaxial electrodes are exposed by milling in the FIB. First, the probe is found with the scanning electron microscope (SEM) and the stub is rotated so that the cantilever is pointing directly at the FIB aperture (vertical in the display). By moving the tip to a working distance of 5 mm and centering it below the SEM, it will be directly in view with the FIB. The beam current of the FIB is set to 1 pA and the cantilever is brought into focus. Prolonged viewing of the probe with the ion beam damages the films, so focusing and sigmation correction are done as quickly as possible and while looking at the sides of the cantilever, not the tip. When the beam is in focus and the texture of the films is visible, the beam is brought to the tip, refocused and frozen. The milling region is defined as a fine rectangle to include the entire tip up to where the tip is 300 nm wide. The milling is set to 10 layers at

60 s/layer with a beam current of 1 pA. Before milling, a final FIB image is taken to correct for any drift that has occurred. After each layer of milling, a FIB frame is taken to monitor the progress. A series of 1-3 passes is typically sufficient and the probe appears finished when imaged with the ion beam. Finally, the probe is imaged with the SEM to ensure that the core electrode is visible and measure the probe size.

The finished probes are removed from the stub and are ready for use in the AFM. The FIB sample holder is taken to the wet bench and acetone is sprayed at the probes until the silver paint is seen to have dissolved. The probes are then gently grabbed with tweezers to see if they come off with little force. If not, more acetone is applied. Once they are removed, they are sonicated for 10 s by being held into acetone, blown dry with N_2, and stored in a gel box. A finished probe created with this protocol is shown in Figure 3.6(b).

3.4 Variations of the Fabrication Procedure

The protocol described in Section 3.3 is flexible and variants of this protocol have been used to make each of the probes shown in Figure 3.6. Probes are characterized by their insulating layer thickness λ. The four probe models shown are (a) coaxial probes with $\lambda \approx 400$ nm used for imaging and manipulation with dielectrophoresis, (b) coaxial probes with $\lambda \approx 50$ nm used for high resolution electrostatic imaging, (c) triaxial probes with $\lambda \approx 1.6$ μm used for manipulating nanoscale objects with negative dielectrophoresis, and (d) coaxial probes with ~300 nm insulating layers that have been milled such that the pyramidal core conductor protrudes for high resolution topographic imaging as well as electrostatic imaging.

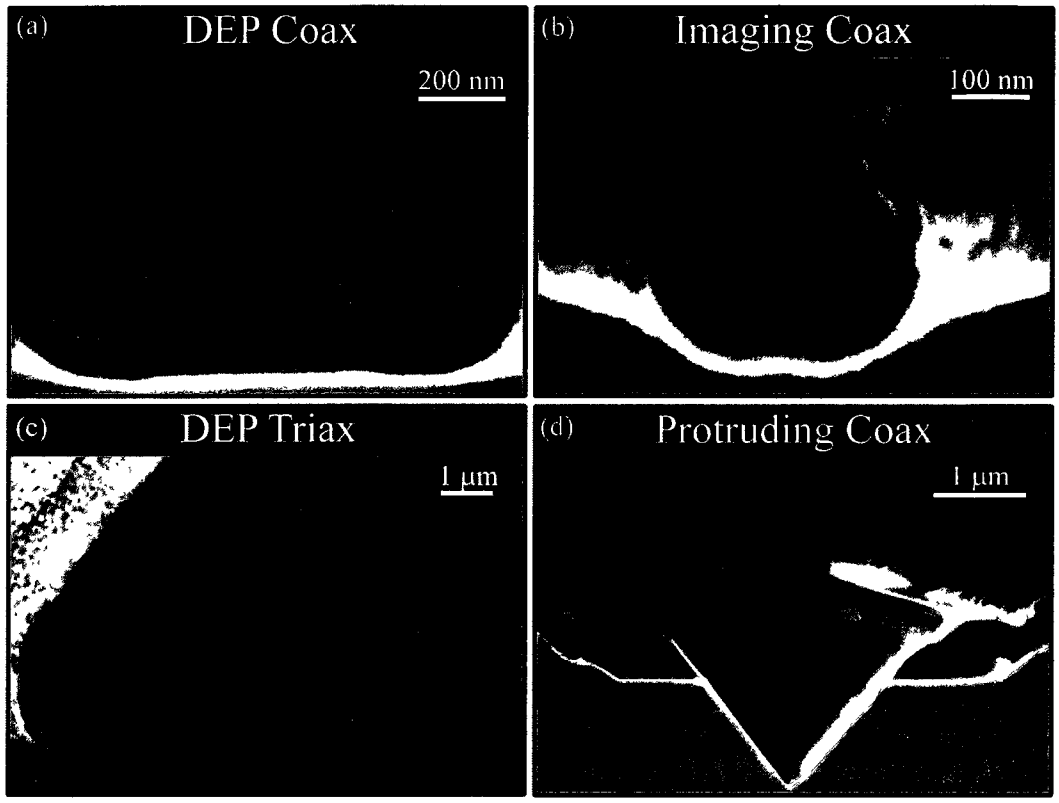

Figure 3.6: SEM micrographs of finished coaxial and triaxial probes. (a) A coaxial probe used for dielectrophoresis. (b) A coaxial probe used for high-resolution imaging. (c) A triaxial probe used for manipulation with dielectrophoresis. (d) A coaxial probe that has been milled such that the pyramidal core electrode is protruding.

3.4.1 Ohmic contact to silicon probes

Uncoated silicon probes (Arrow-NC – NanoAndMore) can be used instead of metalized probes and they have the advantage that a sticking metal layer is not needed for the insulating layer. Such probes were used to make DEP coaxes, as shown in Figure 3.6(a). A disadvantage is that it is more difficult to make Ohmic contact to the core electrode. This is not necessary when bare silicon is on top of the probe and directly clipped to, as the clip provides sufficient pressure to penetrate the na-

tive oxide layer. Ohmic contact is achieved by thermal evaporation of of 15 nm of Ti and 100 nm of Al on the back side followed by a 30 min anneal in forming gas at 325 °C. Probe holders that have a hole in the back are used to allow deposition without having to remount them or mount them upside down.

3.4.2 Thermal evaporation

Prior to the use of EE-4, thermal evaporation was used to deposit all metal layers. In order to evenly coat the probes, a rotating stage was needed. Rotation speeds were typically a quarter turn every 2 nm of thickness. Chrome was used instead of titanium as a sticking layer due to ease of evaporation.

3.4.3 Triaxial probe fabrication

The fabrication protocol to create traxial probes like the one shown in Figure 3.6(c) is similar to the method described in Section 3.3 and it proceeds as follows.

1. Five Arrow-NCPt probes are cleaned and mounted as described.
2. 60 nm of Cr deposited with thermal evaporation while rotating the samples.
3. A trilayer of 100 nm SiN_x, 1800 nm SiO_2, 100 nm SiN_x is deposited by PECVD.
4. 25 nm of Cr, 50 nm of Au, and 25 nm more of Cr are deposited through the mask shown on the right in Figure 3.1(c) creating a bond pad for the inner shell.
5. A trilayer of 100 nm SiN_x. 1800 nm SiO_2, 100 nm SiN_x is deposited by PECVD with small drops of thermal grease applied to the bond pads of the inner shell and the aluminum mask shown on the right in Figure 3.1(b).

6. 25 nm of Cr and 75 nm of Au are deposited through the mask shown on the right in Figure 3.1(b) with the mask flipped upside down to put the bond pand for the outer shell on the opposite side from the inner shell.

7. The probes are lifted of off the chip holder and mounted on the 36° FIB stub as described above.

8. Triaxial probes are milled using the FIB with a beam current of 300 pA and cut to where the tip is ~10 μm wide.

The layout of the bond pads can be seen in Figure 3.7 with two wire bonds connected to the top pad which leads to the inner shell and two wire bonds connected to the bottom pad which leads to the outer shell. The probe is silver painted down to make electrical contact to the core conductor.

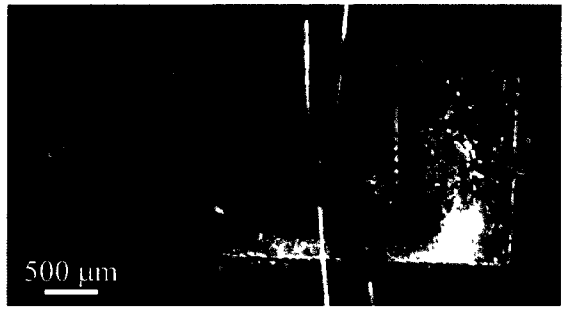

Figure 3.7: Optical micrograph of a triaxial AFM probe mounted on a printed circuit board with silver paint. Wire bonds make contact to the top and bottom bond pads which connect to the inner and outer shell electrodes respectively. The patterned metal films are visible running from the bond pads to the cantilever on the left side of the probe.

3.4.4 Protruding tips

Coaxial probes have tightly confined electric fields, but their blunt profile detracts from their topographic resolution. In order to mitigate degradation in spatial resolution, we created probes in which the insulating layer was milled off in three sections, to expose the pyramidal core electrode as shown in Figure 3.6(d). Such probes are made with Arrow-NCPt probes with 230 nm of SiO_2 and 80 nm of SiN_x. The probes are milled with four cuts, one parallel to each of the two front faces and two parallel to the back face, one from each side. Beam current is typically 40 pA with XeF_2 gas injected to increase milling speeds.[37] These probes were fabricated by Kevin Satzinger.

3.5 Film Characterization

The insulating layer in a coaxial probe is a crucial part of their function so it is important to characterize the thickness and dielectric strength. Test samples are deposited on 9×9 mm^2 silicon chips. The thickness is determined by spectroscopic ellipsometry (WVASE32 – J.A. Woollam) with wavelengths between 300 nm and 800 nm at angles of incidence between 55° and 75°. The deposition rates are found to be 3.89 Å/s for SiO2HR and 1.35 Å/s for SiNLST. The index of refraction at 630 nm for each of the films are found to be 1.45 for SiOHR and 1.82 SiNLST.

The film thickness at the tip is not uniform due to incomplete sidewall coverage and anisotropy of deposition. Sidewall coverage for plasma enhanced CVD is not perfect and can be measured after FIB milling by observation of the SEM, as seen

in Figure 3.6(a). The insulator film width at the tip varies due to the asymmetry of tip and its uneven exposure to the plasma. The film thickness on the probe is measured to be $\gtrsim 50\%$ of the reference thickness with a maximum thickness of $\sim 90\%$ the reference thickness.

The films are further characterized by measuring the breakdown voltage. 595 nm thick SiN_x films are deposited on a silicon wafer and 250 $\times$ 250 μm^2 Cr/Au islands are patterned with photolithography. The breakdown voltage V_{BD} of many squares is found by contacting an individual island with a probe station and ramping a DC voltage up until breakdown is observed. The distribution of breakdown voltages V_{BD} is shown in Figure 3.8. The mean value of the breakdown field is $E_{BD} \approx 4.8$ MV/cm and E_{BD} varies from 2 to 7 MV/cm, in good agreement with typical values seen for dielectrics as discussed in Section 2.5.3.[54]

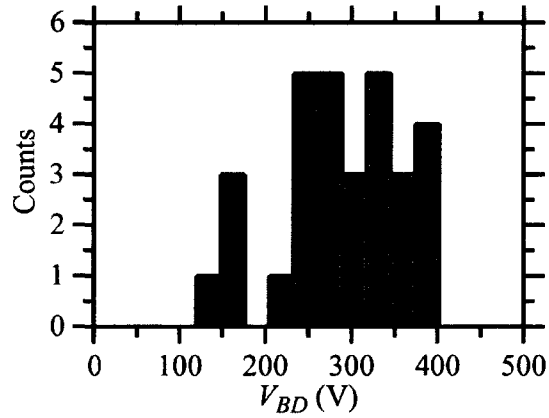

Figure 3.8: The distribution of breakdown voltages V_{BD} of 595 nm thick film of low stress silicon nitride. The mean breakdown voltage is $E_{BD} \approx 4.8$ MV/cm.

3.6 Integration into a Commercial AFM System

Coaxial probes are integrated into a commercial AFM system (MFP3D – Asylum Research) by a custom tip holder picture in Figure 3.9. Probes are held between a metal clip and a printed circuit board. The cantilevers are suspended above a window to allow observation with a microscope and the so that a laser spot can be focused onto the cantilever. The metal clip makes electrical contact to the shell electrode and two gold leads on the printed circuit board allow contact to the core electrode. Once the probe is mounted, the bottom contact is verified with a multimeter by checking to make sure that the resistance between the two bottom leads is low, typically 15 Ω, while the resistance between the clip and bottom leads is large, typically overloading the multimeter. The two leads are insulated form the electronics in the AFM and are brought out by wires. The probe can be connected to any combination of outputs of the AFM controller or custom electronics depending on the system.

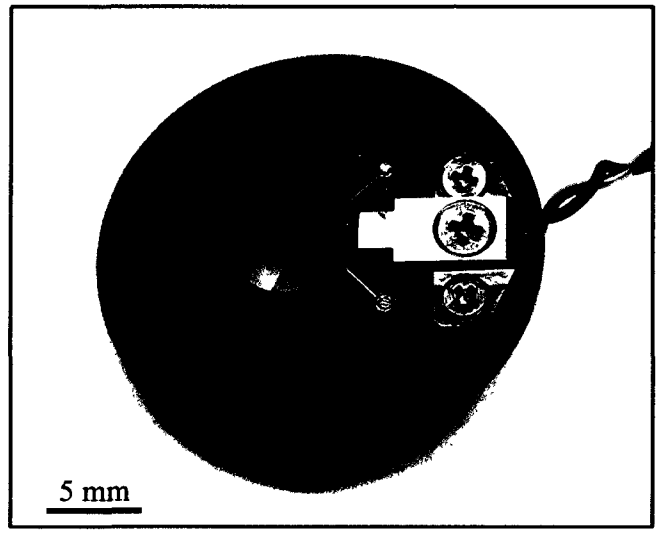

Figure 3.9: Optical image of the coaxial tip holder supplied by Asylum Research. A coaxial probe would rest between the metallic clip on the right and the green printed circuit board such that the cantilever is suspended over the glass window in the middle of the tip holder. Electrical contact to the shell electrode is made through the clip while the two gold leads of the printed circuit board make contact to the core electrode. The two wires leading out of the frame connect these electrodes to external circuitry.

Chapter 4

Self-Driving Capacitive Cantilevers

4.1 Introduction

A major trend in advancing AFM techniques is to increase the measurement bandwidth to afford faster scanning.[57] This is commonly done by using stiffer, higher frequency cantilevers. This presents a challenge for commercial atomic force microscopes that utilize a piezoelectric stack on which the probe is rested to drive the cantilever. Driving the cantilever with a distant source results in exciting extraneous mechanical modes in the chip and environment. The situation is worse in liquid as large scale motion leads to fluid flows which disturb the measurement. Local driving has been demonstrated by depositing piezoelectric materials on the cantilever[58] and exciting vibrations with a Schottky barrier.[59]

Here, we demonstrate a cantilever with an embedded capacitor that couples the mechanical deformation of the cantilever to the electrostatic energy stored in the capacitor. We use this coupling to mechanically drive cantilevers by the application

of an AC voltage. Such driving is useful for dynamic AFM applications such as tapping mode AFM, contact resonance measurements, and driving cantilevers at high frequencies. We begin by describing a model of a capacitive cantilever that explains the coupling of the electrostatic energy to the bending of the cantilever. We use this model to derive the expected drive amplitude and force in self-driving capacitive cantilevers. Next, we find that electrostatic driving enables higher fidelity driving of the mechanical resonance mode than by mechanical driving and electrostatic driving is found to be in quantitative agreement with our model. We demonstrate amplitude modulation imaging and contact resonance with electrostatic driving. Finally, we discuss future applications of this technique including high frequency driving, driving in liquid, and self-sensing probes.

4.2 Capacitive Cantilever Dynamics

A capacitive cantilever can be understood by expanding the Euler-Bernoulli energy of bending to include the electrostatic energy stored in the capacitor. The electrostatic energy is coupled with the mechanical deformation by two effects that change the capacitance with mechanical deformation. The first effect is Maxwell stress and manifests as the dimensions of the capacitor varying with strain. The second effect is electrostriction, or the change in dielectric constant in response to strain. These two effects compete but Maxwell stress is more significant for the devices presented here. In this Section, we describe the theory behind these effects to motivate their use to drive a cantilever.

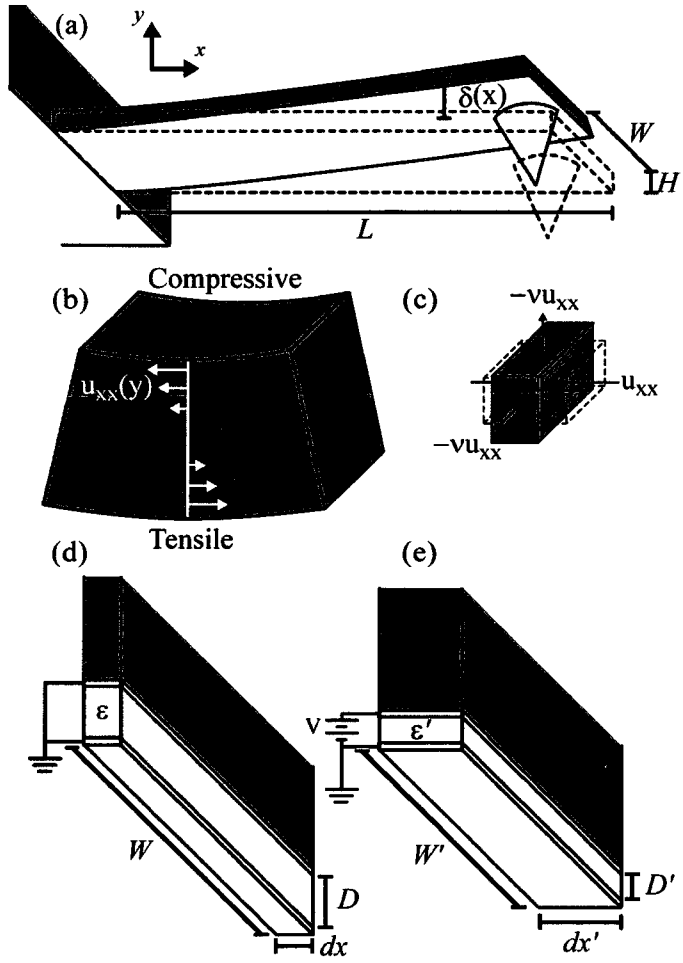

Figure 4.1: (a) Schematic of the deflection of a capacitive cantilever. (b) Linear strain profile in an Euler-Bernoulli beam due to bending. (c) Poisson's effect generates transverse strain in response to longitudinal strain. (d) A cross section of the bottom face of the cantilever, which houses a thin film capacitor. (e) When a voltage is applied to the capacitor, the dimensions and relative dielectric permittivity are modified.

4.2.1 Euler-Bernoulli deformation of a cantilever

The mechanical deformation of cantilever can be described by analyzing the cantilever as an Euler-Bernoulli beam.[60] We consider a uniform and isotropic thin cantilever of length L, with rectangular cross section of width W and thickness H.

The cantilever is bound at $x = 0$ and free at $x = L$, as shown in Figure 4.1(a). Thin ($H \ll L$) cantilevers may be described by Euler-Bernoulli beam theory in which the dynamics of the bead are described by Eq. (2.1). If surface films such as the films that make up the capacitor are thin, the presence of the films do not significantly affect the mechanical properties of the cantilever.[35]

The center position is deflected to a location $y = \delta(x)$ where δ is the deflection profile of the cantilever. Mechanical deformations may be characterized by the Cauchy strain tensor $\overline{u}$ given by,[60]

$$u_{ij} = \frac{1}{2}\left(\frac{\partial \zeta_i}{\partial x_j} + \frac{\partial \zeta_j}{\partial x_i}\right) \tag{4.1}$$

where $\boldsymbol{\zeta}$ is the infinitesimal displacement in the $\boldsymbol{x}$ direction. The strain is usually very small ($u_{ij} \ll 1$). Euler-Bernoulli theory predicts that bending generates a longitudinal strain that is linear in distance away from the center position, given by,

$$u_{xx}(x, y) = -y\frac{d^2\delta}{dx^2} \tag{4.2}$$

as shown in Fig 4.1(b). Further, the energy of bending an Euler-Bernoulli beam is given by,

$$U_{Bending} = \int_0^L \frac{1}{2} Y I \left(\frac{\partial^2 \delta}{\partial x^2}\right)^2 dx, \tag{4.3}$$

where I is the area moment of inertia and Y is the Young's modulus. Strain transverse to the cantilever axis is generated by Poisson's effect as shown in Figure 4.1(c). The transverse strain is given by $u_{yy} = -\nu u_{xx}$ and $u_{zz} = -\nu u_{xx}$ where ν is the Poisson's ratio of the cantilever material.

4.2.2 Maxwell stress

The principle effect that mechanical deformation has on the electrostatic energy stored in the capacitor is to physically deform the geometry of the capacitor, an effect known as Maxwell stress.[61] A cross section of the capacitor is shown in Figure 4.1(d). Here the insulating film has relative permittivity ϵ and thickness D. The capacitor has capacitance given by,

$$C = \frac{LW\epsilon\epsilon_0}{D} \tag{4.4}$$

If a voltage V is applied to the electrodes, the electrostatic energy stored in the capacitor is given by,

$$U_C = -\frac{1}{2}CV^2. \tag{4.5}$$

Here, the negative sign has been included to account for the fixed V system by including the energy liberated from the battery as discussed in Section 2.4.1. The dimensions of the capacitor are distorted by the strain of bending as shown in Figure 4.1(e). The change in dimensions is determined by the local longitudinal strain u_{xx} and is describe by,

$$dx \rightarrow dx' = dx(1 + u_{xx}) \tag{4.6a}$$

$$D \rightarrow D' = D(1 - \nu u_{xx}) \tag{4.6b}$$

$$W \rightarrow W' = W(1 - \nu u_{xx}) \tag{4.6c}$$

It is evident from Eq. (4.4) that the effect on the capacitance from the change in D and the change in W will cancel but that the change in dx will affect the capacitance.

4.2.3 Electrostriction

Mechanical strain changes the dielectric permittivity through electrostriction in opposition to the effect of Maxwell stress. For an isotropic material under small deformation, the most general dielectric tensor $\overline{\epsilon}$ may be written as,[62, 61, 63]

$$\overline{\epsilon} = \epsilon\overline{I} + a_1\overline{u} + a_2\,\mathrm{tr}(\overline{u})\overline{I}, \tag{4.7}$$

where $\overline{I}$ is the identity matrix and tr() indicates the trace operation. Here, ϵ is the relative permittivity and a_1 and a_2 are constants that determine the response to shear and bulk deformations respectively. For isotropic materials, a_1 and a_2 depend only on the relative permittivity ϵ and are given by,[62]

$$a_1 = -\frac{2}{5}(\epsilon - 1)^2 \tag{4.8a}$$

$$a_2 = -\frac{1}{3}(\epsilon - 1)(\epsilon + 2) + \frac{2}{15}(\epsilon - 1)^2 \tag{4.8b}$$

The magnitudes of a_1 and a_2 are plotted *vs.* relative permittivity in Figure 4.2(a). For silicon-rich silicon nitride with a relative permittivity $\epsilon = 7.8$[64] we find $a_1 = -18.5$ and $a_2 = -16$, indicated on the plot by a grey line.

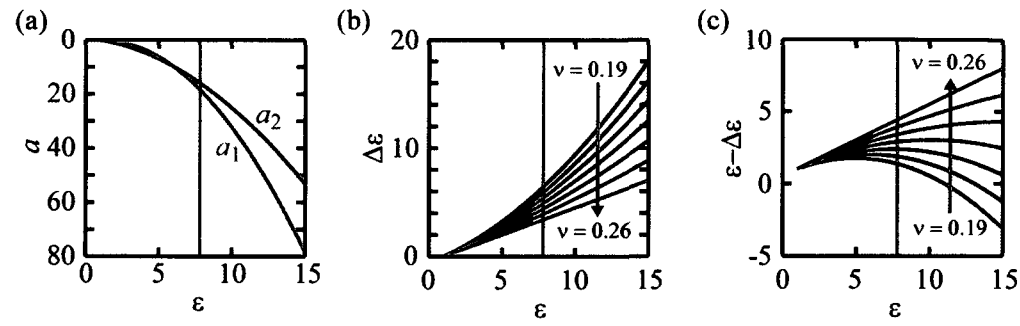

Figure 4.2: (a) Calculation of shear deformation (a_1) and bulk deformation (a_2) electrostriction constants for isotropic solids. The grey line indicates the relative permittivity of silicon-rich silicon nitride. (b) The proportionality constant $\Delta\epsilon$ representing the linear response of the relative permittivity in response to strain. The grey line indicates the relative permittivity of silicon nitride and the variation with respect to Poisson's ratio ν is apparent as indicated on the plot. (c) The overall electrostatic contribution to the energy is proportional to $\epsilon - \Delta\epsilon$ when electrostriction and Maxwell stress are both included. This plot illustrates the effect of varying ϵ and ν. Materials with higher ν experience a greater capacitive contribution while the response with respect to ϵ is non-monotonic, especially for small values of ν.

Strain results in a linear reduction of permittivity. The electric field is predominantly y-directed so the change in energy will be determined by ϵ_{yy} which can be written,

$$\epsilon_{yy} = \epsilon - a_1 \nu u_{xx} + a_2 u_{xx}(1 - 2\nu). \tag{4.9}$$

We can write the change in relative permittivity in response to applied strain as,

$$\epsilon \rightarrow \epsilon' = \epsilon - \Delta\epsilon u_{xx} \tag{4.10}$$

by defining,

$$\Delta\epsilon = a_1 \nu - a_2(1 - 2\nu). \tag{4.11}$$

For silicon-rich silicon nitride with a relative permittivity $\epsilon = 7.8$[64] and taking a Poisson's ratio of $\nu = 0.21$ as typically used for silicon nitride grown with plasma enhanced chemical vapor deposition,[65, 66] we find $\Delta\epsilon = 5.4$. The value of $\Delta\epsilon$

strongly depends on ν, as illustrated in Figure 4.2(b) and is a potential source of uncertainty in this model.

4.2.4 Bending energy of a capacitive cantilever

The result of Maxwell stress and electrostriction is that the electrostatic energy stored in a capacitor depends the bending of the cantilever. The electrostatic energy of the capacitor shown in Figure 4.1(a) can be found by integrating the energy along x while applying the geometric transformation from Eq. (4.6) and change in relative permittivity from Eq. (4.10). The electrostatic energy stored in the capacitor is given by,

$$U_C = -\int_0^L \frac{1}{2}\left(1 - \frac{\Delta\epsilon}{\epsilon}u_{xx}\right)(1+u_{xx})\frac{\epsilon\epsilon_0 WV^2}{D}dx. \tag{4.12}$$

The longitudinal strain in the capacitor is found by applying Eq. (4.2) with $y = -\frac{H}{2}$,

$$u_{xx} = \frac{H}{2}\frac{d^2\delta}{dx^2}. \tag{4.13}$$

The electrostatic energy can be expanded,

$$U_C = -\int_0^L \frac{1}{2}\left(1 + \left[1 - \frac{\Delta\epsilon}{\epsilon}\right]\frac{H}{2}\frac{d^2\delta}{dx^2} - \frac{H^2}{4}\left(\frac{d^2\delta}{dx^2}\right)^2\frac{\Delta\epsilon}{\epsilon}\right)\frac{\epsilon\epsilon_0 WV^2}{D}dx. \tag{4.14}$$

The constant term plays no role in the cantilever dynamics, so we may neglect it. The total energy of bending the cantilever may be found by combining Eq. (4.14) and Eq. (4.3) to find,

$$U = \int_0^L \left(\left[\frac{YWH^3}{24} + \frac{WH^2\Delta\epsilon V^2}{8D}\right]\left(\frac{d^2\delta}{dx^2}\right)^2 - \frac{[\epsilon - \Delta\epsilon]\,\epsilon_0 WHV^2}{4D}\left(\frac{d^2\delta}{dx^2}\right)\right)dx \tag{4.15}$$

The two effects of an applied voltage are to introduce a term linear in bending and raise the bending modulus. The relative change in bending modulus with an applied

voltage is small if $V \lesssim \sqrt{\frac{DYH}{3\Delta\epsilon\epsilon_0}}$; for $H = 4.6$ μm, $D = 60$ nm, $\Delta\epsilon = 5.4$, and $Y \sim 200$ GPa we find $V \lesssim 4$ kV, so we may safely ignore the second order electrostatic contribution. The total energy may be written,

$$U_{total} = \int_0^L \left(\frac{YWH^3}{24} \left(\frac{d^2\delta}{dx^2} \right)^2 - \frac{[\epsilon - \Delta\epsilon]\,\epsilon_0 WHV^2}{4D} \left(\frac{d^2\delta}{dx^2} \right) \right) dx \tag{4.16}$$

It is clear from this expression that $\delta = 0$ is no longer the deflection profile that minimizes the energy. In particular, we may minimize the integrand with respect to bending to find the new bending which minimizes the energy,

$$\frac{d^2\delta}{dx^2} = \frac{3[\epsilon - \Delta\epsilon]\epsilon_0 V^2}{DYH^2}. \tag{4.17}$$

We may now integrate this equation with the boundary conditions that $\delta(0) = 0$ and $\frac{d\delta}{dx}(0) = 0$ to find the rest deflection with an applied voltage,

$$\delta = \frac{3[\epsilon - \Delta\epsilon]\epsilon_0 V^2}{2DYT^2} x^2. \tag{4.18}$$

We can parameterize the deflection $\delta(L)$ at the end of the cantilever with the force F required to create an equivalent deflection of the tip. Considering the motion of the tip as spring-mass system, the equivalent force F is found using $F = k\delta(L)$ where k is the effective spring constant of the tip given by $k = \frac{YWH^3}{4L^3}$. The force is found to be,

$$F = [\epsilon - \Delta\epsilon]\epsilon_0 V^2 \frac{3WH}{8LD}. \tag{4.19}$$

In contrast, the deflection profile δ of a cantilever subject to an equivalent force F at its tip is different and given by,

$$\delta = Fk \frac{x^2(3L - x)}{2L^3}, \tag{4.20}$$

compared to the purely quadratic deflection that we find when driven electrostatically. While the electrostatically driven mode and the mechanically driven mode differ, the dot product of the normalized modes is 0.998, indicating that the modes are nearly identical.

The electrostatic force that deflects the cantilever is result of the competing effects of Maxwell stress and electrostriction. The magnitude of the resultant force non-monotonically depends on the relative dielectric permittivity of the dielectric layer. In particular the force is proportional to the effective relative permittivity given by $\epsilon - \Delta\epsilon$, which is plotted in Figure 4.2(c). Materials with high Poisson's ratio are preferable and for each Poisson's ratio there is an optimal dielectric constant which is larger for higher Poisson's ratio.

The deflection profile can also be derived directly by solving Eq. (2.1) with the boundary conditions that $\delta(0) = 0$, $\frac{d\delta}{dx}(0) = 0$, $\frac{d^2\delta}{dx^2}(L) = \frac{3[\epsilon-\Delta\epsilon]\epsilon_0 V^2}{DYT^2}$, and $\frac{d^3\delta}{dx^3}(L) = 0$.

4.2.5 Electrostatic driving

Driving the capacitor with an AC voltage enables direct driving of the mechanical mode of the cantilever. While the first vibrational eigenmode of a thin cantilever, as shown in Eq. (2.2), contains trigonometric and hyperbolic functions, the normalized dot product between the eigenmode in Eq. (2.2) and the quadratic deflection of Eq. (4.18) is 0.998. If the voltage is driven at a frequency near the mechanical resonant frequency f_0 of the cantilever. the first mode of the cantilever will be driven directly. We drive the capacitor with a voltage $V = V_{AC}\sin(2\pi ft) + V_{DC}$. The total DC potential drop across the capacitor includes a static potential ϕ_{static} that is due

to contact potential difference and static charge. Since F is proportional to V^2, there will be contributions at DC, f and $2f$. The DC contribution is difficult to separate from the static deflections due to tip-sample interactions and thermal drift. The term oscillating at f is a candidate for driving dynamic AFM, but it is complicated by the inclusion of the static potential ϕ_{static}. The term oscillating at $2f$ is the most convenient to use as ϕ_{static} and V_{DC} drop out. To drive the cantilever with the term oscillating at $2f$, the voltage is driven with $f = \frac{f_0}{2}$ and the oscillation is observed at f_0.

4.3 Experimental

We create self-driving cantilevers by the methods outlined in Chapter 3. A finished probe is shown schematically in Figure 4.1. The bottom face of a commercial AFM probe is coated with a shell electrode and the original conducting probe serves as the core electrode. Fabrication begins with commercial metalized probes (Arrow-NCPt – NanoWorld AG). Probes are coated in a 40 nm sticking layer of chrome and a 70 nm of low stress silicon nitride forms the insulating layer. A further ~2 μm insulating layer is deposited only on the body of the probe to reinforce it and a 30 nm / 50 nm bilayer of of chrome / gold to form the shell electrode.

Self-driving probes are tested in a commercial atomic force microscope (MFP3D – Asylum Research). The probes are clipped into the tip holder shown in Figure 3.9 in which the clip makes electrical contact to the shell electrode while the probe is pressed against electrodes that make electrical contact to the core electrode. The mechanical deflection of the probe is measured using the standard optical lever tech-

nique built into the commercial system The optical lever is calibrated by pressing the probe into a rigid substrate and comparing the change in laser deflection to the motion of the z-piezoelectric The spring constant of the cantilever is measured using the equipartition technique in which the rms thermal fluctuations of the cantilever are converted to a spring constant assuming each cantilever mode has energy $\frac{1}{2}k_BT$ where k_B is Boltzmann's constant and $T = 300$ K is ambient temperature Driving the cantilever with the $2f$ harmonic is accomplished using the commercial control software with a feature called dual AC mode The principle frequency is set to f_0 and the second frequency is set to $\frac{f_0}{2}$ but only the latter frequency receives any drive voltage Care must be taken to ensure that the ratio of the frequencies is precisely 1/2 otherwise the measured phase will drift throughout the measurement

4.4 Results

4.4.1 High fidelity driving

Driving the capacitive cantilever with an AC voltage electrostatically actuates the cantilever mechanically with high fidelity Figure 4 3(a) shows the the frequency spectrum of the oscillation amplitude A *vs* f of a capacitive cantilever that is driven mechanically by shaking the piezoelectric (left panel) and the same cantilever is driven electrically by applying $V_{AC} = 1$ V and $V_{DC} = 3$ V to the capacitor (right panel) The mechanical resonance is clearly visible as the drive signal is swept in frequency The amplitudes are fit to the amplitude of a driven damped spring-mass system, as given in Eq (2 6), and the fits are shown as grey lines When driven mechanically,

the fitting results in $f_0 = 243.2$ kHz and $Q = 521$ and when the same cantilever is driven electrically the fitting reveals similar values of $f_0 = 243.2$ kHz and $Q = 533$. The quality of the fit to the electrostatically driven oscillation is considerably better because the drive is coupled directly to the cantilever rather than mechanically through the tip holder.

Electrostatic driving is higher fidelity than mechanical driving when they are both driven at same amplitude A. Figure 4.3(b) shows a different but identically prepared capacitive cantilever driven such that the maximum amplitude observed for mechanical (left panel) and electrical (right panel) driving was the same. Here the electrical driving is stronger, with $V_{AC} = 5$ V and $V_{DC} = 5$ V. Mechanical driving produced a fit with $f_0 = 242.0$ kHz and $Q = 471$ while electrical driving results in a higher quality fit with $f_0 = 242.0$ kHz and $Q = 561$. An improvement in the fit quality over the mechanical driving is still seen in the electrical driving, so the improvement over mechanical driving persists when both methods produce comparable amplitudes.

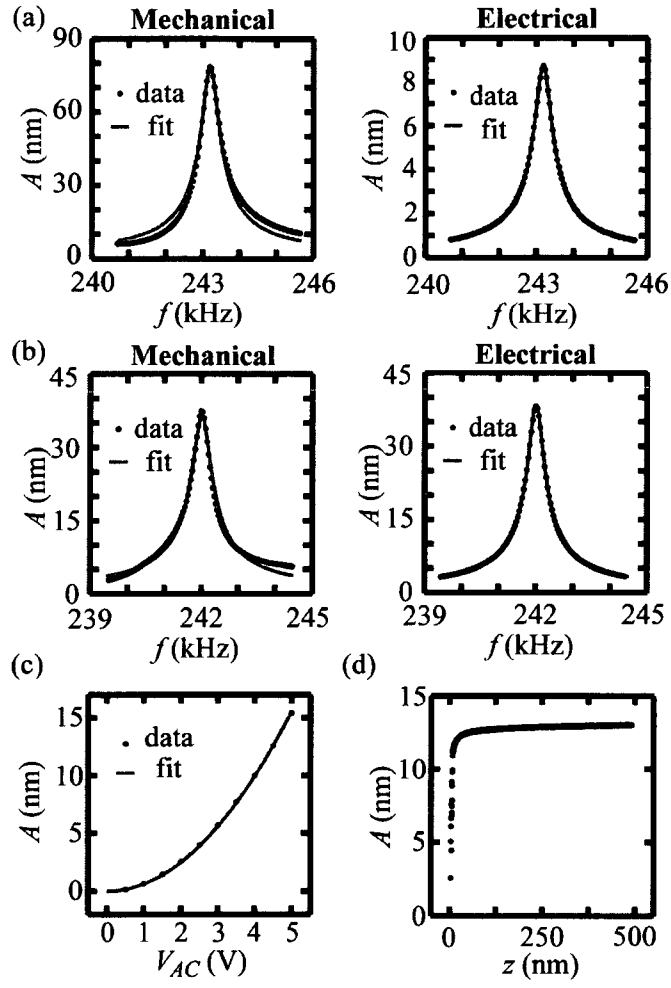

Figure 4.3: (a) The resonance peak of the mechanical oscillation amplitude A *vs.* driving frequency f of a capacitive cantilever when it is driven mechanically (left) and electrically (right). The electrical driving matches the theory much better than mechanical driving does owing to the local nature of the driving. (b) A *vs.* f of a different but identically prepared capacitive cantilever when it is driven mechanically (left) and electrically (right). Again, the electrical driving matches the theory better. (c) Amplitude of oscillation is measured with varying drive voltage V_{AC} and quadratic behavior is observed. (d) Amplitude of oscillation is seen to decrease monotonically as the tip-sample distance z is lowered, a prerequisite for amplitude modulation imaging.

4.4.2 Voltage dependance of driving

The amplitude A of the mechanical oscillation of capacitive cantilevers is measured to be quadratic with electrostatic drive voltage V_{AC} in agreement with our model of electrostatic driving. An RF voltage V_{AC} is applied at $f = \frac{f_0}{2}$ and the oscillation amplitude A is recorded at f_0. Driving with the frequency-doubled term removes the effect of DC potentials and static charge. Figure 4.3(c) shows A *vs.* V_{AC}. The data is fit to $A = \alpha V_{AC}^2$ and we find $\alpha = 0.62$ nm/V^2.

The oscillation amplitude can be predicted by our model for capacitive cantilevers and is in quantitative agreement with the experimentally observed value. The expected oscillation amplitude A is estimated by plugging the electrostatic force from Eq. (4.19) into the expression for A given in Eq. (2.6). If the cantilever is driven electrostatically at $f = \frac{f_0}{2}$, the frequency doubled term has the form, $\frac{1}{2}V_{AC}^2 \sin(2\pi f_0 t)$, resulting in an additional factor of $\frac{1}{2}$. The amplitude A is predicted to be,

$$A = \frac{3}{16}[\epsilon - \Delta\epsilon]\epsilon_0 V_{AC}^2 \frac{HWQ}{LDk}. \tag{4.21}$$

This model predicts $\alpha = 0.86$ nm/V^2 using manufacturer specified values, $H = 4.6$ μm. $W = 45$ μm, and $L = 160$ μm. We determined $k = 45.8$ nN/nm and $Q = 533$ from calibration, $D = 68$ nm from ellipsometry, and used $\epsilon = 7.8$, $\Delta\epsilon = 5.4$, and $\nu = 0.21$.[65, 66] The discrepancy between $\alpha = 0.62$ nm/V^2 as found experimentally and $\alpha = 0.86$ nm/V^2 from theory may be attributed to the deviation of the capacitive cantilever geometry from the cantilever ideal model and the sensitive dependence of $\Delta\epsilon$ on ν, which is poorly characterized in the literature.[65, 66]

4.4.3 Dynamic AFM with electrostatic driving

The oscillation is seen to depend weakly on tip-sample distance until short range tip-sample forces come into play, making this driving method ideal for amplitude modulation atomic force microscopy. Figure 4.3(d) shows the cantilever oscillation observed with $V_{AC} = 5$ V at $f = \frac{f_0}{2}$. The amplitude A of the oscillation is seen to decay monotonically with decreasing tip-sample distance z. The sharp decrease in A *vs.* z as the tip approaches the sample is the basis of tapping mode AFM imaging.

Electrically driven cantilevers can be used to take topographic AM-AFM images that have high quality. Figure 4.4(a) depicts a topographic scan of a calibration sample (CalibratAR 3D – Asylum Research) taken while shaking a capacitive cantilever mechanically. The calibration sample consists of a 200 nm deep trench in the middle of the image. Figure 4.4(b) is the same region imaged by driving the cantilever electrostatically. The same imaging quality is observed when driving the cantilever mechanically and electrostatically. Figure 4.4(c) is a electrically driven topographic scan taken of 13 nm tall gold electron-beam lithographically defined alignment numbers on a silicon dioxide substrate, demonstrating resolving nanometer scale features with electrostatic driving. In both Figures 4.4(b) and 4.4(c), the capacitive cantilever is driven the probe electrically with $V_{AC} = 5$ V at $f = \frac{f_0}{2}$, which corresponds to a free space oscillation of ~15 nm and the amplitude modulation set point was set to 8 nm.

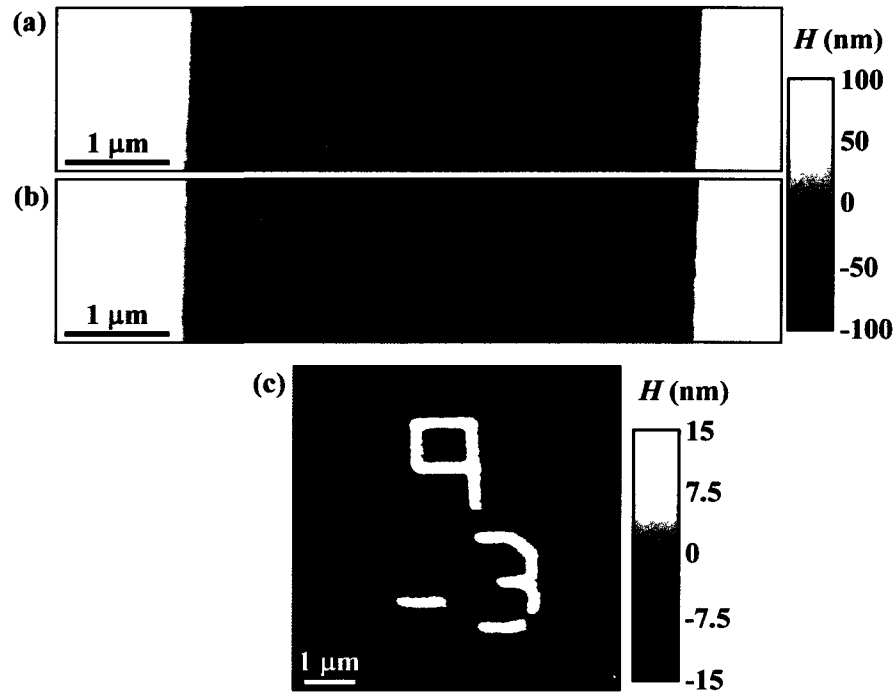

Figure 4.4: Comparison of tapping mode imaging with electrical and mechanical driving. (a) Topographic image of a calibration sample found while driving the probe mechanically. The sample consists of a 200 nm deep trench. (b) Topographic image of the same region taken while driving the probe electrically. The imaging quality is indistinguishable. (c) Topographic image of a nanostructured sample taken while driving the sample electrostatically. The pattern are metallic fiducial numbers patterned by electron beam lithography.

4.4.4 Contact resonance

One application where driving the mechanical mode with high fidelity is crucial is contact resonance.[41, 67] In this technique, the probe tip is held in contact with a surface and the change in the resonance frequency f_0 is observed. The tip-sample contact is treated as a Hookean spring with spring constant $k^\star$ which can depend on the tip and sample material properties, geometry, topography, and the force with which the tip is held to the substrate. The choice of spring constant is important as

this technique can only resolve $k^\star$ if $k \lesssim k^\star \lesssim 100k$.

The difficulty of performing contact resonance at high frequencies is illustrated in Figure 4.5(a) which is a trace of amplitude A *vs.* drive frequency f for a probe with a capacitive cantilever in contact with a glass substrate. The peak at 0.9 MHz is identified as the resonance peak of the cantilever while the spurious peaks between 0.5 and 0.9 MHz result from undesired mechanical modes of the probe-sample system. Because the probe is driven globally by shaking the cantilever, these modes are excited and make interpretation of the signal more difficult. The noisy mechanically driven signal is in contrast to the clean signal visible when the probe is driven electrically shown in Figure 4.5(b). In both panels, the same probe with a capacitive cantilever with $k = 34.7$ nN/nm and $f_0 = 242$ kHz is pressed into a glass slide to the same deflection set point corresponding to ≈ 200 nN of force. The electrically driven probe has $V_{AC} = 5$ V and $V_{DC} = 5$ V.

The contact resonance peak found when driving electrically is shown in Figure 4.5(c). Here, a linear background has been subtracted and the peak is fit to a Gaussian, shown in red. The peak is found to have a peak of 915 μV with $f_0 = 987$ kHz and $Q \approx 120$. The amplitude deviation ΔA about the background is shown as a histogram in Figure 4.5(d). The root-mean-square noise in the measurement is 120 μV from the standard deviation of the fit gaussian shown in red. The signal-to-noise ratio of this technique is therefore ≈ 8.

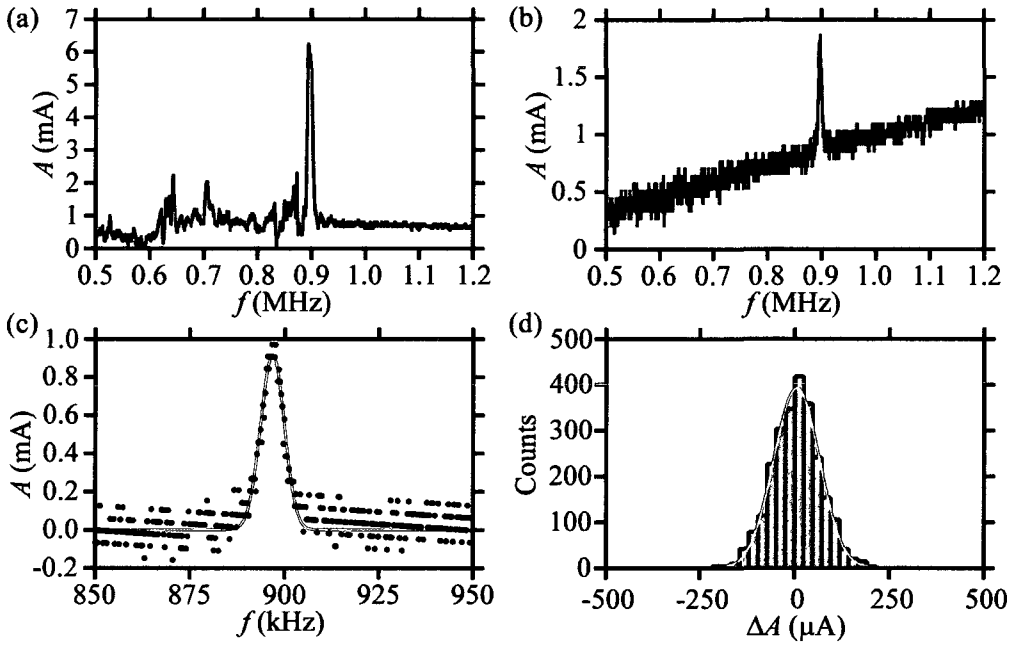

Figure 4.5: (a) Contact resonance peak in oscillation amplitude A *vs.* drive frequency f found while mechanically driving a capacitive probe while it is in contact with a glass substrate. The true contact resonance peak in A at $f \approx 900$ kHz is visible as well as many spurious peaks. (b) Contact resonance peak in A *vs.* f found by electrostatic driving with the same sample and capacitive cantilever. The spurious peaks are now gone while the true peak remains. (c) The contact resonance peak in A *vs.* f from (b) with the background subtracted and fit to a Gaussian. (d) The variation in amplitude ΔA from the background in the contact resonance measurement when driven electrostatically. The signal to noise ratio is found to be ~ 8 for this technique.

4.5 Discussion and Outlook

We have demonstrated that a thin film capacitor on the surface of a cantilever may be used as a mechanical drive for dynamic AFM techniques. The main application for this driving technique is situations where mechanical driving is impractical such as driving high frequencies or in liquid. Recently, self-sensing cantilevers with resonance frequencies up to 127 MHz have been developed.[57] At higher frequencies it is more

difficult to actuate and sense the motion of a cantilever. The internal electrostatic technique demonstrated here is only limited in frequency by the roll-off frequency $f_{RC} = (2\pi RC)^{-1}$ of the driving electrodes, which is $f_{RC} \sim 1$ GHz with a capacitance $C \sim 7$ pF and electrode resistance $R \sim 20\ \Omega$. Shorter cantilevers will have improved high frequency performance as $f_{RC} \propto L^{-2}$.

4.5.1 Capacitance sensing

The change in capacitance associated with bending is sufficiently large to be measured and could provide an additional way to sense the deflection of a capacitive cantilever. The fitting parameter α from Section 4.4.2 can also be expressed as,

$$\alpha = \frac{1}{2}\frac{Q}{k}\frac{dC}{dz}, \tag{4.22}$$

by recognizing that $F = \frac{1}{2}\frac{dC}{dz}V^2$. Using this expression we find $\frac{dC}{dz} = 0.11$ aFnm^{-1} for the cantilever in Figure 4(c). Further, the fractional capacitance change is $\frac{1}{C}\frac{dC}{dz} = 1.5 \times 10^{-8}$ nm^{-1}. High quality AC capacitance bridges can detect 1 part in 10^9 change in capacitance,[57] which would afford this technique ~1 Å resolution in deflection. Finally, the model predicts that the fractional change in capacitance $\frac{dC}{dz}$ improves with decreasing L if H is held constant,

$$\frac{1}{C}\frac{dC}{dz} = \frac{3}{8}\left[1 - \frac{\Delta\epsilon}{\epsilon}\right]\frac{H}{L^2} \tag{4.23}$$

A major challenge would be reducing the parasitic capacitance to keep the signal to background ratio high.

Chapter 5

High Resolution Kelvin Probe Force Microscopy with Coaxial Probes

5.1 Introduction

The principle reason for previous interest in coaxial probes has been their ability to create localized electric fields for imaging. Previous imaging with coaxial probes has included scanning near field microwave microscopy[31] and scanning conductance microscopy.[37] Kelvin probe force microscopy (KPFM) has proved to be a valuable tool for measuring the work function of a material.[6] In addition, KPFM is a useful for evaluating the spatial resolution of probes because it provides a quantitative signal, in contrast to the qualitative nature of many other electrostatic force microscopy techniques.[9]

In this Chapter, we demonstrate high spatial resolution Kelvin probe force microscopy (KPFM) using coaxial probes. In Section 5.2 we describe the principles of KPFM and how they are affected by the addition of the ground shield of a coaxial probe. Two experimental apparatuses to perform KPFM with a coaxial probe are presented in Section 5.3 along with a technique to calibrate them. In Section 5.4, we present KPFM data taken with a coaxial and an unshielded probe and find that the spatial resolution as determined by the width of a step is consistently improved by approximately an order of magnitude. Finally, in Section 5.5 we discuss the outlook of this technique and the relevance of complications due to static charge.

5.2 KPFM with Coaxial Probes

Here we describe the theory of how KPFM is used to measure the contact potential difference (CPD) between the sample material and the AFM tip.[6, 68] We then derive how the shell of a coaxial probe changes the electrical picture by describing the capacitances present in a coaxial AFM probe. Finally, we explain how to remove the electrical contribution from the shell electrode and measure the CPD between the tip and sample.

The electrostatic potential near the tip of an unshielded and a coaxial probe is shown in Figures 5.1(a) and 5.1(b) respectively. The electrostatic potential ϕ created by the unshielded probe shows spatial variation in regions far from the probe, and thus has long-ranged electric field components.[69, 14, 15] In contrast, the variation in ϕ simulated for a coaxial probe is localized at the tip and has no long range contributions. The improvement afforded by the coaxial probe is illustrated in Figure 5.1(c)

which shows the normal electric field on a conducting substrate 50 nm below each probe. The electric field from the coaxial probe is both stronger and more localized below the tip, completely lacking the long range shoulders of the unshielded probe.

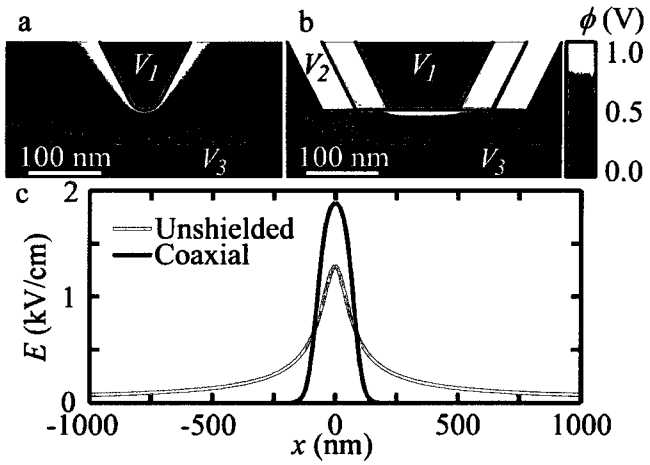

Figure 5.1: (a) Electrostatic simulation of the electric potential ϕ near the tip of an unshielded probe with $V_1 = 1$ V and $V_3 = 0$. The potential is seen to vary far from the probe tip. (b) Electrostatic simulation of ϕ near the tip of a coaxial probe with $V_1 = 1$ V and $V_2 = V_3 = 0$. The variation in ϕ is confined to the probe tip. (c) The electric field magnitude E on the substrate simulated for an unshielded and a coaxial probe. The field from an unshielded probe decays slowly away from the tip. The field from a coaxial probe is both more localized and stronger.

5.2.1 Kelvin probe force microscopy

Kelvin probe force microscopy is a technique to measure the local contact potential difference (CPD) between the sample and the tip.[68] The CPD between two materials is the difference between the work function Φ of the materials converted into a voltage using the charge e of an electron. The CPD between a conducting tip with work function Φ_1 and a sample with work function Φ_3 is given by $(\Phi_3 - \Phi_1)e^{-1}$. A schematic of a KPFM measurement is shown in Figure 5.2(a). A conducting AFM tip is capacitively coupled to a conducting substrate with capacitance C_{13}. The tip

and substrate are held at voltages V_1 and V_3 respectively. The energy U stored in the tip-sample capacitance can be written,

$$U = -\frac{1}{2}C_{13}\left(\left[V_1 + \Phi_1 e^{-1}\right] - \left[V_2 + \Phi_2 e^{-1}\right]\right)^2, \tag{5.1}$$

following the analysis in Section 2.4.1. Variation of U with respect to the tip-sample distance z gives rise to a force F given by,

$$F = \frac{1}{2}\frac{dC_{13}}{dz}\left(\left[V_1 + \Phi_1 e^{-1}\right] - \left[V_2 + \Phi_2 e^{-1}\right]\right)^2. \tag{5.2}$$

In a typical KPFM experiment, the sample is grounded ($V_3 = 0$) and the probe is driven with an AC and a DC voltage, $V_1 = V_{DC} + V_{AC}\sin(\omega t)$. The force from Eq. (5.2) is expanded as,

$$F = \frac{1}{2}\frac{dC_{13}}{dz}\left(\left[V_{DC} - \Delta\Phi_{31}e^{-1}\right]^2 + 2\left[V_{DC} - \Delta\Phi_{31}e^{-1}\right]V_{AC}\sin(\omega t) + \left[V_{AC}\sin(\omega t)\right]^2\right), \tag{5.3}$$

where $\Delta\Phi_{31} = \Phi_3 - \Phi_1$. We may simplify notation by defining $\frac{dC_{ij}}{dz} \equiv C'_{ij}$. Equation (5.3) contains constant terms, terms that oscillate at ω, and terms that oscillate at 2ω. Using the DC term as the signal is difficult as thermal drift and other tip-sample forces will complicate measurement. By choosing to operate at $\omega = \omega_0$ where ω_0 is the the mechanical resonance frequency of the cantilever, the term oscillating at ω will be amplified by the quality factor Q of the cantilever, as described in Eq. (2.6). The magnitude of F oscillating at ω is,

$$F_\omega = C'_{13}\left[V_{DC} - \Delta\Phi_{31}e^{-1}\right]V_{AC}. \tag{5.4}$$

In KPFM, V_{DC} is adjusted to null the amplitude A_ω oscillating at ω. When the oscillation is fully nulled $V_{DC} = V_K$, where the V_K is the Kelvin voltage and,

$$V_K = \Delta\Phi_{31}e^{-1}, \tag{5.5}$$

giving a measure of the CPD between the tip and sample. It is important to note that the Kelvin voltage V_K is defined as the DC voltage that nulls A_ω and may or may not be an accurate measure of the CPD, as we shall see in the following Sections.

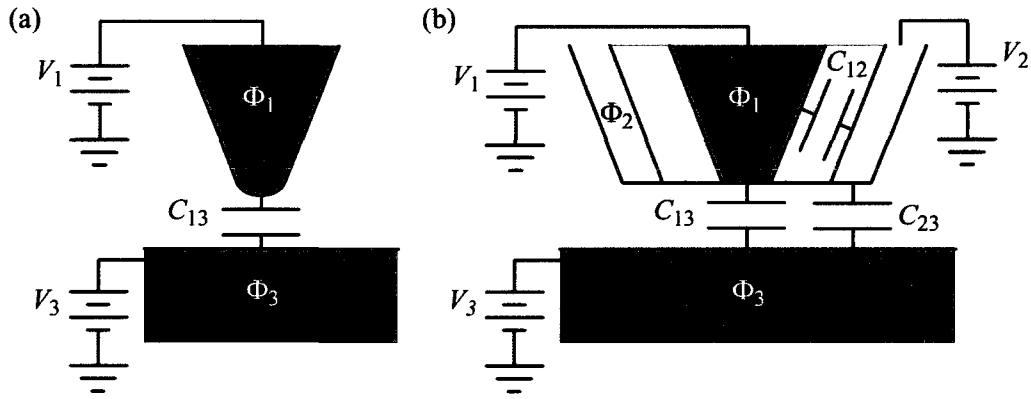

Figure 5.2: (a) Schematic of a conducting AFM probe capacitively coupled to a sample. The capacitive forces can be used to extract the contact potential difference. (b) Schematic of a coaxial AFM probe near a conducting sample. The presence of the shell electrode introduces another work function and two additional capacitances. Measurement of contact potential difference is still possible with the appropriate application of voltages.

5.2.2 Capacitances at the tip of coaxial probes

The principle change in the theory of KPFM operation with a coaxial probe is due to the presence of two additional capacitors. Figure 5.2(b) shows the capacitances at the tip of a coaxial probe. In addition to the tip-sample capacitance C_{13}, there also exists tip-shell capacitance C_{12}, and shell-sample capacitance C_{23}. These capacitances are calculated by finite element simulation of the coaxial tip geometry shown in Figure 5.3(a). Figure 5.3(b) shows the values of the capacitances as the tip-sample distance z is changed. The largest capacitance in the system is the tip-shell capaci-

tance C_{12}, without including the $\sim$ 1 nF capacitance from the rest of the cantilever and probe body

Examining the derivatives of the capacitances C with respect to tip-sample distance z shows that the shell electrode will influence KPFM measurements unless accounted for Figure 5 3(c) shows $C' \equiv \frac{dC}{dz}$ calculated from a finite difference calculation of the data shown in Figure 5 3(b) It is clear that C' is the relevant term as electrostatic forces are proportional to it, as seen in Eq (5 4) All values of C' decrease with increasing z C'_{23} has the largest magnitude, but so long as no AC voltage is applied to the substrate or the shell electrode, it will not contribute to F_ω C'_{13} and C'_{12} have opposite signs and have similar magnitudes There is a constant addition to C'_{12} from cantilever deflection changing the core-shell capacitance of the cantilever, as discussed in Chapter 4 5 1 This constant addition to C'_{12} is shown in Figure 5 3(c) as a dashed red line At a typical separation of $z = 50$ nm, $|C'_{12}| > |C'_{13}|$ so care must be taken to remove the effect of C'_{12}

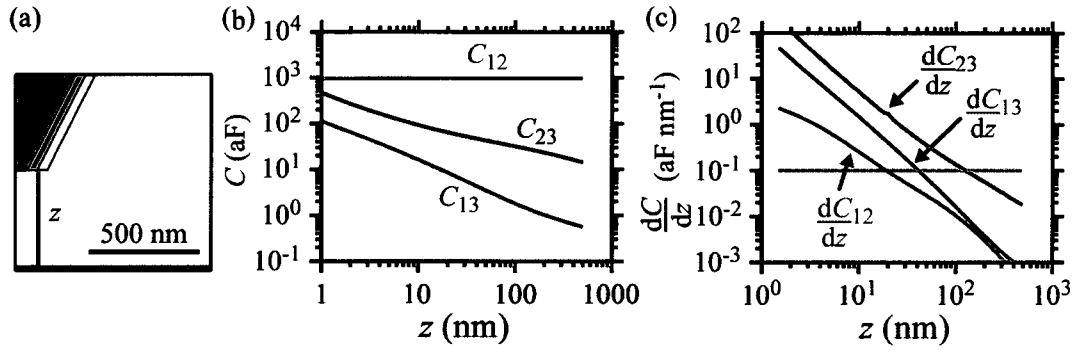

Figure 5.3: (a) Schematic of the geometry used in electrostatic simulation to determine capacitances. Here the coaxial probe has an insulating thickness $\lambda = 50$ nm. (b) Tip-sample capacitance C_{13}, tip-shell capacitance C_{12}, and shell-sample capacitance C_{23} calculated for the geometry shown in (a) as a function of tip-sample distance z. All capacitances depend on tip-sample distance z, although the variation in C_{12} is not visible on this scale. C_{12} is the largest capacitance in the system. (c) The magnitudes of C'_{13}, C'_{23}, and C'_{12} calculated by a finite difference method of the capacitances shown in (b). C'_{23} is the largest by nearly two orders of magnitude, so any AC excitation on the shell will create a dominating effect. The dashed line indicates the constant value of C'_{12} from the cantilever as described in Chapter 4. The similarity in magnitude of C'_{13} and C'_{12} indicates that both must be considered.

5.2.3 Kelvin probe with coaxial probes

The use of a coaxial probe for KPFM alters the Kelvin voltage V_K that sets $F_\omega = 0$.[48] The shell electrode of a coaxial probe introduces two additional capacitances, as depicted in Figure 5.2(b). Extending the analysis in Section 5.2.1 to determine the force on an unshielded probe, the force on a coaxial probe is,

$$F = \frac{1}{2}\frac{dC_{13}}{dz}\left(V_1 - V_3 - \Delta\Phi_{31}e^{-1}\right)^2 + \frac{1}{2}\frac{dC_{12}}{dz}\left(V_1 - V_2 - \Delta\Phi_{21}e^{-1}\right)^2 + \frac{1}{2}\frac{dC_{23}}{dz}\left(V_2 - V_3 - \Delta\Phi_{32}e^{-1}\right)^2, \tag{5.6}$$

where $\Delta\Phi_{21} = \Phi_2 - \Phi_1$ and $\Delta\Phi_{32} = \Phi_3 - \Phi_2$. The simplest configuration is to ground the shell electrode and the substrate ($V_2 = V_3 = 0$) and apply $V_1 = V_{DC} + V_{AC}\sin(\omega t)$.

By applying the voltages in this way, the force on the probe oscillating at angular frequency ω is,

$$F_\omega = V_{AC}\frac{dC_{13}}{dz}\left(V_K - \Delta\Phi_{31}e^{-1}\right) + V_{AC}\frac{dC_{12}}{dz}\left(V_K - \Delta\Phi_{21}e^{-1}\right). \tag{5.7}$$

Nulling F_ω yields a weighted average of the tip-sample and tip-shell CPDs. When the feedback is engaged to find V_{DC} that nulls F_ω, we find,

$$V_K = \frac{C'_{13}\Delta\Phi_{31}e^{-1} + C'_{12}\Delta\Phi_{21}e^{-1}}{C'_{13} + C'_{12}}. \tag{5.8}$$

The measured contact potential difference now depends on the tip-sample and tip-shell capacitances and both of these capacitances are non-trivial and depend on tip-sample distance z, as discussed in Section 5.2.2. Since C'_{13} and C'_{12} both depend on z means that attempting to measure the contact potential difference directly with this technique will yield poor results laden with topographic artifacts. This effect is commonly seen in scanning Kelvin microscopy, a non-AFM based technique to measure CPD, and is known as the stray capacitance problem.[70, 71, 72]

We have developed two methods of measuring the tip-sample CPD with a coaxial probe despite contributions from the shell electrode. The first technique is called the "active bias" because it incorporates active components while the second technique we call "passive bias" as it only uses passive components.

Active bias KPFM with coaxial probes

In the active bias technique, the true tip-sample CPD is measured by making sure the core and shell electrodes stay at the same DC voltage throughout the course of a measurement. This technique is borrowed from scanning kelvin microscopy in which

V_{DC} is also applied to ground shield.[72, 73] In order to account for the tip-shell CPD, we include a bias voltage V_S. As V_{DC} and V_{AC} are generated by the same digital to analog converter (DAC), we must separate V_{DC} from V_{AC}. The implementation of this method is shown in Figure 5.4(a). In this method, $V_1 = V_{DC} + V_{AC}\sin(\omega t)$, $V_2 = V_S + V_{DC}$, and $V_3 = 0$. The force is therefore,

$$F = \frac{1}{2}\frac{dC_{13}}{dz}\left(V_{DC} + V_{AC}\sin(\omega t) - \Delta\Phi_{31}e^{-1}\right)^2 + \frac{1}{2}\frac{dC_{12}}{dz}\left(V_{AC}\sin(\omega t) - V_S - \Delta\Phi_{21}e^{-1}\right)^2 + \frac{1}{2}\frac{dC_{23}}{dz}\left(V_S + V_{DC} - \Delta\Phi_{32}e^{-1}\right)^2. \tag{5.9}$$

Considering only the components oscillating at ω we find,

$$F_\omega = V_{AC}\frac{dC_{13}}{dz}\left(V_{DC} - \Delta\Phi_{31}e^{-1}\right) + V_{AC}\frac{dC_{12}}{dz}\left(-V_S - \Delta\Phi_{21}e^{-1}\right). \tag{5.10}$$

By applying feedback to change V_{DC} such that $F_\omega = 0$, the Kelvin voltage is,

$$V_K = \Delta\Phi_{31}e^{-1} + \frac{C'_{12}}{C'_{13}}\left(V_S + \Delta\Phi_{21}e^{-1}\right). \tag{5.11}$$

The first term in Eq. (5.11) is recognized to be the true tip-sample CPD while the second term is the contribution from the tip-shell capacitance which goes to zero if we set,

$$V_S^0 = -\Delta\Phi_{21}e^{-1}. \tag{5.12}$$

Passive bias KPFM with coaxial probes

In the passive bias technique, the true tip-sample CPD is measured by keeping the core electrode grounded while the feedback controls the voltage on the sample. This method uses a discrete element implementation of a "bias tee" in order to separate V_{AC} and V_{DC}. In this method, the tip is driven with only the RF excitation V_{AC}

while V_{DC} is applied to the substrate. A bias voltage V_S is applied to the shell electrode to ground it relative to the tip. The voltages on each electrode are therefore, $V_1 = V_{AC}\sin(\omega t)$, $V_2 = V_S$, and $V_3 = V_{DC}$. The force on the tip is,

$$F = \frac{1}{2}\frac{dC_{13}}{dz}\left(V_{AC}\sin(\omega t) - V_{DC} - \Delta\Phi_{31}e^{-1}\right)^2 + \frac{1}{2}\frac{dC_{12}}{dz}\left(V_{AC}\sin(\omega t) - V_S - \Delta\Phi_{21}e^{-1}\right)^2 + \frac{1}{2}\frac{dC_{23}}{dz}\left(V_S - V_{DC} - \Delta\Phi_{32}e^{-1}\right)^2. \tag{5.13}$$

Taking only the component oscillation at ω, we find,

$$F_\omega = V_{AC}\frac{dC_{13}}{dz}\left(-V_{DC} - \Delta\Phi_{31}e^{-1}\right)^2 + V_{AC}\frac{dC_{12}}{dz}\left(-V_S - \Delta\Phi_{21}e^{-1}\right)^2. \tag{5.14}$$

Which leads to the value of V_{DC} that sets $F_\omega = 0$,

$$V_K = -\Delta\Phi_{31}e^{-1} - \frac{C'_{12}}{C'_{13}}\left(V_S + \Delta\Phi_{21}e^{-1}\right)^2, \tag{5.15}$$

which is the opposite sign as the Kelvin condition of the active bias method from Eq. (5.11). As before, the bias voltage is appropriately set when,

$$V_S^0 = -\Delta\Phi_{21}e^{-1}. \tag{5.16}$$

The advantage of the passive bias technique is that the DC voltage on the core and shell electrodes is not changing during course of a measurement. Our implementation of the passive bias technique is shown in Figure 5.4(b).

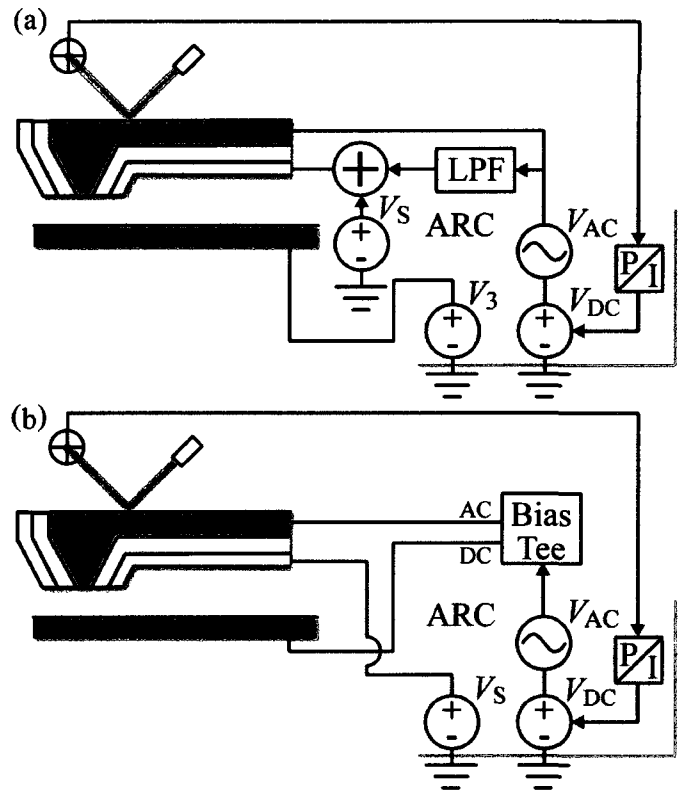

Figure 5.4: Circuit schematics of coaxial KPFM operated with active bias (a) and with passive bias (b). In both modes the control voltages are generated by the Asylum Research Controller (ARC) and some external electronics are needed to create the voltages necessary for operation.

5.3 Experimental

5.3.1 Electronics

Figure 5.4 shows a schematic of the electronics used to perform active bias (Figure 5.4(a)) and passive bias (Figure 5.4(b)) coaxial KPFM. Both apparatus utilize the Asylum Research Controller (ARC) to generate V_{DC} and V_{AC}. The motion of the cantilever in both techniques is measured with an optical lever technique in which

a laser is bounced off the cantilever and deflections are measured with a 4-quadrant photodiode The amplitude A and phase of the mechanical oscillation of the cantilever is used with a proportional-integral (PI) controller to adjust V_{DC} to set $A_\omega = 0$ The difference between the methods is primarily in how the control voltages are assigned to the electrodes of the system

In active mode, V_{DC} and V_{AC} are fed directly to the core electrode In addition, V_{DC} is separated by a 5 pole low pass RC filter with a corner at 25 kHz V_{DC} is then added to a bias voltage V_S created by an external voltage source (33220A Agilent Technologies) The adding is done by three operation amplifiers (OPA227P – Burr-Brown Corporation) in inverting mode Two potentiometers are used to tune the gain in order to insure that V_{DC} being reproduced with high fidelity An advantage of this technique is that the V_{DC} that the ARC is producing is being faithfully delivered to the tip, but a disadvantage of this method is that this setup is prone to falling out of calibration through drift

In passive bias mode, V_{DC} and V_{AC} are split by a bias tee implemented with discrete elements V_{AC} is separated by a 1 pole high pass RC filter with a corner frequency at 34 kHz, which passes 99% of V_{AC} to V_1 V_{DC} is separated by a 5 pole low pass LR filter with a corner frequency at 25 kHz, which attenuates V_{AC} by ~ -80 dB and allows V_{DC} to reach V_3 The shell bias voltage V_S is created by the Asylum research controller (ARC) and no external active components are needed The advantage of this technique is that it is stable and the AC field is completely removed from every electrode besides the core to reduce the possibility of the AC signal bleeding onto the shell electrode This method is also less susceptible to accumulation of

charge, as is discussed in Section 5.5.1.

Central to the operation of both the active and passive biased coaxial KPFM methods is separating V_{AC} and V_{DC}, and this must be done carefully for two reasons. (1) Any residual AC voltage on the shell electrode will have an enormous effect as the shell-sample capacitance is much greater than the tip-sample capacitance. (2) A typical cantilever resonance frequency is $\sim$ 250 kHz while the V_{DC} is being updated by the ARC feedback at 100 kHz giving a narrow window in frequency space to attenuate V_{AC} but allow V_{DC} to pass. Attenuating the high frequency components of V_{DC} leads to significant error in the feedback that manifests as mismatch between the trace and retrace in the measured V_K.

A Kelvin probe with coaxial tips is robust against electrical shorts in the insulating layer of the coaxial probe. The tip-shell capacitance of a coaxial probe is typically $C_{12} \sim 1$ nF, corresponding to an impedance of $\sim 600\ \Omega$ at $f = 250$ kHz. Such a low impedance indicates that low source resistances are necessary to avoid the AC voltages being present on the shell electrode. The voltages are all sourced inside the ARC by op-amps with low output resistance ($R_{out} \sim 1\ \Omega$) and the metal films of coaxial probes have $R_{Contact} \lesssim 5\ \Omega$, as described in Section 2.3. These low impedances allow the V_{DC} and V_{AC} to be delivered with high fidelity to the tip. The presence of pin-hole defects in the insulating film, typically with $R \sim 10\ \text{k}\Omega$, does not affect Kelvin operation.

5.3.2 Fabrication of coaxial probes for imaging

Probes are fabricated by the method outlined in Chapter 3. We use metalized probes (Arrow-NCPt – NanoWorld AG) which are coated in a 40 nm sticking layer of chrome, 70 nm of low stress silicon nitride, a ~ 2 μm insulating layer to reinforce the probe body, and a 30 nm/50 nm bilayer of of chrome/gold to form the ground shield. The coaxial electrodes are exposed with a focused ion beam etch. A typical finished probe is shown in Figure 5.5.

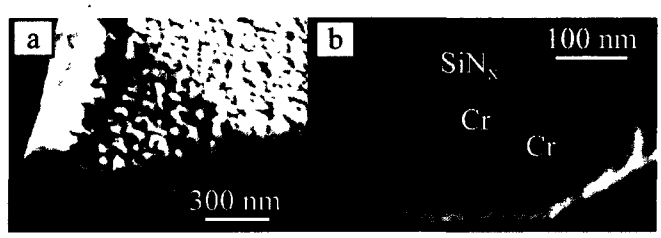

Figure 5.5: (a) Scanning electron micrograph of a coaxial probe used for high resolution electrostatic force microscopy. (b) A magnified view of the tip showing the chrome core electrode, silicon nitride insulating layer, and chrome/gold shell electrode.

5.3.3 Fabrication of reference samples

Fabrication of reference samples for Kelvin probe is subtle because the work function is extremely sensitive to the condition of the surface. Samples age rapidly due to surface contamination and oxidation so measurements must be accompanied by control measurements for quantitative comparison. Oxidation is particularly harmful as it can lead to charging of the surface causing drift during the course of single measurements. Metals such as gold and platinum that do not oxidize are preferable for this reason. An additional consideration is that the "dog ear" edge profile left by some photolithographic techniques can cause topographical artifacts that compli-

cate interpretation. For this reason, etching techniques or lift-off resists (LOR) are preferred.

We describe the fabrication of the two reference samples here. The first reference sample was a chrome/gold structure deposited on an doped silicon wafer. A 2" n+ doped silicon wafer is chemically cleaned and 30 nm of chrome and 30 nm of gold is deposited on the entire wafer by thermal evaporation. Photoresist (S1813 – Shipley) is spun on and a reference pattern of 20 μm wide lines separated by 20 μm is written on the sample by photolithography. After development and a post-exposure bake, the wafer is immersed in a potassium iodine gold-etchant (Gold Etchant Type TFA – Transene Company, Inc.) for 20 s to remove the exposed gold but leave the chrome beneath. The reaction is quenched in water and the residual photoresist is stripped with liftoff techniques. The etching method gives clean steps from gold to chrome but the reaction is not quenched uniformly and leads to step edge roughness.

The second reference sample was a gold/platinum structure deposited on an doped silicon wafer. a 9×9 mm^2 n+ doped silicon wafer chip that had been previously coated in 10 nm of chrome and 35 nm of gold is chemically cleaned and coated in a bilayer of a lift off resist (LOR 3A – MicroChem) and photoresist (S1813 – Shipley). A reference pattern with 5, 10, and 20 μm lines is imprinted with photolithography, the sample is developed, and 5 nm of titanium and 25 nm of platinum is deposited with electron beam evaporation. The remaining photoresist is lifted off with remover PG (MicroChem). Samples are stored in the dry box until they are measured.

5.3.4 Kelvin probe force microscopy

Kelvin probe measurements are taken as a two-pass technique using a commercial AFM (MFP-3D – Asylum Research) In the first pass, the AFM is driven mechanically and the topography is found by standard amplitude modulation AFM as described in Section 2 2 In the next pass, the probe retraces the previously captured topographic trace and the probe is driven electrically Feedback adjusts V_{DC} to minimize the cantilever amplitude A_ω The value of V_{DC} that minimizes the amplitude is recorded as V_K These interlaced scans are repeated to generate an image The AFM is typically scanned at 5 μm/s and the KPFM retrace is at done at the same tip-sample separation z as the topographic scan All images of V_K have the mean of each trace subtracted to reduce the effect of drift during the scan

5.4 Results

In this section, we describe initial results of performing KPFM with coaxial probes We start by showing that correctly setting the bias voltage V_S is important for coaxial KPFM by examining topographic artifacts while the probe is incorrectly biased We then describe how V_S is calibrated to remove the effect of the shell electrode Finally we demonstrate enhanced spatial resolution of coaxial probes on reference samples using both active bias and passive bias modes

5.4.1 Topographic artifacts with incorrect bias

To illustrate the effect of a coaxial KPFM measurement with V_S set incorrectly, we perform KPFM of a step between two regions of different metals while varying the bias voltage V_S. Topographic artifacts are a well documented problem in KPFM.[11] Figure 5.6 shows a sequence of traces of V_K measured while scanning a coaxial probe over a step of gold on the right and chrome on the left. Here, 30 nm of chrome is evaporated onto gold. The red line is a topographic trace with the vertical scale shown in the plot, a significant dog-ear is visible at the step. The correct V_S is determined to be $V_S^0 = 1228$ mV. When $V_S > V_S^0$, traces of the topographic feature are visible in V_K as peaks. Conversely, when $V_S < V_S^0$, traces of the topographic feature are visible in V_K as valleys. The influence of topography appears proportional to $V_S - V_S^0$ and underscores the importance of correctly biasing V_S in order to measure the true CPD.

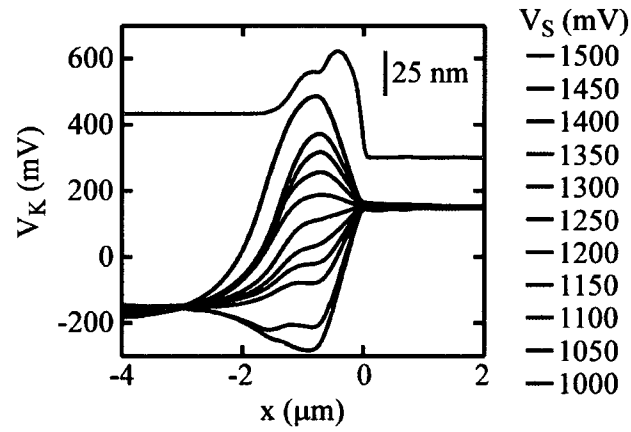

Figure 5.6: KPFM scans over a step from a region of gold ($x > 0$) to a region of chrome ($x < 0$). A topographic trace is shown as a red line and V_K is shown as the blue and black lines. Topographical artifacts are visible in every trace of V_K to varying degree. When V_S is near the true value of $V_S^0 = 1228$ mV, topographic artifacts are minimized.

5.4.2 Calibrating the bias voltage

Calibrating the bias voltage V_S on the shell electrode is necessary to be able to quantitatively measure the true tip-sample CPD. V_S can be found easily by grounding the shell electrode and engaging the KPFM feedback while macroscopically far from the sample. When the probe is many millimeters from the sample, $C'_{13} \to 0$ but $C'_{12} \neq 0$, because of the effects discussed in Chapter 4. Specifically, deflecting the cantilever always changes the tip-shell capacitance as the strain changes the tip-sample capacitance in the cantilever. A typical value for $C'_{12} = 0.11$ aFnm^{-1} as described in Section 4.5.1. If the feedback is engaged to adjust V_{DC} to set $A_\omega = 0$ while $V_2 = 0$, the resulting V_K is given in Eq. (5.8). Since $|C'_{13}| \ll |C'_{12}|$, $V_K = \Delta\Phi_{21}e^{-1}$. Setting $V_S = -\Delta\Phi_{21}e^{-1}$ results in a correctly calibrated coaxial KPFM probe.

The calibration can be verified by observing the effect of changing V_S on V_K while performing a Kelvin measurement. Figure 5.7(a) shows V_K measured while varying V_S above a uniform gold substrate using the active bias method. For each tip-sample separation z, V_K is seen to be linear with V_S, as predicted in Eq. (5.11), and the slope of that line is $\frac{C'_{12}}{C'_{13}}$. The point at which the lines intersect is where the probe is property calibrated and $V_S^0 = -\Delta\Phi_{21}$ Here we find $\Delta\Phi_{21} = -560$ mV.

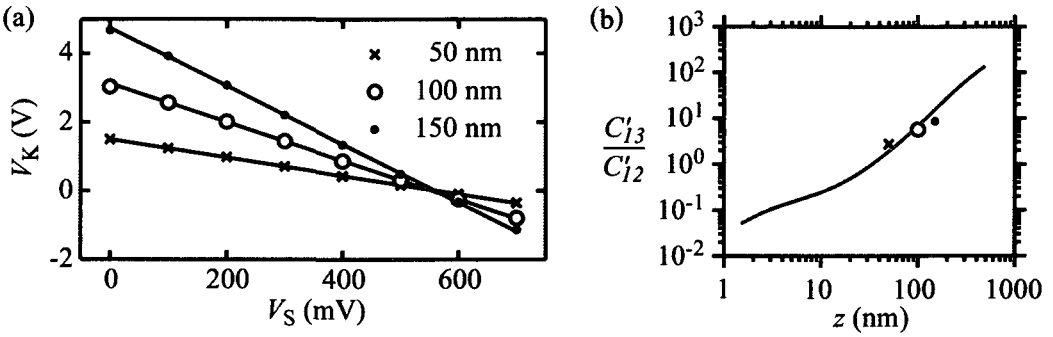

Figure 5.7: (a) Measured Kelvin voltage V_K while scanning over a uniform gold sample and varying the bias voltage V_S. At a given tip-sample separation z, V_K varies linearly with V_S, as predicted by Eq. (5.11), with slope equal to C'_{13}/C'_{12}. The intercept of the lines indicates the value of $V_S = V_S^0$. (b) Theoretical value of C'_{13}/C'_{12} simulated for the coaxial probe shown in Figure 5.3(a) including the cantilever contribution of $C'_{13} = 0.11$ aFnm^{-1}, as described in Section 4.5.1. The slopes of the three lines from (a) are included on the plot as the three points and show good agreement with theory (red curve) without fitting.

The measured values of $\frac{C'_{12}}{C'_{13}}$ are also used to validate our model of the capacitive interactions in coaxial KPFM. These slopes of linear fits of Figure 5.7(a) are shown in Figure 5.7(b) as points. The red line indicates the theoretical prediction made by combining the simulated capacitance from Figure 5.3 and the value of C'_{12} measured for a similar cantilever as described in Section 4.5.1. The line is not a fit but rather a comparison of the data with our theoretical prediction. The agreement indicates that our model for the electrostatic interactions in this system is accurate.

5.4.3 Enhanced resolution with Kelvin Probes

Figure 5.8 shows enhanced spatial resolution of a coaxial probe through KPFM measurements of a chrome/gold step using active bias to account for the shell electrode. Figure 5.8(a) shows an the Kelvin image of the step generated by an unshielded

probe. As the probe passes from a uniform region of gold on the the left to a uniform region of chrome on the right, V_K is seen to slowly transition across the image. In contrast, Figure 5.8(b) shows a different region of the same sample imaged with a coaxial probe. The transition appears much steeper. The improvement in resolution is more readily seen in Figure 5.8(c) which shows the average line trace of each method. In this plot, each line trace is shifted to be centered about the step and then averaged together. The step imaged by a coaxial probe is both sharper and more quickly reaches the maximum value. The resolution D_{step} can be estimated as the distance to traverse 25% to 75% of the step height. We find that unshielded probe $D_{step}^{Unshielded} = 1150$ nm while $D_{step}^{Coaxial} = 123$ nm, exhibiting nearly an order of magnitude improvement. This experiment was performed with active bias with $V_S^0 = 335$ mV on an etched chrome/gold sample as described in Section 5.3.3.

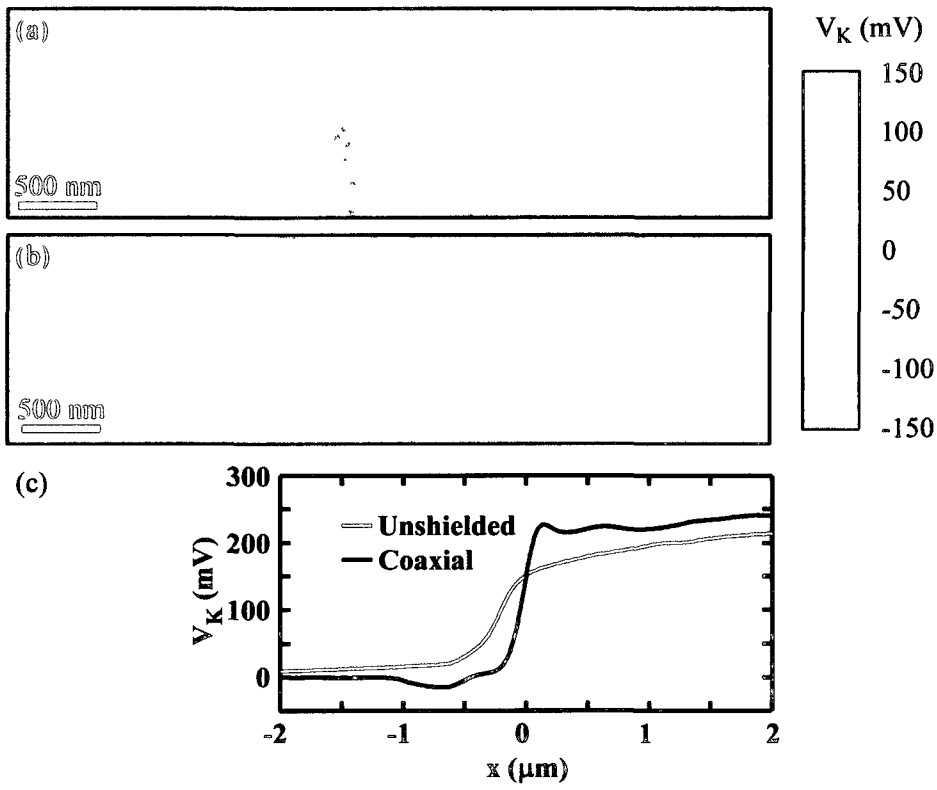

Figure 5.8: (a) Unshielded KPFM measurement of a chrome/gold step. Considerable blur is visible at the step from gold on the left to chrome on the right. (b) Coaxial KPFM measurement of the same chrome/gold step. The image appears much sharper. (c) Each line traces from (a) and (b) are centered about the step and averaged to form the average step function for unshielded (red) and coaxial (black) probes. The coaxial step looks considerably sharper. The distance necessary to rise from 25% to 75% of the step for the coaxial probe is nearly an order of magnitude smaller than that for the unshielded probe.

Figure 5.9 shows enhanced the spatial resolution of a coaxial probe through KPFM measurements of a gold/platinum metallic step using passive bias to account for the shell electrode. Figure 5.9(a) shows V_K generated by an unshielded probe. Here the transition from gold on the left to platinum on the right is located off-center to the left. V_K is seen to slowly transition across the image. The image width corresponds to the maximum scan range of the AFM and the image center was chosen to highlight the

slow transition on the right side of the step due to the cantilever. Figure 5.9(b) shows a different region of the same sample imaged with a coaxial probe. The transition in V_K is much sharper. The improvement in resolution is apparent in Figure 5.9(c) which shows the average line trace of each method. Each line trace is shifted to overlay the middle of each step before averaging. As before, the step imaged with a coaxial probe is both sharper and more quickly reaches the saturated value. We find that unshielded probe $D_{step}^{Unshielded} = 13$ μm; the variation between this and the previous experiment can be attributed to the previous experiment having a smaller scan width and not reaching the saturated value. For the coaxial probe, we find $D_{step}^{Coax} = 540$ nm, which is approximately 25$\times$ smaller than the step measured with an unshielded probe. The coaxial probe in this measurement is larger, the tip was 700 nm wide, *vs.* a 400 nm wide probe used in Figure 5.8. This experiment was performed with passive bias with $V_S^0 = 1.77$ V on a gold/platinum sample described in Section 5.3.3.

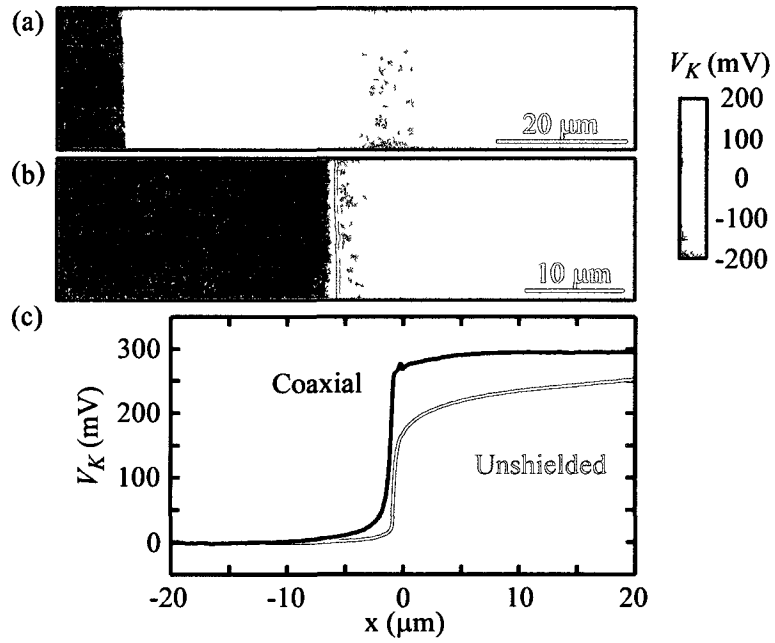

Figure 5.9: (a) Unshielded KPFM measurement of a sample with a gold/platnimum step. Considerable blur is visible at the step from gold on the left to platinum on the right. (b) Coaxial KPFM measurement of the same gold/platinum step. The image appears much sharper. (c) Average step of the above images; the coaxial step looks considerably sharper. The length to rise from 25% to 75% of the step for the coaxial probe is approximately 25× times smaller than that for the unshielded probe.

5.5 Discussion and Outlook

We have demonstrated that coaxial probes can image contact potential difference (CPD) with much higher spatial resolution than unshielded probes. The improvement in resolution comes from two effects. (1) The cantilever and cone of an AFM probe is responsible for interactions that spans dozens of microns, as is evident in Figure 5.9(a). The electrostatic shielding prevents the cantilever and cone from having any effect on the measured CPD. (2) As will be discussed in depth in Chapter 6, the electric field from a coaxial probe is similar to the field produced by an electric dipole. A

dipolar field decays more quickly than the monopolar field produced by the tip of an unshielded probe The latter effect is an important motivating factor for coaxial KPFM There exist frequency modulation (FM) techniques to measure CPD in which the signal is proportional to $\frac{d^2C}{dz^2}$ rather than $\frac{dC}{dz}$ as in amplitude modulation (AM) KPFM [74, 75] The second derivative largely eliminates the electrostatic contribution from the cantilever and cone The fact that a coaxial probe behaves like a dipole indicates that a coaxial probe still offers an advantage over FM-KPFM and if a coaxial probe is used with FM-KPFM would further improve the spatial resolution

5.5.1 Drift due to static charge

According to the model of coaxial KPFM presented here, coaxial probes are calibrated when $V_S^0 = -\Delta\Phi_{21}e^{-1}$ This does not fully account for the behavior of the coaxial probes, as evidenced by the fact that we find probes prepared in the same way are calibrated by different values of V_S^0, and that V_S^0 can drift over the course of a measurement We believe the dominant cause of drift and the variation in V_S^0 between probes is due to static charge in the insulating layer of coaxial probes It is well known that KPFM is sensitive to static charge[76] and that PECVD films are subject to trapped charge [77]

Passive bias mode helps mitigate the effects of static charge As discussed in Section 5 3 4, KPFM measurements are performed in a two-pass technique where KPFM scans are interlaced with tapping mode scans to determined the sample topography During the topographic lines, $V_{DC} = V_{AC} = 0$, and the sudden changes in voltage can lead to a buildup of static charge In passive mode, the DC voltages on the shell

and core electrode do not depend on V_{DC} created by the ARC so they stay constant throughout the entire measurement. For this reason, passive bias is less sensitive to accumulation of static charge.

Chapter 6

Dielectrophoretic Imaging and Manipulation with Coaxial Probes

6.1 Introduction

The atomic force microscope (AFM) has been used for an increasingly diverse set of applications. Among these, the AFM has gained interest as a tool for precision nanoassembly of single devices and parallel assembly at a large scale. Single nanoparticles are commonly positioned by physically sliding them along surfaces with the tip of an AFM [17, 18, 19, 20]. Microscale particles can be assembled by lifting them using two coordinated AFM probes [24, 25]. A long standing goal is to produce a pick-and-place tool that can image with high spatial resolution, pick up single microscale particles, and deposit them in a specified location. Such a tool would enable the assembly of microscale structures as well as granting the AFM probe flexibility to image with a multitude of functional microparticles.

In this chapter, we discuss the use of a coaxial probe, as shown in Figure 6.1(a), to image and manipulate materials at the nanoscale with dielectrophoresis (DEP). We begin by showing that coaxial probes produce electric fields that are well approximated by the electric field of a dipole.[78] The theory illustrating how an electric dipole may be used to image objects with DEP is presented. We measure the DEP force between a coaxial probe and a substrate and find it to be in agreement with the dipole model. Silica beads are imaged with DEP and we demonstrate high fidelity imaging that is in quantitative agreement with the dipole model. Finally, we use a coaxial probe to perform three dimensional pick-and-place of a single silica bead.[79] The combination of the ability to image with high resolution using DEP and perform pick-and-place makes coaxial probes a versatile tool for nanotechnology.

6.2 Coaxial Probes as Electric Dipoles

Coaxial AFM probes create an electric field that is well approximated by a dipolar electric field. Figure 6.1(a) shows an electrostatic simulation (Maxwell 2D - Ansoft) of a coaxial probe with an insulator of thickness $\lambda = 500$ nm. In this simulation, the core electrode is held at $V = 1$ V and the shell electrode is grounded. The electric field is localized at the tip and falls off quickly away from the tip. In particular, the electric field E along the z-axis is shown in Figure 6.1(b) as red dots. Here the field has been scaled to reach the maximum breakdown electric field in air in ambient conditions of $E_{BD} = 0.75$ MV/cm.[55] The electric field is constant near the tip but then falls off quickly. This field is fit very well to the electric field of a dipole of

moment p located a distance L_p into the tip,[46]

$$E_z = \frac{p}{2\pi\epsilon_0}\frac{1}{(z+L_p)^3}, \tag{6.1}$$

shown as the red line in the plot.

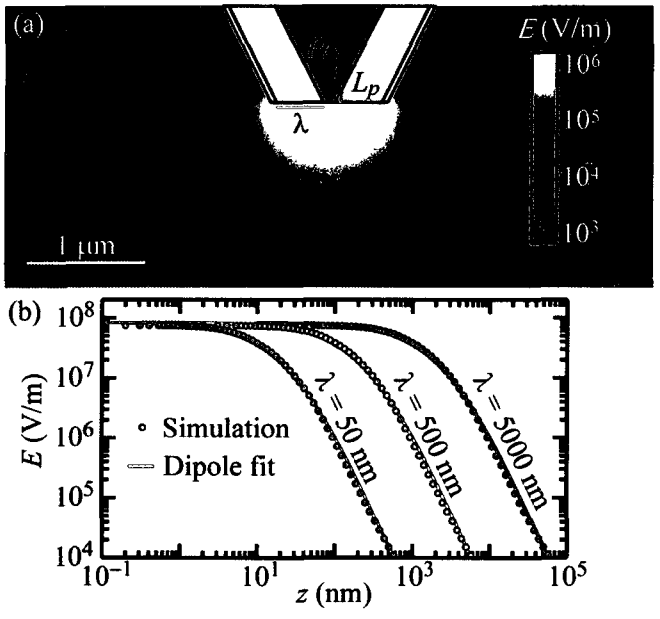

Figure 6.1: (a) Electrostatic simulation of a coaxial probe with a voltage V applied to the core electrode with the shell electrode grounded. Here the inner conductor is held at 1 V while the outer conductor is grounded. The electric field is well approximated by a dipole of moment p held a distance L_p inside the probe. (b) The electric field E on the z-axis simulated for three probes with varying insulator thickness λ is shown as dots of different color. The field of each probe is scaled such that the maximum field is the breakdown field E_{BD} of air. The electric field of a dipole fits the simulated field very well and is shown for each simulated geometry as a solid line.[78]

The location and strength of the electric dipole scales with the size of the probe, which is useful for selecting the optimum size of a probe. The electrostatic simulation was repeated with $\lambda = 50$ nm and $\lambda = 5000$ nm and the results are shown as grey and blue dots in Figure 6.1(b) respectively. The maximum electric field calculated for these probes has also been scaled to reach the breakdown field E_{BD} in air. The

electric field of these probes also very well fit by Eq. (6.1), as shown by the grey and blue curves. All three probes are well represented by dipoles with,

$$L_p = 0.75\lambda, \tag{6.2}$$

and

$$p = 26\epsilon_0 V \lambda^2. \tag{6.3}$$

For the maximum voltage that can be applied to a given probe without dielectric breakdown, the dipole moment is,

$$p = 9.1\epsilon_0 E_{BD} \lambda^3. \tag{6.4}$$

The DEP force $F_{substrate}$ between a coaxial probe and a substrate may be calculated with the dipole model and is found to be independent of tip size. The electric field produced by a probe dipole a distance z above a dielectric half plane of permittivity ϵ_2 can be found by the method of images. In addition to the field from the original dipole, there is an image dipole located at $-z$ with a moment given by,[80]

$$p' = -p\frac{\varepsilon_2 - \varepsilon_0}{\varepsilon_2 + \varepsilon_0}. \tag{6.5}$$

The force $F_{substrate}$ on the probe dipole due to the substrate is given by $F_z = p\frac{\delta E_{p'}}{\delta z}$ which is,

$$F_{substrate} = -\frac{3p^2}{16\pi\epsilon_0}\left(\frac{\varepsilon_2 - \varepsilon_0}{\varepsilon_2 + \varepsilon_0}\right)\frac{1}{z^4} \tag{6.6}$$

The force from a coaxial probe resting against a substrate can be calculated by substituting $z = L_p$ and using the value for p from Eq. (6.3) to find.

$$F_{substrate} \approx 127\epsilon_0 V^2 \left(\frac{\varepsilon_2 - \varepsilon_0}{\varepsilon_2 + \varepsilon_0}\right). \tag{6.7}$$

For a coaxial probe resting on silicon with $\epsilon_2 = 11.68\epsilon_2$, we find $F_{substrate} = 0.95$ nN/V^2 $\times$ V^2 from Eq. (6.7). This result is independent of λ, although the maximum force is not, as λ will determine the maximum V that can be applied. If the electric field is oscillating, it is appropriate to use the root-mean-square of V.

The DEP force on a coaxial tip, modeled as a dipole can also be used to image materials with the position dependant DEP force. Figure 6.2(a) illustrates a dipole a distance z above a substrate on which a dielectric sphere of radius a rests. The dipole is a distance ρ to the side of the sphere and the dielectric constants of the sphere and substrate are ϵ_1 and ϵ_2 respectively. The force from the substrate is estimated from the method of images and is given in Eq. (6.6). To first order, the force on the dipole from the sphere is the dielectrophoretic force on the sphere from the dipole in the absence of the substrate. The z-directed DEP force from on the dipole from the sphere is found to be,

$$F_{sphere} = -\frac{3p^2a^3}{\pi\epsilon_0}\left(\frac{\varepsilon_1 - \varepsilon_0}{\varepsilon_1 + 2\varepsilon_0}\right)\frac{(z-a)^3}{([z-a]^2+\rho^2)^5}. \tag{6.8}$$

The total force on the dipole just above ($z = 2a$) a sphere and substrate with $\epsilon_1 = \epsilon_2 = 3.8\epsilon_0$ is given in Figure 6.2(b). The peak in the force curve provides a direct way to localize the dielectric object, allowing it to be imaged.

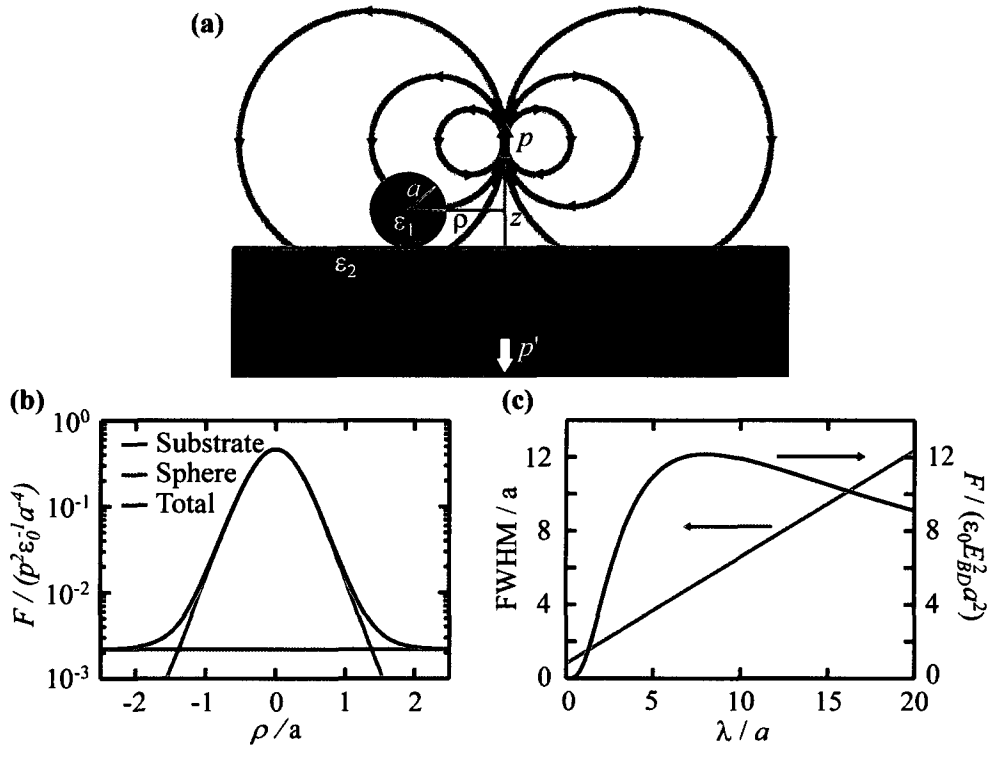

Figure 6.2: (a) Schematic of the model system of a dipole imaging a dielectric sphere. A dipole p is a distance z above a substrate and a distance ρ to the side of a dielectric sphere of radius a. The sphere has permittivity ϵ_1 and the substrate permittivity ϵ_2. An image dipole p' is formed in the substrate. (b) The DEP forces on a dipole as it is slid over the top of a sphere with $z = 2a$ and $\epsilon_1 = \epsilon_2 = 3.8\epsilon_0$. The force F_{Sphere} from the sphere is shown as a red line, $F_{Substrate}$ is a blue line, and their sum is depicted as a black line. The force is peaked above the sphere, indicating that this force may be used to localize the sphere. (c) The resolution and sensitivity of a coaxial probe with insulator thickness λ while imaging a dielectric sphere of radius a when the probe is held directly against the sphere, so the probe dipole is at a height $z = 2a + L_p$. The full-width at half-max (FWHM) is given as a red line and monotonically increases as the probe is made larger. F_{Sphere} is given as a black line and increases with increasing λ for $\lambda < 8a$. These plots illustrate the tradeoff between higher sensitivity with larger probes but better resolution with smaller probes.[78]

The scaling relationship between the insulating layer thickness λ of a coaxial probe and the location and strength of its effective dipole moment leads to a prediction for the optimum probe size to image a given object. The spatial resolu-

tion is estimated by calculating the full-width at half-max (FWHM) to be FWHM $= 2\left(a + 0.75L_p\right)\left(2^{1/5} - 1\right)^{1/2}$. The FWHM is plotted in Figure 6.2(c) as a red line. The sensitivity is given by the maximum force resultant from a given sphere. The maximum force is plotted in Figure 6.2(c) as a black line. While the resolution gets consistently worse as the tip is made larger, the sensitivity rises quickly and peaks at $R = 8a$.

6.3 Probe Fabrication and Sample Preparation

6.3.1 Coaxial probes for DEP imaging and manipulation

Coaxial probes were fabricated by the method outline in Chapter 3. Uncoated silicon probes were used (Arrow-NC – Nanoword AG) with Ti/Al Ohmic contacts, 500 nm insulating layers made of low stress SiN_x, and an outer conductor formed by 15 nm of Cr and 30 nm of Au. A typical probe is shown in Figure 6.3. The cantilever extends off the right edge of the image and the tip is visible in the top left corner. The inset shows the a magnified view of coaxial electrodes and labels of the films at the tip.

Figure 6.3: Scanning electron micrograph of a typical coaxial AFM probe for DEP imaging and manipulation.[78] The inset shows a magnified view of the coaxial electrodes in which the triangular inner conductor is visible.[79]

6.3.2 Test samples of silica beads

Reference samples for dielectrophoretic imaging and analysis were made by depositing silica beads on flat substrates. Three types of substrates are used: glass slides (VWR), silicon wafers (Silicon Quest International), and silicon wafers that have had their surface roughened by a reactive ion etch (RIE) method.[81] To roughen wafers, S1813 photoresist is spun onto the wafer and it is soft baked. The sample is then etched in a reactive ion etch at 20 mTorr with 20:4 sccm of SF_6:O_2 for 26 min, which increases the surface roughness from $\sim$ 1 nm_{RMS} to $\sim$ 16 nm_{RMS} by imprinting the inhomogeneity of the resist onto the substrate. The surface roughness decreases adhesion making it easier to remove particles from the surface.[28, 82, 52] Before use, substrates are chemically cleaned thoroughly. Cleaning begins with a 20 min sonication in acetone, then a 10 min soak in boiling trichloroethylene on a 140 °C hot plate, followed by a 10 min sonication in acetone, ending in a 10 min. sonication in methanol. Substrates are then blown dry with N_2 and stored in a dry box until measurements.

Silica beads are deposited on a substrate to provide topographical features and particles to manipulate. Polyscience 1 ± 0.05 μm diameter size standard beads were centrifuged (3 min at 5000 rpm in Model V microcentrifuge – VWR Scientific) to separate the beads from the stock suspension. The original suspension is pipetted out and the beads are resuspended in either deionized (DI) water or isopropanol. The suspension is pipetted onto the cleaned substrate and allowed to dry in a vacuum chamber. The choice of solvent affects the configuration of beads, isopropanol has lower surface tension and results in less clustering while the solvent is evaporating. This provided isolated beads where as the DI suspension tended to produce more close-packed structures.

Experiments are performed in a dry environment to minimize capillary adhesion. Dry air is flowed into the AFM enclosure and the relative humidity is monitored by a portable humidity meter. Experiments were performed with the relative humidity below 20%, the lower limit of the humidity meter.

6.3.3 High voltage electronics

Dielectrophoresis driving voltages are created by by running a function generator through a high voltage power supply (BOP 500 – Kepco), which has a gain of 50×. The current and voltage are tracked (177 Microvolt DMM – Keithley Instruments Inc.) to record the drive voltage and ensure that current is under $\sim$ 1 mA. Currents of $\sim$ 1 mA are typical capacitive displacement currents while currents $\gg$ 1 mA indicate that the insulating layer has broken down and the probe is no longer usable.

6.4 Dielectrophoresis on a Substrate

Force-distance curves reveal that application of an electric field increases the force required to remove a coaxial AFM probe from a substrate. Force-distance measurements F *vs.* z are performed with coaxial AFM probes in which the probe is moved towards the substrate at 100 nm/s until the cantilever reaches a deflection set point, corresponding to a deflection of $\sim$ 22 nm.[83] The cantilever is then withdrawn. A typical F *vs.* z curve with no applied voltage is shown in Figure 6.4(a) in which the red curve depicts the approach and the black curve depicts the withdrawal. The jump into contact is due to short range attractive forces and the linear deflection is indicative of Hookean deflection of the cantilever once it is in contact. The largest attractive force during withdrawal is denoted F_{PO} and represents the sum of the attractive forces experienced when the tip is near the substrate. Now we apply $V = 20\ V_{RMS}$ at 5 kHz to the tip and repeat F *vs.* z, as shown in Figure 6.4(b). Here, F_{PO} has dramatically increased, demonstrating that the applied voltage increases the attractive forces between the tip and substrate.

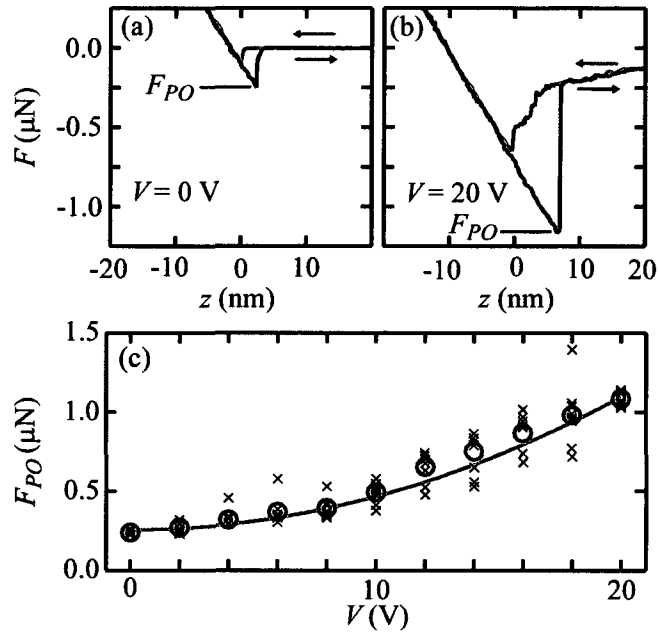

Figure 6.4: (a) Force-distance curve F *vs.* tip-sample separation z taken by a coaxial probe against a polished silicon substrate. The red line indicates the descent and the black line indicates the withdrawal. The linear portion indicates that the tip is in contact and the cantilever is bending linearly. The largest attractive point during the withdrawal is denoted the pull-off force F_{PO} and is the sum of all forces attracting the tip to the substrate. (b) Force-distance curve taken on the same sample with 20 V_{RMS} applied to the tip. A much larger F_{PO} is observed. (c) Pull-off forces F_{PO} observed from many F *vs.* z curves taken at different voltages V. Each 'x' indicates an individual measurement while the 'o' indicates the average at a given voltage. The averages are fit to a quadratic term plus an offset, shown in red, in good agreement with adhesion plus DEP.[79]

The result of many F *vs.* z curves indicate F_{PO} includes a contribution from DEP in agreement with the dipole model of coaxial probes. Figure 6.4(c) shows the pull-off force F_{PO} from many F *vs.* z curves at different voltages V where each 'x' indicates a separate measurement and each 'o' is their average at a given V. The average values are well fit by $F_{PO} = \beta + \alpha V^2$ with $\alpha = 2.10 \pm 0.04$ nN/V^2 and $\beta = 256 \pm 9$ nN, as shown as the red curve in Figure 6.4(c). Here, β represents

stiction forces and the quadratic relationship between F_{PO} and V is in support of a contribution from dielectrophoresis. Further, the experimentally determined value for α is good agreement with attractive force predicted by the dipole model, as described in Eq. (6.7), which yields $\alpha = 0.95$ nN/V^2. The only parameter of this model is the dielectric constant of the substrate, which we take to be $\epsilon_2 = 11.68\epsilon_0$ from silicon.

6.5 Imaging with Dielectrophoresis

A coaxial probe can image with dielectrophoresis to improve its imaging ability. A consequence of a blunt coaxial probe is that topographical images of objects may contain artifacts of the tip shape. Figure 6.5(a) shows a close-packed monolayer of 1 μm diameter silica beads imaged in tapping mode by a coaxial probe. The triangular artifacts are due to the size similarity between the probe and the beads. Now, a voltage $V = 40$ V$_{RMS}$ at 5 kHz is applied to the tip and the same region is imaged again with the same imaging parameters, the result is Figure 6.5(b). The beads are clearly visible and appear symmetric. The probe is now operating in a non-contact regime as the attractive force is sufficient to lower the amplitude sufficiently to engage the feedback.

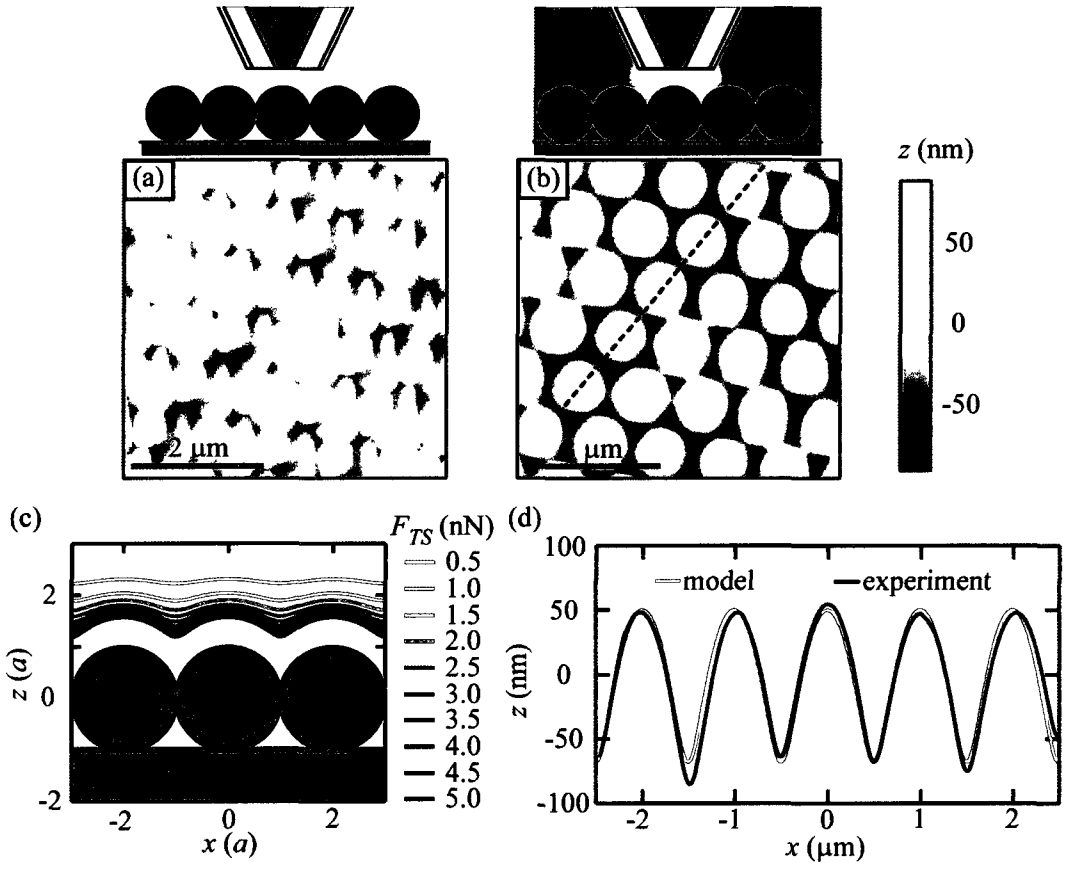

Figure 6.5: (a) Tapping mode image of a close-packed monolayer of 1 μm diameter silica beads. Artifacts of the tip shape are visible in the image due to the similar size of the tip and features. (b) Topographic image taken with the same imaging parameters with V=40 V_{RMS} applied to the tip at 5 kHz. The beads now appear symmetric and are clearly distinguished. The beads are now being imaged without contact and the dominant interaction is DEP. The tip-sample force may be estimated from imaging parameters to be F_{TS} = 2.9 nN. (c) Contours of constant force calculated for a dipole above a close-packed monolayer of silica beads. The lighter lines indicate a lower force. (d) A least-squares fit of the contours of constant force shown in (c) to the topographic trace shown as a dashed line in (b). The fit provides an estimate of the tip-sample force F_{TS} = 2.1 nN, in good agreement with the experimentally determined value, indicating that the coaxial probe is behaving as an electrical dipole.[78]

A dipole model of the tip provides excellent agreement with topographical scans of the silica beads. We find agreement between a topographic line trace from Figure 6.5(b) and a contour of constant force from the dipole model which demonstrates

that we are imaging with DEP. We estimate the tip-sample force F_{TS} using Eq. (2.7) which is valid in amplitude modulation AFM when the dominant interactions are conservative and only have significant values at the point of closest approach, as they are here. Using $k = 39$ nN/nm, $A_0 = 162$ nm, $A_S = 88$ nm, and $Q = 534$, we find $F_{TS} = 2.9$ nN. The tip-sample force may be independently estimated with the dipole model by estimating DEP force on a dipole above a hexagonally close packed monolayer of 1 μm diameter silica beads resting on a silica substrate. We generate contours of constant force, as depicted in Figure 6.5(c), then compute a least-squares fit with the topographic contour across the peaks of beads shown as a dashed line in Figure 6.5(b). The line trace is shown as a black line in Figure 6.5(d) with the fit to the dipole model is shown as a red line. This is a one parameter fit which yields $F_{TS} = 2.1$ nN if we estimate the strength of the dipole as $p = 4 \times 10^{-22}$ Cm, which is the dipole moment predicted by Eq. (6.4) with $\lambda = 400$ nm. The good agreement between the predictions of the dipole model and experiment, as well as the symmetric appearance of the beads, indicates the the tip is indeed behaving as a dipole.

6.6 Coaxial AFM Tweezers

We demonstrate the 3D assembly of silica beads using a coaxial AFM probe. Figures 6.6(a) to 6.6(c) show the manipulation of sparse silica beads on polished silicon and Figures 6.6(d) to 6.6(f) show the manipulation of a close-packed monolayer of beads on roughened silicon, both in air. To locate a bead, the sample is first imaged in tapping mode, as shown in Figures 6.6(a) and 6.6(d). The triangular shape of the beads is due to the convolution of the triangular tip with the beads. To pick up a

bead, the tip is pressed into it with $V = 40$ V_{RMS} at 5 kHz. At this voltage, DEP together with the adhesion of the bead to the tip is strong enough to pick up the bead by overcoming its adhesion to the substrate. The force-distance curve shows that a bead was picked up. Once the bead has been picked up, the field is turned off, and the beads are imaged again as shown in Figures 6.6(b) and 6.6(e). The beads now appear round, because they are imaged by a fellow bead. The bead is deposited by pressing the tip into the desired location and scraping the bead off by moving it along the surface. This drop off technique is needed to overcome the adhesion between the bead and the coaxial probe surface. The change in AFM feedback shows that drop off has occurred. The substrate is again imaged as shown in Figures 6.6(c) and 6.6(f) to verify the final position of the bead.

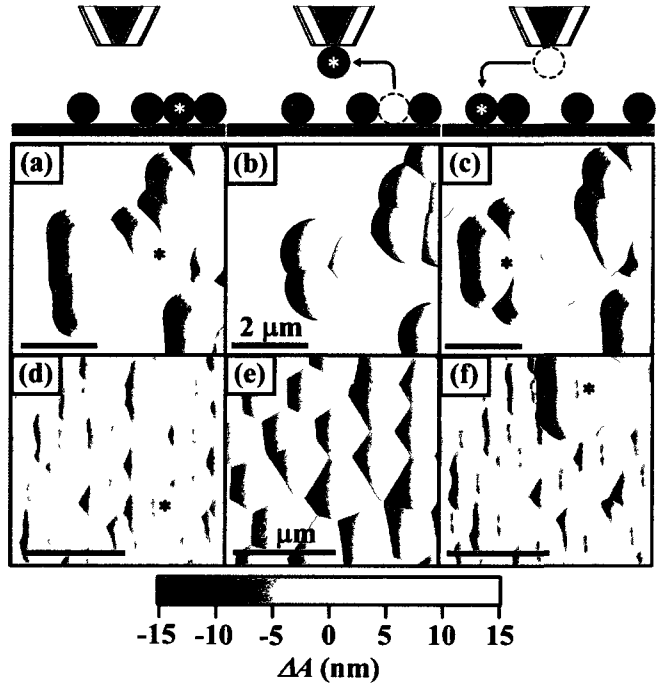

Figure 6.6: Tapping mode images taken by a coaxial probe showing the assembly of 1 μm diameter silica beads. The color scale corresponds to the change in oscillation amplitude A. (a) Sparse beads on a smooth silicon substrate. The bead marked with an asterisk is picked up by the coaxial probe. The marked bead is grabbed by the tip by pressing against it with $V = 40$ V_{RMS} applied to the tip. Dielectrophoresis holds the bead to the tip. Once retracted from the substrate, the field is turned off and adhesive forces are sufficient to hold the bead to the coaxial probe. (b) The same region is imaged again with the bead on the tip of the coaxial probe. (c) The bead is deposited in the location marked with an asterisk and the sample is imaged again with the coaxial tip. (d) A close-packed layer of beads on a roughened silicon substrate. The bead marked with an asterisk is picked up with the coaxial probe with DEP. (e) The same sample is imaged again with the bead on the tip. (f) The bead is deposited in the location marked with an asterisk and the sample is imaged again with the coaxial tip. This bead was deposited on top of an array of other bead demonstrating 3D assembly.[79]

6.7 Outlook

Imaging with DEP improves the utility of coaxial probes for topographic imaging by making the imaging mode non-contact and decreasing the effective tip radius. The non-contact nature of imaging with DEP mitigates the bluntness and asymmetry of the tip. If tip radius is defined as the half-width at half-max (HWHM) of a vanishingly small object ($a \rightarrow 0$), the tip radius is found to be HWHM $= 0.75L_p\left(2^{1/5}-1\right)^{1/2}$ or HWHM $\approx 0.3\lambda$. Thus imaging with DEP allows for $\approx 70\%$ improvement in tip radius.

A further advantage of imaging with DEP is that the local force is dependant on the dielectric properties of the sample and can be used to image variation in dielectric parameters. The force on a coaxial tip a distance z above a substrate is proportional to $\frac{(\epsilon_2-\epsilon_0)}{(\epsilon_2+\epsilon_0)}$, as seen in Eq. (6.6). The presence of the substrate dielectric constant ϵ_2 shows the dependance of the DEP force on the dielectric properties. The DEP imaging performed here was performed with an electric field at 5 kHz but in principle any frequency may be used and dielectric frequency specific dielectric imaging may be performed to provide a dielectric map of a substrate at many frequencies.

Conductive objects may also be imaged and manipulated with DEP. If an object is conducting or acted on by an AC field, it is appropriate to consider the complex permittivity as described in Section 2.4.2. Conductive objects have very high polarizabilities, making them optimal for imaging and manipulation with positive DEP.[45]

The ability to pick-and-place microscale objects has many potential applications in assembly and imaging. Biological cells are typically very polarizable and are commonly positioned with DEP. A coaxial probe could place them in specific locations

to perform tissue assembly or monitor cell-cell interactions. Further, if a particle of interest can be grabbed and held, it can be used to image a sample, as demonstrated in Figure 6.6. This technique could be used to image with functionalized particles and observe specific interactions. Two limitations of using coaxial probes and DEP are clustering, since the interaction is attractive everywhere, and irreversible stiction, as particles are held in contact. We have proposed and demonstrated triaxial probes that overcome these challenges for nanoscale particles and they are discussed in Chapter 7.

Chapter 7

Triaxial AFM Probes for Non-Contact Trapping and Manipulation

7.1 Introduction

An atomic force microscope (AFM) tip that can grab and release particles could have many applications in manipulation and imaging.[84, 24] In Chapter 6, we described coaxial AFM probes that can perform pick-and-place manipulation of microscale objects and image with a particle trapped on their tip. Coaxial probes use positive dielectrophoresis (pDEP) to trap objects more polarizable than the medium. Using pDEP has two major drawbacks: (1) The use of an long range attractive force can result in clustering of the desired particle, rather than grabbing a controllable number. (2) In the electrostatic regime, maxima of electric field necessarily are in

contact with electrodes so trapping while in contact is necessary. Trapping in contact makes pDEP methods at risk for irreversible stiction from van der Waals or other adhesion forces.[85]

In this chapter, we demonstrate triaxial AFM probes for non-contact trapping and manipulation with negative dielectrophoresis (nDEP). A schematic of a triaxial probe is shown in Figure 7.1, a core electrode is surrounded by an inner and an outer shell electrode. By applying a voltage to the inner shell electrode, a triaxial probe creates an electric field with a zero displaced from the tip which can be used for trapping an object with nDEP. We begin by presenting a theoretical model of a triaxial probe in which the trapping action is captured by a simple ring model of the electrodes. This simple model illuminates the limitations of triaxial probes and how trapping ability varies with different sized probes. Next, we describe triaxial probe fabrication and the experimental apparatus used to demonstrate trapping. We show non-contact trapping of a single nanoparticle with a triaxial probe. The motion of the nanoparticle in the trap is used to image the shape and strength of the trap, which we find to be in agreement with our model. By adjusting the voltages on the probe, we move a single nanoparticle relative to the probe. Finally, we discuss future applications of triaxial probes for 3D nanoassembly of quantum structures and multifunctional imaging.

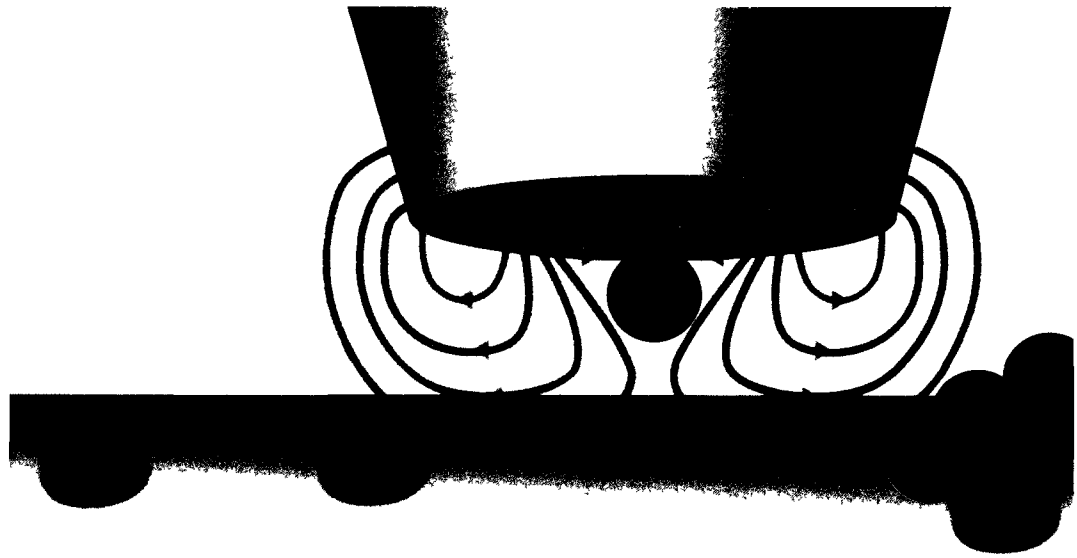

Figure 7.1: Illustration of a triaxial AFM probe performing assembly of a trapped nanoparticle suspended in water using negative dielectrophoresis (nDEP). The core electrode is a conducting AFM probe that has been coated with alternating insulating and conducting layers. Radio frequency voltages are applied to core and inner shell electrodes which generate an electric field indicated schematically by red field lines. The nanoparticle is trapped in the electric field zero displaced from the tip.[86]

7.2 nDEP Trapping with Triaxial Probes

Triaxial AFM probes can trap a single nanoparticle suspended in water using negative dielectrophoresis (nDEP). The triaxial probe is comprised of three independently contacted concentric electrodes constructed on an AFM probe as shown in Figure 7.2. The core electrode is held at voltage V_1, the inner shell electrode is held at V_2 and the outer shell electrode is grounded. The electrodes are separated by insulating layers of thickness λ. In order to demonstrate the utility of a triaxial probe for trapping nanoparticles, we simulate the electric field produced by a triaxial probe using 2D axisymmetric (Maxwell SV – Ansoft Corp.) and full 3D (Maxwell 11 – An-

soft Corp.) finite element electrostatic simulations. The geometry and composition used for simulations in this are shown in Figure 7.2.

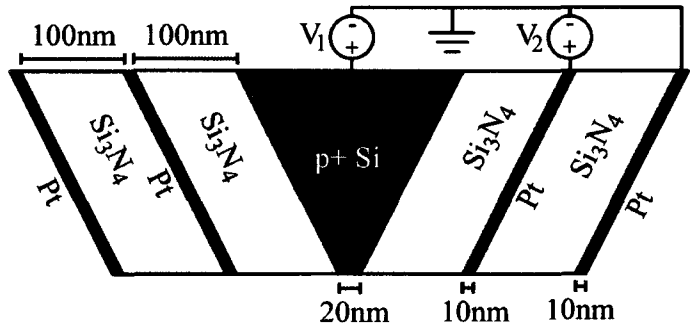

Figure 7.2: The triaxial AFM probe geometry used in electrostatic simulations. The core electrode is held at V_1, the inner shell electrode is held at V_2, and the outer shell electrode is grounded. The electrodes are separated by $\lambda = 100$ nm thick layers of silicon nitride.[87]

7.2.1 Electric field zero near the tip of a triaxial probe

Triaxial probes can use nDEP to trap nanoparticles much smaller than the tip radius without bringing them into contact with the surface of the tip. Figure 7.3(a) shows the magnitude of the electric field E calculated near the apex of a triaxial probe with $V_1 = 0$ V and $V_2 = 10$ V. There is a zero in the electric field displaced from the tip by $z_0 = 44$ nm. The right and bottom insets show the trapping energy calculated using Eq. (2.20) for a 5 nm radius silicon sphere along the z-axis at $r = 0$ (left) and along the r-axis at $z = z_0$ (bottom). The energy minima forms a trap that can hold a single nanoparticle in all three dimensions. The trap is weakest along the z-axis making that where a particle is most likely to escape. The maximum energy on this axis defines the trapping energy U_M located at $z = z_M$. The trapping energy

U_M for a 5 nm radius silicon sphere is greater than 10 k_BT at room temperature, indicating that it will be held against thermal fluctuations.

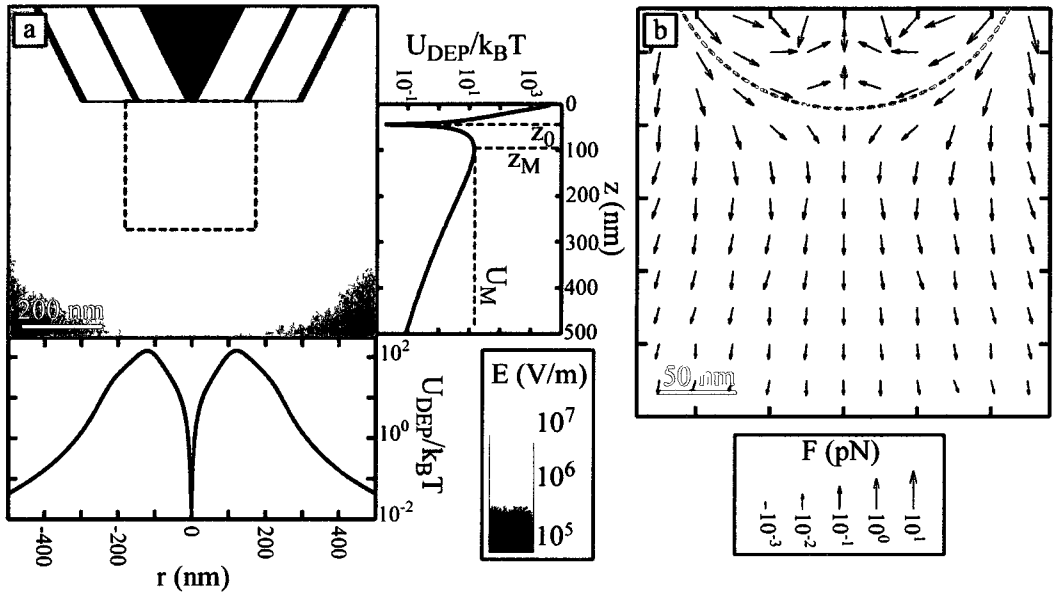

Figure 7.3: (a) The electric field amplitude E calculated by 2D simulation with $V_1 = 0$ and $V_2 = 10$ V. (right) The dielectrophoretic energy U_{DEP} of a 5 nm radius silicon sphere in water is calculated in units of k_BT at room temperature from Eq. (2.20) along z with $r = 0$. The minima of U_{DEP} at $z > 0$ is the location of the trap z_0. The maximum energy U_M beyond the trap ($z > z_0$) determines the strength of the trap. For a 5 nm radius silicon sphere U_M is greater than 10 k_BT. (bottom) Trapping energy U_{DEP} is calculated in units of thermal energy at room temperature as a function of r at $z = z_0$. (b) The DEP force $\boldsymbol{F}_{DEP}$ experienced by a 5 nm radius silicon sphere calculated from 3D simulation is vector plotted with the electric field magnitude E denoted by the color scale. The location of this plot corresponds to the dashed box in (a). The region inside by the blue dashed line represents the attractive region which pushes a particle into the nDEP trap while the region outside the dashed line is repulsive and pushes particles away from the triaxial probe.[87]

Triaxial probes hold a particle in an attractive region surrounded by a repulsive region in analogy to a hand grasping an object. The force $\boldsymbol{F}_{DEP}$ experienced by a 5 nm radius silicon sphere is plotted as a vector field superimposed on E, depicted as the colorscale in Figure 7.3(b). The blue dashed line separates the attractive trapping

region from the outer repulsive region. Inside the dashed line, $\boldsymbol{F_{DEP}}$ pushes particles toward the trap. Outside this region, $\boldsymbol{F_{DEP}}$ pushes particles away from the triaxial probe. The dashed line follows a ridge in the energy landscape with a saddle point located on the z-axis at z_M. The equivalence between forces and particle trajectories is due to Stokes' law in which the drag force is,[88]

$$\boldsymbol{F_{Drag}} = -6\pi\mu a\boldsymbol{v}, \tag{7.1}$$

where μ is the fluid viscosity. Therefore in low Reynolds numbers flows,[89] such as the flow around nanoparticles, $\boldsymbol{v} \propto \boldsymbol{F_{DEP}}$.

7.2.2 Moving the nDEP trap

The position and size of the nDEP trap can be tuned by adjusting the relative voltages on the core and inner shell electrodes as illustrated in Figure 7.4. When a voltage $V = 10$ V is applied to V_2, and $V_1 = 0$, the nDEP trap is close to the surface of the triaxial probe, as shown in Figure 7.4(a). If V_2 is held at $V_2 = V_1 + 10$ V while V_1 is made increasingly negative, the trap broadens and moves out into the medium as shown in the progression from Figure 7.4(a) to Figure 7.4(f). The trap is fully extended when $V_2 = 0$ and $V_1 = -10$ V. In this circumstance, the field profile, as shown in Figure 7.4(g), looks like the field of a coaxial probe. and the trap can be thought of as being infinitely far away. By adjusting V_1/V_2, the position of the trap can be controlled and positioned finely.

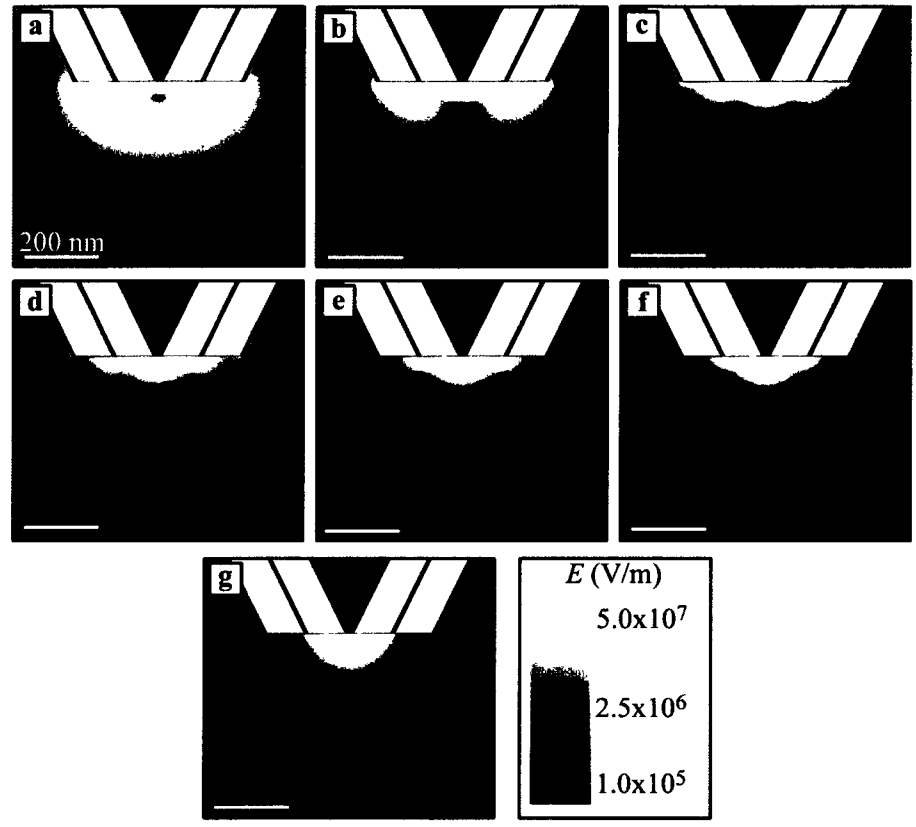

Figure 7.4: Electric field calculated by 2D simulation near the tip of a triaxial probe while varying V_2 and setting $V_1 = V_2 - 10$ V. (a) $V_2 = 10$ V, (b) $V_2 = 5$ V, (c) $V_2 = 2.9$ V, (d) $V_2 = 2$ V, (e) $V_2 = 1.5$ V, (f) $V_2 = 1.2$ V, and (g) $V_2 = 0$ V.[87]

7.2.3 Nanoassembly with a triaxial probe

A traixial probe acts analogously to a movable hand that can grasp and hold a single suspended particle, then release it at a desired location. The repulsive region around the trap combined with the ability to tune the size of the trap makes assembly with a triaxial probe analogous to a person grabbing a baseball out of a bag full of baseballs. The character of the trap is varied from attractive to repulsive by sweeping the ratio of applied voltages V_1/V_2.

An example of the assembly procedure is as follows

I. A topographic AFM scan is taken to locate the destination of the nanoparticle

II. The triaxial probe is made repulsive repulsive by setting $V_1 = -10$ V and $V_2 = 0$ V, as shown in Figure 7 4(g) The inner voltage V_1 is held at $V_1 = V_2 - 10$ V throughout the assembly procedure

III. The tip is moved into a liquid suspension of the desired nanoparticles

IV. A trap is formed by increasing V_2 which draws an electric field zero towards the triaxial probe, as shown in Figures 7 4(g) through 7 4(a) The repulsive region folds around the trap like a hand grabbing a baseball Matching the size of the triaxial probe to the size of the nanoparticle ensures that only one nanoparticle can be trapped at a time In the case of fluorescent particles such as semiconductor quantum dots, fluorescence microscopy can be used to determine if a particle is present

V. The triaxial probe is moved to the particle destination and V_2 is returned to 0 V The spatial profile of the field progresses from Figures 7 4(a) through 7 4(g) pushing the particle onto the surface where it is held with adhesive forces

Using this procedure, the particle can be deposited on a substrate while never touching the surface of the triaxial probe and risking being stuck to it by adhesive forces

7.2.4 Ring model of a triaxial probe

We have developed a simple model to analyze the ability of triaxial probes to trap nanoparticles The geometry of the triaxial probe can be approximated by three

simple electrodes: two concentric rings in the x-y plane centered around a disc at the origin, as shown in Figure 7.5(a). This approximation is most valid in the region close to the end of the tip where the conical probe has little effect. The radius of the inner ring is λ_e and the radius of the outer ring is $2\lambda_e$, where the effective radius of the ring λ_e is not required to be the same as the insulating layer thickness λ of the triaxial probe. We give the rings a circular cross section with radius δ and the disc a height δ for the purpose of assigning them capacitances, but we take $\delta \ll \lambda_e$ so the fields generated by the electrodes are well approximated by those of a point charge at the origin and rings of infinitesimal thickness. The charge on a given electrode can be given in terms of the voltages V_i and capacitance matrix elements C_{ij} where $i = 1$ or $j = 1$ corresponds to the center disc, 2 represents the middle ring, and 3 represents the outer ring. The charge q_i on the ith electrode is given by,

$$q_1 = C_{12}(V_1 - V_2) + C_{13}V_1, \tag{7.2a}$$

$$q_2 = -C_{12}(V_1 - V_2) + C_{23}V_2, \tag{7.2b}$$

$$q_3 = -C_{13}V_1 - C_{23}V_2. \tag{7.2c}$$

The model is simplified by defining two dimensionless parameters, $\kappa_1 = C_{12}/C_{23}$, $\kappa_2 = C_{13}/C_{23}$, a normalized distance $\xi = z/\lambda_e$, and the ratio of applied voltages $\eta = V_1/V_2$. The z-component of the electric field on the z-axis generated by these electrodes is,

$$E_z = \frac{C_{23}\Delta V}{4\pi\epsilon_0\lambda_e^2}\frac{1}{(1-\eta)}\left[\frac{\kappa_1(\eta-1)+\kappa_2\eta}{\xi^2} + \frac{(1-\kappa_1(\eta-1))\xi}{(\xi^2+1)^{3/2}} - \frac{(1+\kappa_2\eta)\xi}{(\xi^2+4)^{3/2}}\right], \tag{7.3}$$

where $\Delta V = V_2 - V_1$. The maximum ΔV possible without dielectric breakdown of water is $\Delta V = 10$ V for a triaxial probe with $\lambda = 100$ nm.[56]

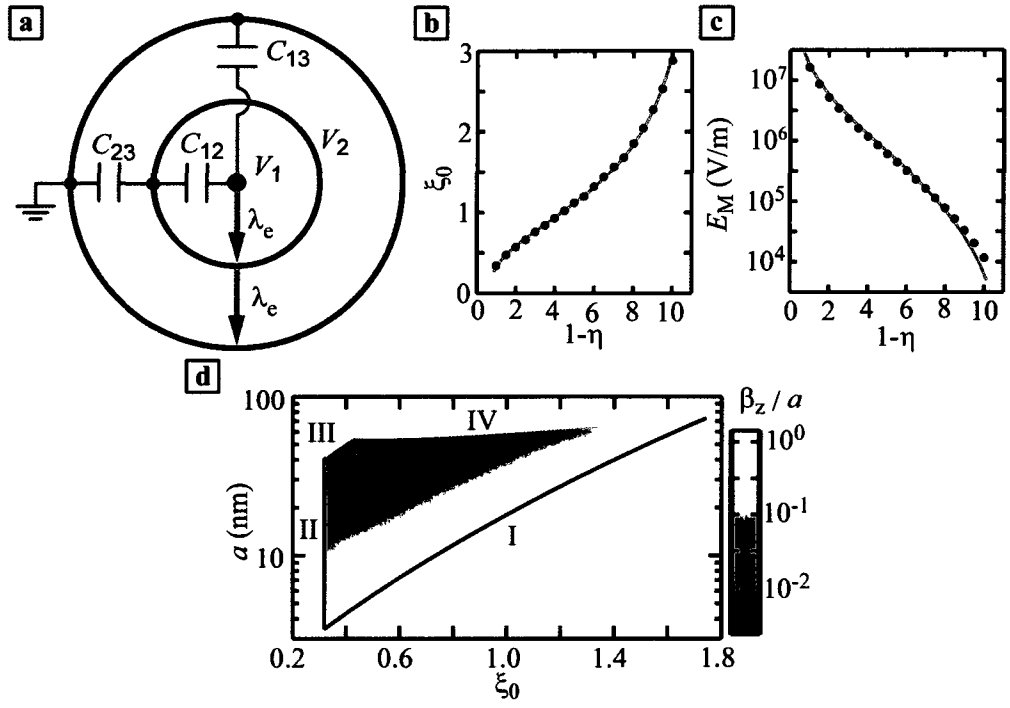

Figure 7.5: (a) Schematic of the ring electrode model of the a triaxial probe. The electrodes lie in the $x-y$ plane with the center electrode at the origin. (b) Normalized location $\xi_0 = z_0/\lambda_e$ along the axis of the electric field zero versus voltage ratio $1-\eta = (V_2 - V_1)/V_2$. The points correspond to results from finite element simulation while the line is the prediction of the ring model, fit to the points. (c) The trapping electric field E_M at z_M *vs.* $1-\eta$. The points are from the finite element simulation and the line is the prediction from the ring model, fit to the points. (d) Representation of the parameters for which a triaxial probe can trap a silicon nanoparticle with radius a held at ξ_0. The smallest silicon particle that can be held against thermal energy k_BT with the triaxial probe is $a = 2$ nm. The shading corresponds to the root mean square displacement β_z/a of the particle along the z-axis in the trap normalized by its radius which is calculated by linearizing E_z about z_0.[87]

The ring model predicts that the normalized electric field zero location $\xi_0 = z_0/R_e$ is determined only by the voltage ratio $\eta = V_1/V_2$. The voltage ratio η necessary to produce a given ξ_0 is found by setting Eq. (7.3) equal to zero which gives,

$$\eta = \frac{\kappa_1 - (\kappa_1 + 1)(1 + \xi_0^{-2})^{-3/2} + (1 + 4\xi_0^{-2})^{-3/2}}{\kappa_1 + \kappa_2 - \kappa_1(1 + \xi_0^{-2})^{-3/2} - \kappa_2(1 + 4\xi_0^{-2})^{-3/2}}. \tag{7.4}$$

This equation must be solved numerically for ξ_0, but the fact that neither V_1 nor V_2 enters the equation directly indicates that ξ_0 depends only on $\eta = V_1/V_2$ and not the absolute value of either voltage. To obtain the ring radius λ_e and relative values of the capacitance matrix elements C_{ij}, we fit the solutions of Eq. (7.4) to values of z_0 and $1-\eta$ obtained from finite element simulations of the electric field. Figure 7.5(b) shows excellent agreement in the fit between the analytic solution (curve) and the finite element simulation (points). The fit yields $\kappa_1 = 0.025 \pm 0.001$, $\kappa_2 = 0.063 \pm 0.001$ and $\lambda_e = 130 \pm 2$ nm for the tip geometry shown in figure 7.5(b) with $\lambda = 100$ nm.

The magnitude of the trapping electric field E_M that determines the energy barrier U_M of the trap is specified by the voltage ratio $\eta = V_1/V_2$ and the absolute value of the capacitiances. The location of this field maximum can be found analytically by finding where $\frac{\partial E_z}{\partial z} = 0$ for $z > z_0$. The derivative of the axial electric field is given by,

$$\frac{\partial E_z}{\partial z} = \frac{C_{23}\Delta V}{4\pi\epsilon_0\lambda_e^3}\frac{1}{(1-\eta)}\left[-\frac{2\kappa_1(\eta-1)+\kappa_2\eta}{\xi^3} - \frac{(1-\kappa_1(\eta-1))(2\xi^2-1)}{(\xi^2+1)^{5/2}} + \frac{(1+\kappa_2\eta)(2\xi^2-4)}{(\xi^2+4)^{5/2}}\right]. \tag{7.5}$$

The electric field maxima location $\xi_M = z_M/\lambda_e$ along the z-axis can be obtained by numerically solving $dE_z/dz = 0$. To obtain the absolute values of the capacitance matrix elements C_{ij}. we fit E_M from Eq. (7.3) to values of E_M and $1-\eta$ obtained from finite element simulations of the electric field. Figure 7.5(c) shows good agreement in the fit between the analytic solution from the ring model (curve) and the finite element simulation (points). The fit yields $C_{23} = 12.0 \pm 0.5$ aF and deviates at large values of $1-\eta$, because it is not possible to neglect the influence of the conical probe far away from the tip. The value of E_M can be used together with Eq. (2.20) to calculate the trapping energy U_M of a given particle.

7.2.5 Limits on trapping with a triaxial probe

Triaxial probes provides a powerful way to trap and assemble particles of a range of sizes. The region in which a triaxial probe can trap a silicon nanoparticle as a function of trap location ξ_0 and nanoparticle radius a is given by boundaries **I**, **II**, **III**, and **IV** shown in figure 7.5(d).

I. This boundary is determined by the condition that the trapping energy U_M be greater than thermal energy k_BT.

II. The minimum trap location ξ_0 is given by the breakdown voltage between the inner and outer shell electrodes.

III. The trapped particle radius a cannot be larger than z_0 without the particle coming into contact with the tip.

IV. The particle cannot be larger than the trap size. This is estimated by limiting the particle radius $a < z_M - z_0$.

This analysis predicts that silicon particles as small as $a = 2$ nm can be trapped with triaxial probes at room temperature. This model is most valid when $a \ll \lambda$ and therefore a is small compared to the physical size of the trap.

It is possible to trap particles with a triaxial probe such that their random fluctuations due to Brownian motion are smaller than their radius. We estimate how tightly particles are held by linearizing E_z about z_0 which gives U_{DEP} parabolic in z. This approximation defines a spring constant $k \propto (dE_z/dz)^2$ which can be used with

the equipartition theorem[90] to approximate the root mean displacement β_z in z as,

$$\beta_z = \left(\langle (z - z_0)^2 \rangle\right)^{1/2} = \left(\frac{-k_B T}{4\pi a^3 \epsilon_M K \left(dE_z/dz\right)^2}\right)^{1/2} \quad (7\ 6)$$

This number will be real because the Classius-Mosotti factor K is negative for nDEP The root mean square displacement β_z normalized by the particle radius is shown as the the color scale in Figure 7 5(d) All but the smallest particles that can be trapped have $\beta_z < a$

7.2.6 Scaling of triaxial probes

As Maxwell's equations have no built in length scale, it is useful to consider how the utility of a triaxial probe would change as probe is made larger or smaller The probe is characterized by the thickness of its insulating layer λ and the rest of the dimensions are taken to scale with λ The ring model helps elucidate the scaling as the capacitances C_{ij} and ring radius λ_e fully specify the electrostatics Dimensionally, we expect $\lambda_e \propto \lambda$ and $C_{ij} \propto \lambda$ and this is verified by simulation of triaxial probes with λ = 10 50, 100 1000 nm and subsequent fitting to $\eta(\xi_0)$ and $E_M(\eta)$, as described above The results of this fitting are shown in Figures 7 6(a) to 7 6(d) As expected, $\lambda_e = \lambda \times 1\ 55$, $C_{23} = \lambda \times 0\ 12$ aF/nm, and both κ_1 and κ_2 are found to be independent of λ The triaxial probes used in these simulations have a different aspect ratio from the one described previously, accounting for the difference in fitting parameters The maximum possible ΔV between two electrodes will also scale proportionally to λ as it is determined by the maximum electric field E_{BD} that avoids dielectric breakdown of the medium

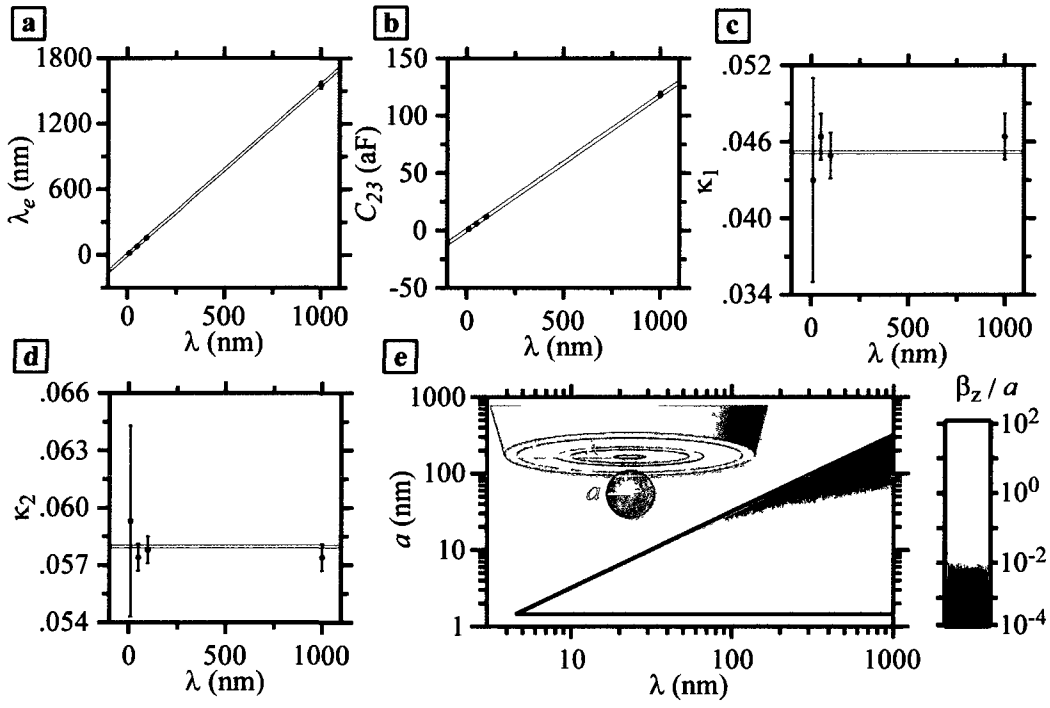

Figure 7.6: Scaling of the trapping ability of triaxial probes with size elucidated with the ring model. (a) The effective ring radius λ_e scales linearly with the insulating thickness λ of a triaxial probe. While the individual capacitances such as C_{23} vary with linearly λ (b), the ratios $\kappa_1 = C_{12}/C_{23}$ (c) and $\kappa_2 = C_{13}/C_{23}$ (d) are independent of λ. (e) The scaling of the ring model parameters with λ is used to predict the trapping limitations of triaxial probes of a given size. This estimate is for a nanoparticle of radius a experiencing nDEP ($\mathrm{Re}(K) = -0.5$) in water ($\epsilon_M = 80\epsilon_0$) with a maximum voltage $\Delta V/\lambda = 1$ MV/cm. All triaxial probes are limited in the lower limit of trapping to $a = 1.5$ nm by the breakdown field of water and in upper limit to $a = 0.32 \times \lambda$ to avoid the particle touching the probe. The color scale shows the ratio β_z/a which indicates how tightly a given particle is held. It is clear that smaller probes trap more tightly, demonstrating the advantage of size-matching the triaxial probe to the particle.

The scaling of the parameters of the ring model allow a comparison of the trapping ability of different size triaxial probes. Since κ_1 and κ_2 do not depend on λ, the normalized trap location ξ_0 given in Eq. (7.4) is independent of λ as well. The trapping capability of a triaxial probe is given by the maximum field $E_z(\xi_M)$ at the

location of the potential maximum U_M. The scaling of $E_z(\xi_M)$ is given by Eq. (7.3) and is found to be,

$$E_z(\xi_M) \propto \frac{C_{23}\Delta V}{4\pi\epsilon_0\lambda_e^2} \propto \frac{\lambda^2}{\lambda^2} = 1. \tag{7.7}$$

The maximum electric field is therefore constant with changing λ, therefore all triaxial probes have the same lower limit in trapped particle size, but smaller triaxial probes can do it at lower voltages. The stiffness of the trap is given by $\frac{\partial E_z}{\partial z}(\xi = \xi_0)$, the scaling of which is given by,

$$\frac{\partial E_z}{\partial z} \propto \frac{C_{23}\Delta V}{4\pi\epsilon_0\lambda_e^3} \propto \frac{\lambda^2}{\lambda^3} \propto \frac{1}{\lambda}. \tag{7.8}$$

This scaling indicates that smaller triaxial probes are able to hold a given particle tighter. The final scaling consideration of triaxial probes is the maximum size particle that can be trapped. If the particle is held at $\eta = 0$, the largest particle that can be held without touching the probe is $a = z_0 = \xi_0\lambda_e$.

The trapping capability of a triaxial probe with insulating thickness λ is shown in Figure 7.6(e). The enclosed region of the graph is the region in which trapping is possible and the color indicates the rms fluctuations β_z of a trapped particle along the z-axis normalized to particle radius a. The bottom boundary occurs when the particle is too small to be held with $U_M = k_BT$. The upper boundary is given by the particle being too large for the trap such that if the particle was at held in the trap it would be in contact with the triaxial probe $z_0 = a$. Smaller probes hold objects more tightly and require less voltage while larger probes can trap a greater range of particle sizes. This estimate is for a nanoparticle of radius a experiencing perfect nDEP ($\mathrm{Re}(K) = -0.5$) in water ($\epsilon_M = 80\epsilon_0$) with a maximum voltage $\Delta V/\lambda = 1$ MV/cm.

7.3 Experimental

7.3.1 Fabrication of triaxial probes

Triaxial AFM probes were fabricated on commercial, doped silicon, PtIr coated AFM probes (Arrow-NCPt – NanoAndMore USA) as described in Chapter 3. In brief, a batch of probes is chemically cleaned and mounted onto a metal carrier. A 60 nm layer of chrome is evaporated onto the top surface of the probes by thermal evaporation, followed by a a 2 μm trilayer of $SiN_x/SiO_2/ SiN_x$ deposited by plasma enhanced chemical vapor deposition (PECVD). A 100 nm Cr/Au/Cr trilayer forms the inner shell electrode followed by another 2 μm insulating trilayer. The outer shell is formed by 100 nm of Cr/Au deposited by thermal evaporation. The probes are then milled in a focused ion beam (FIB) to expose the triaxial electrodes at the tip as shown in Figure 7.7(a) and magnified in Figure 7.7(b).

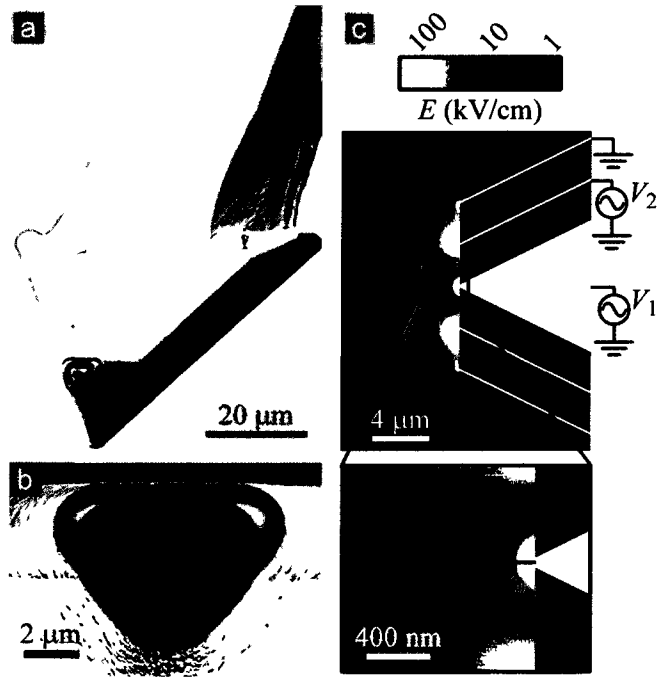

Figure 7.7: (a) Scanning electron micrograph of a triaxial probe and cantilever. (b) Magnification of the triaxial electrodes. The core electrode is visible as the triangle in the center and the inner and outer shell electrodes are visible as thin lines. (c) Finite element electric field simulation of the field at the tip of a triaxial probe with $V_1 = 0$ V and $V_2 = 10$ V. The electric field is strongly peaked at the tip and a minima in field is visible displaced from the tip. The inset shows a magnification of the field minimum, which is a distance z_0. This corresponds to a zero in the electric field where the electric field changes sign and we will use this zero to trap particles with nDEP.

7.3.2 Fluid cell and micropositioner

The experimental apparatus used to measured the trapping action of triaxial probes is shown in Figure 7.8. The triaxial probe is silver painted onto a printed circuit board (PCB) probe holder, and electrical contacts are made through wire bonds as shown in Figure 7.8(a) The probe tip is maneuvered by a micropositioner within 20 μm of the bottom of a fluid cell to allow observation by the inverted optical

microscope objective as shown schematically in Figure 7.8(b). The PCB is attached to a mounting arm as shown in Figure 7.8(c) which connects to a three axis micropositioner (injectMan – Eppindorf). The AFM cantilever is lowered into the fluid in open top fluid cell formed by a glass coverslip with a rubber gasket (Press-To-SealTM – Invitrogen). The fluid cell is placed on an inverted fluorescence microscope (DMIR13 – Leica) and observed by a sensitive camera (iXon X3 897 – Andor Technology plc.) through a 100× oil immersion objective with 1.5× barrel magnification.

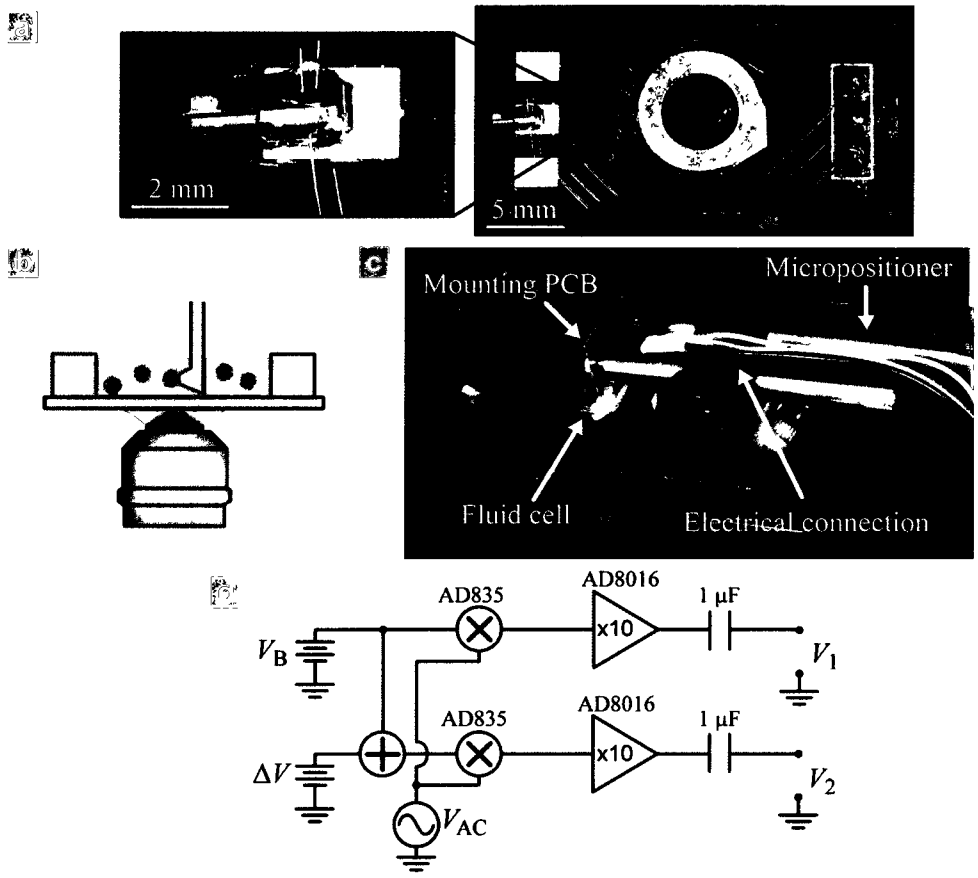

Figure 7.8: (a) Photograph of a triaxial probe mounded on a printed circuit board and electrically connect *via* wire bonds. (inset) Magnification of the probe showing the patterning of the films to allow separate connection to the inner and outer shell electrodes. (b) Schematic of the triaxial probe immersed in solution above an optical microscope. (c) Photograph of the triaxial manipulation assembly. The probe holder is attached to the end of a mounting arm connecting to a micropositioner (out of frame to the right). The probe is immersed in the fluid cell which is illuminated by blue light for fluorescence excitation. (d) Custom electronics created for driving the triaxial probe. This apparatus can drive a capacitive load with ~22 V up to ~20 MHz.

Operation of the triaxial probe was observed by manipulating fluorescent polystyrene beads. A 100 μL quantity of 1% by volume polystyrene beads (G200 or G900 Fluoro-MaxTM – Thermo Scientific) loaded with green dye are suspended in 500 mL 1:1

deionized (DI) water:Glycerol by volume. The glycerol increases the dynamic viscosity μ from $\mu = 1$ cP to $\mu = 8$ cP making the motion of beads easier to visualize.[91] A low conducitivity medium is necessarily to mitigate electrokinetic effects such as AC-electroosmosis and Joule heating as discussed in Section 2.5.2.[45]

7.3.3 Dielectric properties of the system

Tabulated dielectric properties can be used to predicted the DEP behavior of the system. The dielectric constant and viscosity of a 1:1 by volume mixtures of water and glycerol is $\epsilon_M = 63\epsilon_0$[92] and $\mu = 8$ cP[91]. The conductivity σ_M is determined largely by the quantity of dissolved ions in the water. We begin with millipore deionized water ($\sigma_M \sim 0.1$ μS/cm). Small quantities of ions may be introduced by the stock bead suspension, but the final conductivity is measured to be $\sigma_M < 1$ μS/cm. Polystyrene beads are not as well characterized in the literature; their permittivity is consistently $\epsilon_P = 2.6\epsilon_0$[93], but the surface conductance G_S depends on details of the media and bead preparation. For particles with radius $a = 100$ nm, estimates vary from $G_S \sim 0.2$ nS[93] to $G_S \sim 1$ nS[51]. From the measured crossover frequency $f_C \sim 800$ kHz, calculated in Eq. (2.23), we estimate $G_S \approx 0.2$ nS.

7.3.4 Electronics

Custom electronics, shown in Figure 7.8(d), are required to drive the capacitive load presented by a triaxial probe. Electrical connection to the triaxial probe enters *via* the cable visible in Figure 7.8(c). The voltages V_1 and V_2 are measured at the contact pads of the triaxial probe holder by an oscilloscope. The radio frequency (RF)

voltage V_{AC} is generated by a function generator (33250A – Agilent Technologies). Two additional function generators (33220A – Agilent Technologies) drive the bias voltage V_B and throttle voltage ΔV. These voltages are fed into two analog multiplier chips (AD835 – Analog Devices) that create the products $V_{AC} \times V_B$ and $V_{AC} \times [V_B + \Delta V]$ which are fed into a line driver (AD8016 – Analog Devices) to provide a 10× gain and drive the capacitive load. The final voltages are passed through a 1 μF blocking capacitor to remove any DC offset. The drive circuitry is limited to 22 V peak-to-peak excitations and to $\sim$ 20 MHz frequencies by the final amplifier. Following the analysis of Section 2.3, the excitation is also limited by attenuation due to the RC network formed by the triaxial probes. For the probe described here, $C \sim 100$ pF and $R \sim 10\ \Omega$ which will attenuate voltages applied at $f > 160$ MHz.

7.4 Results

In this Section, we experimentally demonstrate trapping and manipulation of nanoparticles with triaxial probes. In Section 7.4.1 we show that a combination of pDEP and nDEP can be used to draw particles toward the triaxial probe, and hold them in the nDEP trap. Next, in Section 7.4.2 we measure the DEP-induced particle speed and find it to be in agreement with our theoretical predicts. In Section 7.4.3, we characterize the size and shape of the trap and find it to be in agreement with our model for this system. Finally, in Section 7.4.4 we show that we can position a single nanoparticle relative to the probe by changing the ratio of applied voltages.

7.4.1 Trapping with a triaxial probe using pDEP and nDEP

Figure 7.9 illustrates how polystyrene beads are drawn toward, and trapped by, the triaxial probe. The probe is held in a suspension of fluorescent polystyrene beads with radius $a = 100$ nm. The beads are surrounded by a layer of ions that form a screening layer at the surface of the bead giving rise to a surface conductance G_S. As discussed in Section 2.4.2, the surface conductance of these beads makes them more polarizable than the medium at frequencies below a characteristic crossover frequency f_C. Their behavior changes from pDEP to nDEP as the RF frequency is increased above $f_C = 800$ kHz. An attractive field profile (Figure 7.9(a)) is created by applying a low frequency RF voltage $V_2 = \Delta V \sin(2\pi f t)$ to the inner shell, with $\Delta V = 10$ V, $f = 100$ kHz, and $V_1 = 0$ V. The sequence of images shown in Figures 7.9(b) to 7.9(f), taken at 200 ms intervals, shows how particles are attracted toward the high field region of the triaxial tip - the bead marked by an arrow moves towards the probe, and becomes trapped on its surface in Figure 7.9(f).

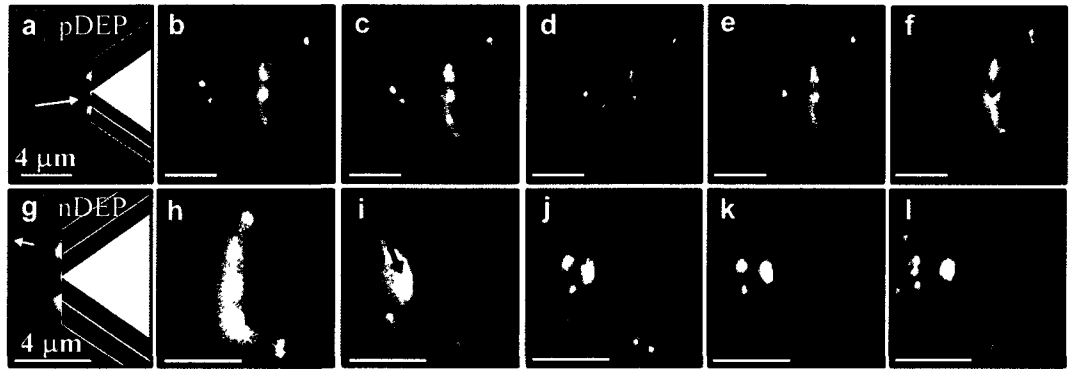

Figure 7.9: (a) Schematic showing particles being attracted to field maxima near the triaxial probe with pDEP. (b) An optical micrograph shows polystyrene beads approaching the triaxial probe; the approximate location of the triaxial probe is shown as an overlay. The bead marked with the red arrow moves towards the probes in subsequent frames (c) through (e), and becomes attached to the probe in (f). All frames are separated by 200 ms. (g) Schematic showing particles being repelled from field maxima near the triaxial probe with nDEP, the particle on top is repelled back into suspension while the bottom particle is held in the nDEP trap. (h) Polystyrene beads are held against a triaxial probe with pDEP. (i) The RF frequency is raised from 100 kHz to 5 Mhz and the interaction becomes nDEP, jettisoning the beads from the triaxial probe. (j) through (l) The majority of the beads are pushed away from the triaxial probe into suspension while those marked with the red arrow are held in the nDEP trap.

By increasing the RF frequency to $f = 5$ MHz, we turn on the nDEP trap above the triaxial probe and contain polystyrene beads like a hand closing. The polystyrene beads are now repelled from high field regions - some are drawn into the nDEP trap and the rest are pushed out into the medium, as shown in Figure 7.9(g). Before f is increased (Figure 7.9(h)), many beads are near the probe surface. Just after the frequency is increased (Figure 7.9(i)), the beads on the probe are jettisoned into suspension. In the subsequent frames (Figures 7.9(j)-7.9(l)), the majority of the beads are pushed away from the probe, while those marked with the red arrow are pulled to the electric field zero that forms the nDEP trap.

7.4.2 Estimation of the speed of DEP

The DEP-induced motion of the polystyrene beads is in agreement with our model of their dielectric properties. The speed of a spherical particle experiencing DEP can be estimated by equating the time averaged DEP force Eq. (2.22) with viscous drag from Eq. (7.1) to find,[45]

$$\boldsymbol{v}_{DEP} = \frac{\epsilon_M a^2 \,\mathrm{Re}(K) \boldsymbol{\nabla} E^2}{6\mu}, \tag{7.9}$$

where K is the frequency dependent Classius Mosotti factor given in Eq. (2.21). A typical experimental electric field gradient in the region just beyond the nDEP trap is $|\boldsymbol{\nabla} E^2| \approx 10^{-2} V^2/\lambda^3$ where V is the applied voltage, λ is the electrode separation of the triaxial probe, and the numerical prefactor is found with the numerical simulation in Figure 7.11(c). Inserting these expressions into Eq. (7.9) we find,

$$v_{DEP} \approx \frac{\epsilon_M 10^{-2} a^2 V^2}{6\mu\lambda^3} \,\mathrm{Re}(K). \tag{7.10}$$

For the triaxial probe and system here, $\lambda = 1.6$ μm, $V = 7.5$ V, $a = 100$ nm, $\epsilon_M = 63\epsilon_0$, and $\mu = 8$ cP. For these conditions, $v_{DEP} \approx 16$ μm/s should be expected.

The measured speeds v_{DEP} of individual polystyrene beads as they approach the triaxial probe *vs.* frequency f are shown as points in Figure 7.10. The red curve is a one parameter fit to the theoretical prediction,

$$v_{DEP} = v_0 \,\mathrm{Re}(K), \tag{7.11}$$

to find $v_0 = 6.5$ μm/s. The results of this fitting indicates that the particles are moving $\sim$ 40% as fast as expected, corresponding to an electric field $\sim$ 60% the expected magnitude at the tip due to the applied voltage being attenuated. The

predicted crossover frequency $f_C \sim 800$ kHz is clearly evident in Figure 7.10. For $f < f_C$, the beads undergo pDEP and move towards the probe and for $f > f_C$, the beads undergo nDEP and are repelled from the tip. This behavior is consistent with the expected behavior predicted by Eq. (7.10).

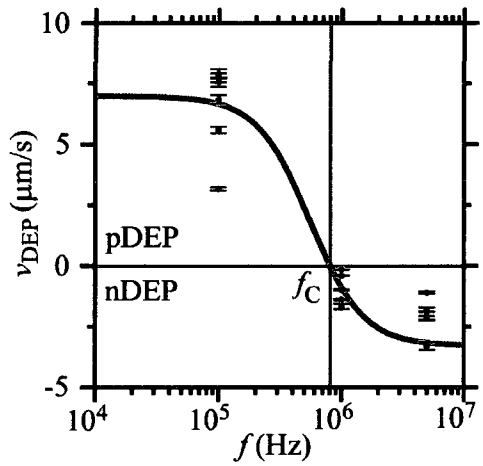

Figure 7.10: Measured speed v_{DEP} of 100 nm radius polystyrene beads *vs.* frequency f of the driving electric field. Each point represents the average speed of a bead moving near the triaxial probe, and the error bars include the error in localizing the beads and the statistical error in finding the speed *via* linear regression. At frequencies $f < f_C$, the beads are attracted to the probe with pDEP, while for $f > f_C$ beads are repelled from regions of high electric field. The red curve is a one parameter fit to the theoretically predicted relationship v_{DEP} *vs.* f given in Eq. (7.11) with $v_0 = 6.5$ μm/s.

7.4.3 Size and shape of nDEP trap

The electric field zero created by the triaxial probe used in this experiment can trap nanoparticles tightly against thermal motion. The electric field profile E is shown in Figures 7.11(b) and 7.11(c). The probe geometry is chosen to represent the triaxial probes used in this study and is shown in Figure 7.11(a). Figure 7.11(b) shows the electric field magnitude E along the z-axis with $V_1 = 0$ and $V_2 = 7.5$ V. A zero in the

electric field is located at $z = z_0$ which will trap a particle with nDEP. The simulation shows a finite field minimum at z_0 due to meshing, but a true zero exists as the field changes sign as it passes across z_0. The magnitude of the electric field E in the r-axis at $z = z_0$ also increases away from the on-axis zero, as shown in Figure 7.11(c), so the particle will be held in the r-direction as well. The weakest part of the trap is along the z-axis at $z > z_0$ where the field reaches a maximum $E_M \sim 6$ kV/cm, which will trap nanoparticles with energy greater than $\sim 80 k_B T$ where k_B is Boltzmann's constant and temperature $T = 300$ K at room temperature.

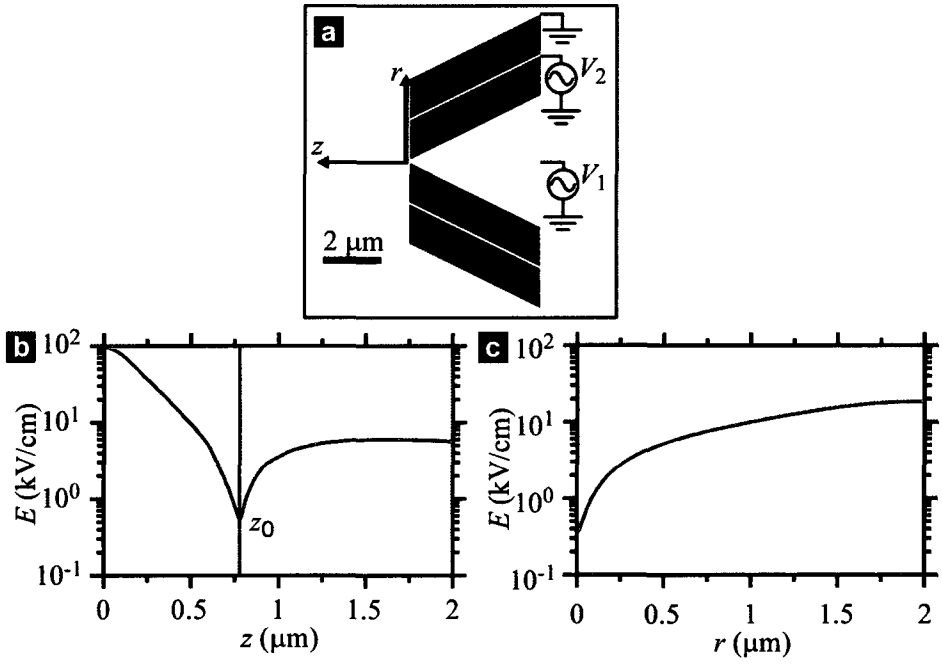

Figure 7.11: (a) Schematic diagram of the model of the triaxial probe used for axisymmetric electrostatic simulation (Maxwell 2D – Asnsys). (b) Simulated magnitude of the electric field E along the z-axis with $V_1 = 0$ V and $V_2 = 7.5$ V. A zero in the electric field amplitude is present at $z = z_0$, creating a trap that will contain an object with nDEP. The presence of the zero is guaranteed as E changes sign as it passes through z_0. (c) Simulated electric field magnitude E along the r-axis at $z = z_0$. The magnitude of the electric field increases in all directions to form an nDEP trap in three dimensions.

The motion of the particle about the nDEP can be used to image the size and shape of the trap. The root-mean-square (rms) displacement of particles due to thermal motion inside the nDEP trap created by linearizing E about $z = z_0$ as shown in Eq. (7.6). Unlike the previous analysis, this field is taken to be oscillatory; averaging E^2 introduces a factor of $\frac{1}{\sqrt{2}}$. The rms displacements about $z = z_0$ in the z and r directions are then,

$$\beta_z = \left(\langle (z - z_0)^2 \rangle\right)^{1/2} = \left(\frac{-k_B T}{2\pi a^3 \epsilon_M K \left(dE_z/dz\right)^2}\right)^{1/2} \tag{7.12}$$

and

$$\beta_r = \left(\langle r^2 \rangle\right)^{1/2} = \left(\frac{-k_B T}{2\pi a^3 \epsilon_M K \left(dE_z/dr\right)^2}\right)^{1/2}. \tag{7.13}$$

At $z = z_0$, $\frac{\partial E}{\partial z} = 1.4$ V/μm^2 and $\frac{\partial E}{\partial r} = 0.9$ V/μm^2, calculated with a finite difference method from the electrostatic simulation shown in Figures 7.11(b) and 7.11(c). For a polystyrene bead with $a = 100$ nm driven with an electric field at $f = 1$ MHz, we calculate $\beta_z = 66$ nm and $\beta_r = 103$ nm.

Figure 7.12 shows the triaxial probe holding a polystyrene bead in the nDEP trap within a region comparable to the size of the bead. Figure 7.12(a) shows a sequence of images that depict the motion of a bead (red) trapped above the triaxial probe, and a bead (blue) adhered to the probe surface. The distribution of trapped and adhered particle positions (Figure 7.12(b)) over time is found by fitting two-dimensional Gaussians to each optical image in the sequence. The position of the trapped particle relative to the probe (Figure 7.12(c)), is found by comparing the positions of the trapped and adhered bead in each image. Principle component analysis is used to find the tight (x') and loose (y') axes of the particle distribution over time. The strength of the nDEP trap is described by histograms of the displacements along the

x' and y' axes, shown in Figures 7.12(d) and 7.12(e). The spatial distributions are fit very well by Gaussians, appropriate for thermal fluctuations in a quadratic potential with a linear restoring force.[90] The measured rms displacements $\beta_{x'} = 133$ nm and $\beta_{y'} = 204$ nm are comparable to the 100 nm radius of the particle.

The measured shape and strength of the nDEP trap are in agreement with those predicted by theoretical simulations. Thermal fluctuations of the bead's position can be estimated from the triaxial probe geometry, the dielectric properties of the system, and our theoretical model for triaxial probes. For the triaxial tip shown in Figure 7.11(a), this analysis predicts rms displacements $\beta_z = 66$ nm and $\beta_r = 102$ nm in the axial and radial directions respectively, comparable to our observations. The experimental rms displacements and the observed DEP velocities from Section 7.4.2 are both consistent with the values of V_1 and V_2 being attenuated to $\sim 50\%$ of the applied values. The ratio of the experimental rms displacements $\frac{\sigma_{x'}}{\sigma_{y'}} = 0.65$ is in excellent agreement with the theoretically determined ratio $\frac{\sigma_z}{\sigma_r} = 0.64$, indicating that the shape of the trap matches our theoretical predictions.

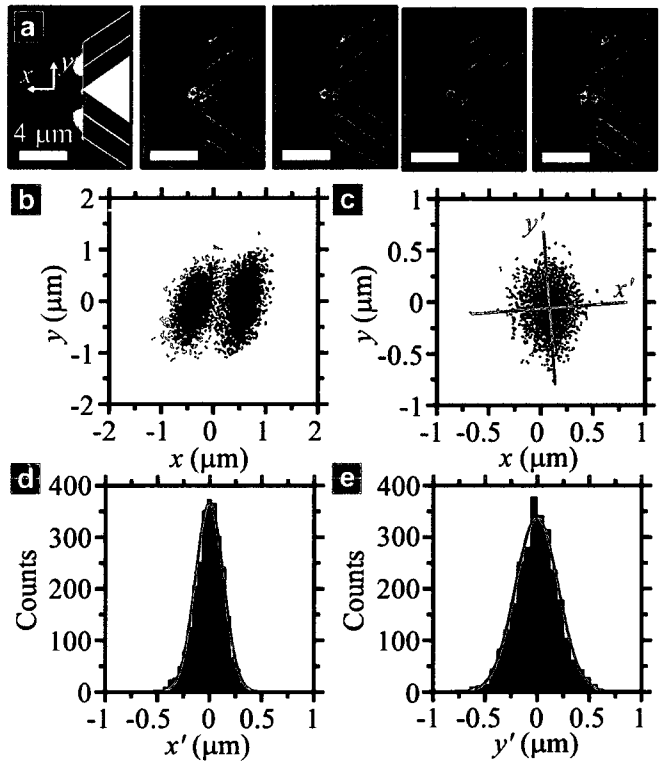

Figure 7.12: (a) Schematic and four representative fluorescence images of a 100 nm radius bead trapped in the nDEP trap. The bead identified with the red dot is held in the nDEP trap while the bead identified with a blue dot is adhered to the tip. A schematic of the tip is superimposed in the approximate location of the tip as a guide to the eye. A 15 V peak-to-peak excitation at 1 MHz is applied to V_2 while $V_1 = 0$. These images are taken from a data set of 5000 images used for the analysis. (b) Scatter plots of the position of the bead in the trap (red dots) and the tip inferred from the position of an attached bead (blue dots). (c) Scatter plot of the separation between the trapped bead and the triaxial tip given by the separation of trapped bead/adhered bead pairs. The axes of tightest and loosest trapping are determined with principle component analysis and are shown on the plot as the x'-axis and y'-axis respectively. (d) Histogram of the spread of the trapped bead about the x'-axis. A Gaussian fits the data very well and produces a width of $\beta_{x'} = 133$ nm. (e) Histogram of the spread of the trapped bead about the y'-axis. A Gaussian fits the data very well and produces a width of $\beta_{y'} = 204$ nm.

7.4.4 Controlling the position of the nDEP trap location

The location of the nDEP trap formed by a triaxial probe can be estimated from the electrostatic field pattern created by the ring model described in Section 7.2.4 and shown in Figure 7.5(a). The position of the nDEP trap in the ring model is parameterized only by the ring radius λ_e and two ratios of capacitances $\kappa_1 = \frac{C_{12}}{C_{23}}$ and $\kappa_2 = \frac{C_{13}}{C_{23}}$. Using the parameters we have previously determined, $\lambda_e = 1.3R$, $\kappa_1 = 0.025$, and $\kappa_2 = 0.063$, we may deduce the trap location for any applied voltages V_1 and V_2. In particular, we find that if we assign $V_1 = V_B$ and $V_2 = V_B + \Delta V$ where ΔV is a throttle voltage that determines how strong the trapping is, the bias voltage V_B determines where the trap is located. The trap location $\xi_0 = z_0/\lambda_e$ normalized to λ_e, is given in Figure7.13. The trap moves monotonically with V_B along the z-axis and especially well behaved and linear in the range $-0.5\Delta V < V_B < 0.5\Delta V$ with a slope $\sim \frac{\lambda_e}{\Delta V}$. As V_B approaches $-\Delta V$ the trap is moved infinitely far away and the trap opens, releasing the nanoparticle. For the probe presented here with $\Delta V = 7.5$ V, $\lambda \sim 1.6$ μm, and therefore $\lambda_e \sim 2$ μm, we expect the slope to be $\frac{\lambda}{\Delta V} \sim -300$ nm/V.

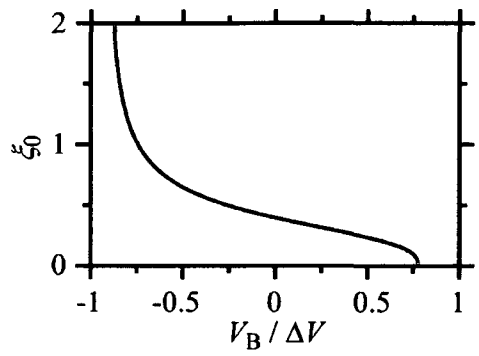

Figure 7.13: The normalized position $\xi_0 = z_0/\lambda_e$ of the nDEP trap along the z-axis *vs.* control voltage V_B is calculated from the ring model with $V_1 = V_B$ and $V_2 = V_B + \Delta V$. The curve shows that ξ_0 is a monotonic function of V_B, and that $z_0(V_B)$ is approximately linear in the range $-0.5\Delta V < V_B < 0.5\Delta V$. The zero disappears for V_B approaching $-\Delta V$, and the nDEP trap ceases to exist, like a hand opening.

Figure 7.14 demonstrates that we can precisely control the height z_0 of the trap above the probe surface, by changing the relative voltages on the core and shell electrodes. By setting $V_1 = V_B \sin(2\pi ft)$ and $V_2 = [V_B + \Delta V]\sin(2\pi ft)$ we make z_0 a monotonic function of the bias voltage V_B, as shown in Figure 7.13. The trapping power is controlled by the throttle voltage $\Delta V = 7.5$ V. Figures 7.14(a) and 7.14(b) show a single 460 nm radius fluorescent polystyrene bead trapped with $V_B = 0$ V and $V_B = -0.5\Delta V$ respectively. The positions of a bead trapped in the nDEP trap (red X) and a bead adhered to the back of the probe (blue X) are found by fitting two-dimensional Gaussians to the fluorescence intensity. The movement of the trapped bead relative to the probe is found for each pair of beads. As V_B is swept from 0 V in Figure 7.14(a) to $-0.5\Delta V$ in Figure 7.14(b), the bead moves away from the tip. By driving V_B with a 2 Hz sine wave, the periodic motion of the bead may be tracked, as seen in Figure 7.14(c). The height z_0 of the trap center relative to the

tip (Figure 7 14(d)), is a smooth and monotonic function of V_B, allowing the user to precisely control the height of a trapped bead above the triaxial probe surface By changing V_B from 0 V to $-0\ 5\Delta V$, the bead is moved $\approx 1\ \mu$m A straight line (red) fits the trap motion well with a slope of -270 nm/V The residual (Figure 7 14(e)), fit by a Gaussian, gives an rms deviation in trap height of 54 nm about the average value

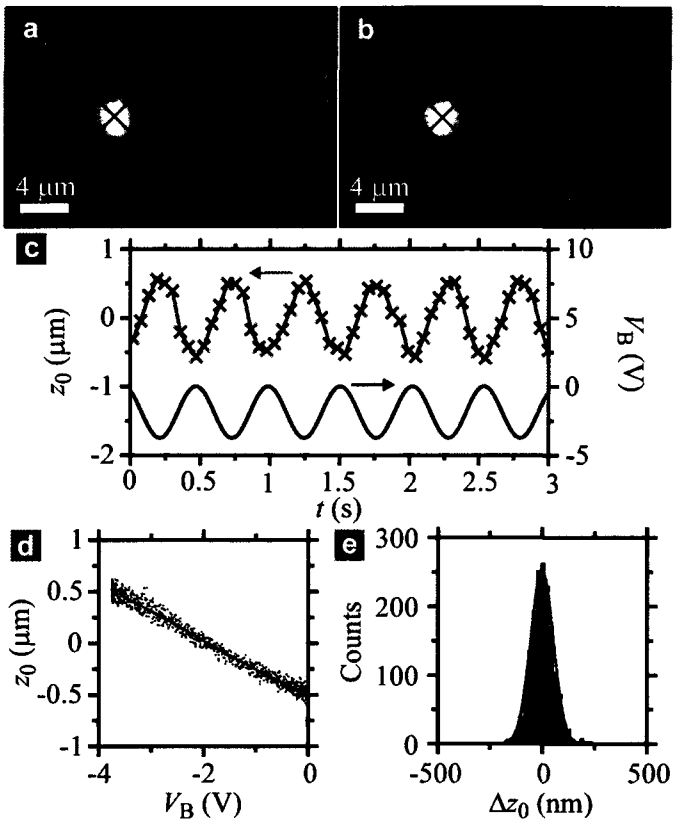

Figure 7.14: (a) Fluorescence image of a 460 nm radius polystyrene bead held in the nDEP trap (red X). A bead adhered to the back of the probe (blue X) is used as a reference to localize the tip. A 15 V peak-to-peak excitation at 5 MHz is applied to V_2 while $V_1 = 0$. (b) Now the bead is held further from the tip as 7.5 V peak-to-peak excitation at 5 MHz is applied to V_2 while the same excitation is applied 180° out of phase to V_1. (c) A control voltage V_B is used to move the nDEP trap location smoothly. The position z_0 of the trap relative to the probe *vs.* time t is determined by the distance between the trapped bead and the reference bead (d) The position of the trap is a monotonic function of V_B and we are able to move the bead ≈ 1 μm relative to the probe. The data is well fit by a line, shown in red. (e) Histogram of the spread of the trapped bead about the linear fit. A Gaussian fits the data very well and produces a standard deviation of 54 nm.

7.5 Discussion and Outlook

We have demonstrated triaxial AFM probes, a novel nanoassembly tool capable of grabbing, holding, and releasing nanoscale components suspended in liquid, as shown in Figure 7.15. Triaxial probes were nanofabricated on commercial AFM probes and we demonstrate trapping polystyrene beads in solution. By using a combination of pDEP and nDEP we draw beads towards the triaxial probe and hold them in an electric field zero displaced from the tip. We hold a 100 nm radius polystyrene bead in a region commensurate with its size and in agreement with our theoretical model for these probes. We are able to move the trapped bead relative to the tip by adjusting the voltages on the triaxial probe; we move a single polystyrene bead a range of ≈ 1 μm relative to the tip.

Our theoretical model of triaxial probes allows us to predict the limitations of triaxial probes and how they can be improved. The only limitation to how small of an object can be trapped is given by the dielectric breakdown field of the medium, which for water predicts that particles as small as 2 nm can be trapped. Smaller probes can trap a given particle more tightly and require less voltage to do so, but ideal trapping occurs when the trap is size-matched to the particle, in analogy to a nanoscale hand.

7.5.1 Integration with an atomic force microscope

The next step in making triaxial probes a viable instrument for nanotechnology is integration with an atomic force microscope. The addition of the AFM infrastructure would allow force-sensing and nanometer scale positioning, both prerequisites for

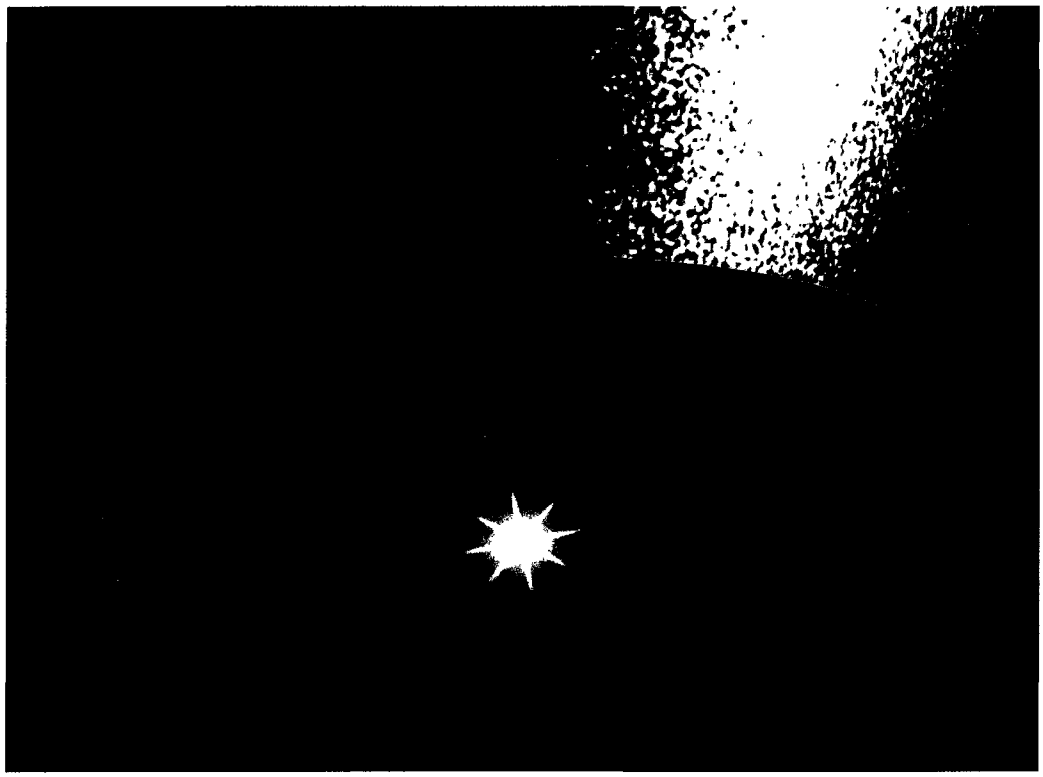

Figure 7.15: Artist's rendition of a triaxial AFM probe holding a single fluorescent nanoparticle.

assembly and imaging with triaxial probes. Since the probes are currently fabricated on commercial AFM probes, no change in the fabrication processes is necessary to enable this switch. Further, the distribution of contacts on the top surface of the AFM chips make them particularly well suited for connection to a commercial tip holder with multiple leads on top such as the iDrive from Asylum Research. Contact to the core conductor can be made from the bottom of the chip as is currently done.

Triaxial probes with thinner insulating layers would enable assembly and manipulation of single nanometer-scale particles. The probes demonstrated here had insulating thickness $\lambda \approx 1.6$ μm; their thickness was chosen to be large enough to observe particle trapping with an optical microscope. We have developed the fab-

rication techniques to create probes as small as $\lambda \approx 30$ nm, as demonstrated in Chapter 3. Smaller probes are simpler to operate as they require smaller voltages and hold objects more tightly by virtue of their size.

7.5.2 Assembly of nanoscale systems

Triaxial AFM probes have strong promise for nanoassembly as they combine the precision and versatility of AFM with the ability to grab and release single nanoparticles. Manipulation with nDEP is powerful because most dielectrics are less polarizable than water and while surface conductance can increase the polarizability of nanoparticles, operating at frequencies above their crossover frequency circumvent this. Operating in liquid is also beneficial as capillary forces are the dominant adhesive force, as described in Section 2.5.1.

Triaxial probes enable nanoassembly of single quantum emitters such as quantum dots[94] or diamond nanoparticles with NV-centers.[20] Semiconductor quantum dots are ideal candidates for manipulation with triaixal AFM probes because their diameter is typically 1 to 10 nm and their dielectric constant $\epsilon_P \sim 10\epsilon_0$ is much less than that of water $\epsilon_M \sim 80\epsilon_0$. Quantum dots may be selected based on characteristics such as photoluminescence spectrum, then positioned on pre-fabricated nanostructures to create complex interacting electronic and photonic systems.[95, 20] Nano-scale alignment with the substrate is afforded by the AFM and single-particle trapping and holding is granted by the triaxial probe.

This technique is also well suited for manipulation of small biological molecules such as proteins, macromolecular complexes such as ribosomes, or DNA.[96] By se-

lecting a frequency above the β relaxation of the protein, typically $1 - 10$ MHz, the protein is no longer able to rotate with the applied field and will have a dielectric constant smaller than that of water[97, 98, 99]. The ability to trap and hold single proteins could enable single molecule experiments and single molecule patterning.

The triaxial probe geometry presented here can be modified to manipulate semiconductor nanowires which are candidates for for nanoelectronics, photonics, spintronics, and quantum information[100, 3]. A chisel shaped AFM probe can be used to create an elongated trap which is well suited to hold nanowires or carbon nanotubes. The electrode spacing can be modified from what is presented here to obtain the optimum trap shape. Smaller radius tips would have better spatial resolution and trap stiffness as an AFM while larger tips would allow for trapping of larger particles.

Chapter 8

Conclusions

In this thesis, we have presented the development and use of coaxial and triaxial AFM probes for imaging and manipulating nanoscale materials. Coaxial and triaxial AFM probes create highly localized electric fields at their tip which can be used for high resolution imaging and manipulating with dielectrophoresis. Here, we will briefly summarize our accomplishments and describe future directions for this work.

This work can be divided into discrete milestones which are each contained in a publication:

- The design of a fabrication protocol to create coaxial and triaxial AFM probes with electrode spacing from $\sim$ 30 nm up to several μm.[101]
- The development of a technique to use cantilevers with thin film capacitors on their surface to drive the mechanical modes of the cantilevers electrically with high fidelity.[102]

- The demonstration of enhanced spatial resolution Kelvin probe force microscopy using coaxial probes.[103]
- Imaging with the dielectrophoretic force and showing that a coaxial probe can be considered an electric dipole.[78]
- Pick-and-place manipulation of μm-scale objects using positive DEP with coaxial AFM probes.[79]
- Described a theoretical model to elucidate the capability of triaxial AFM probes to trap objects using negative DEP.[87, 86]
- Trapped a single nanoparticle in suspension using a triaxial AFM probe.[104]

8.1 Future Directions and Outlook

This work has focused on the development of coaxial and triaxial AFM probes and therefore most experiments were proof-of-principle. Many applications of these technologies involve taking the unique capabilities listed above and bring them to bear on systems in which they will have a high impact. Here, I present several promising directions for future work.

8.1.1 Self-driving cantilevers for high fidelity driving

In Chapter 4, we demonstrated high fidelity driving of the mechanical modes of cantilevers by electrostatically driving a capacitor on their surface. Two main reasons why this is superior to driving *via* a distant piezoelectric are: (1) The mechanical

power from a distant piezoelectric has to travel through the chip holder and AFM chip to reach the cantilever and the result is a transfer function that depends strongly on frequency f, especially at high drive frequencies $f \gtrsim 1$ MHz. (2) When a probe is driven while in liquid or in contact with a substrate, many spurious mechanical modes can be driven that complicate or disrupt the experiment. Direct capacitive driving is a promising candidate for driving cantilevers at high frequencies, in contact, and in liquids.

8.1.2 Electrostatic measurement of heterogenous materials

The electric field confinement afforded by coaxial probes gives them strong potential for enhancing the spatial resolution of any type of electrostatic force microscopy (EFM). Among the most widely used of EFM techniques is Kelvin probe force microscopy, a technique for measuring the local work function of surfaces. Work function is an especially important property of photovoltaics[105], semiconductor devices,[11, 75] and dopant profiling.[106] The ability to improve the spatial resolution of KPFM by an order of magnitude, as we have demonstrated in Chapter 5, has far reaching consequences.

One system in particular that will benefit greatly from enhanced resolution are bulk heterojunction photovoltaics.[105] In bulk heterojunction devices, acceptor and donor regions of polymer phase-separate to form domains on the same length scales as the carrier relaxation length, allowing most excitons to be separated to efficiently capture the energy of incident light. These materials are challenging to develop as they have electrical features on the 10 nm scale which dictate their operation.[105, 75]

The ability to accurately image the work function variation across these domains and their interfaces will much more readily allow the connection between nanoscopic form to macroscopic function.

8.1.3 Spectroscopic imaging with dielectrophoresis

Imaging with dielectrophoresis, as demonstrated in Chapter 6, is a powerful tool to enhance the spatial resolution and measure local dielectric properties. The electrostatic force is highly dependant on local dielectric properties[107] and conductivity.[108, 109] Spectroscopic measurements can be performed by imaging using the DEP force as contrast by varying the applied frequency in between scans. Imaging in this way is analogous to obtaining a "color" image of a sample by obtaining contrast at different frequencies. The range of available frequencies spans at least eight decades, the upper frequency limit $f \lesssim 1$ GHz is given by the RC roll off frequency of coaxial probes while the lower limit frequency $f \gtrsim 500$ Hz is dictated by the bandwidth of the cantilever .

8.1.4 Microscale pick-and-place and imaging

As described in Chapter 6, coaxial AFM probes can perform pick-and-assembly of microscale objects. One area where the positioning of microscale objects can fulfill a need is the positioning of biological cells. The Westervelt lab has previously used DEP to position many cells, drops, and vesicles using an integrated circuit,[110, 111] but the spatial resolution of this technique is limited by the feature size of CMOS processing. In contrast, the spatial resolution of AFM is sub-nanometer, offering

unprecedented control over the relative position of cells. This technique could be used for tissue assembly or the study of cell-cell interactions.

8.1.5 Nanoscale assembly of interacting quantum systems

A triaxial AFM could be used to localize a desired colloidal quantum dot or diamond nanoparticle and position it inside a desired photonic crystal to create multiple interacting quantum devices. There is great need for positioning single nanoparticles. A strong motivator for this is the recent successes in the strong coupling of photonic structures with single artificial atoms.[95] By colocalizing an optical cavity with a semiconductor quantum dot, it is possible to create an entangled state between excitons in the dot and photons in the cavity. This technique has potential for quantum information processing as photonic cavities can be readily fabricated with conventional means, but it remains difficult to position the cavity relative to the quantum dot. Recently, an effort has been made to construct similar photonic crystal / artificial atom structures by positioning diamond nanoparticles with AFM-based sliding[20] and dip-pen methods.[112] We have shown in Chapter 7 how triaxial probes can be used as a nanoscale had to grab and position single nanoscale particles. When used in combination with an AFM, triaxial probes constitute a powerful platform for assembly and sensing.

8.1.6 Multifunctional AFM probes

Triaxial AFM probes have the potential to act as a new class of multifunctional AFM probes. AFM probes have demonstrated wide versatility a multitude of ma-

terials being attached to the probe surface enabling imaging a specific property. Examples include bioparticles for imaging biological functionalization,[84] metallic nanoparticles for scanning near field optical imaging,[113] and nanotubes[114, 115] or nanoneedles[116] for high spatial resolution imaging. Triaxial probes add the ability to grab, image with, and release a specified nanoparticle, similar to techniques used in optical tweezing.[117, 118]

The ability to control the functionalization will greatly increase the capabilities of an AFM in a single experiment. A typical experiment could include a triaxial probe operating in a suspension of beads that are size-matched to the tip, as shown schematically in Figure 8.1. Each bead would be functionalized differently, and perhaps labeled with a particular fluorescent dye. A single particle is swept into the trap by applying a sequence of voltages as described in Figs 7.4(g) through 7.4(a). The presence and type of the bead can be verified with fluorescence microscopy. Once the bead is trapped it can be used to image or perform force spectroscopy.[119]

Another benefit of working with a particle held in a nDEP trap rather than attached to an AFM tip or cantilever is that it is free to rotate and move independently of the tip, which is very useful if the goal is to study the behavior of the particle in suspension.

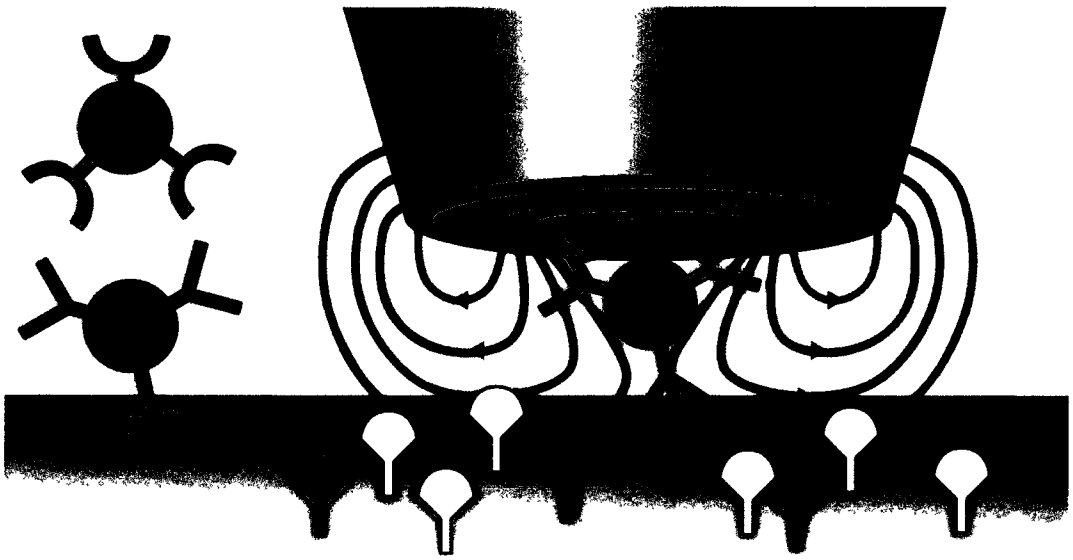

Figure 8.1: Schematic of a triaxial probe acting as a multifunctional probe. Here a triaxial probe is holding a nanoparticle that has been functionalized with an antibody that is specific to one of the antigens present on the surface. After imaging with this nanoparticle, the particle can be replaced with a particle with different functionalization by grabbing a different particle out of suspension.

Imaging the motion of a particle in the trap can either be done by measuring the deflection of the cantilever of measuring the lateral motion of the particle in the trap. The spring constant of a trapped particle can be inferred from its rms displacement in the trap and thus we find that for the triaxial probe presented in Chapter 7 with a 100 nm radius bead, $k \approx 4 \times 10^{-6}$ N/m, about five orders of magnitude less than a typical spring constant of a cantilever. Since the deflection of the cantilever depends on the two springs in series, if the spring constants are of similar magnitude, the motion of the particle can be inferred from watching the cantilever. For a smaller cantilever with $\lambda = 100$ nm driven with 10 V we expect $k \approx 10^{-1}$ N/m as $k \propto \lambda^2$, this spring constant is the same magnitude of the spring constant of cantilevers used in biological applications. Alternatively, the particle can be adhered to the tip to

image without an applied electric field and directly observe the deflection of the cantilever. Finally, the lateral deflection of the bead could be observed optically, in a close analogue to optical tweezer force spectroscopy experiments, except with triaxial AFM probes, the trap size is not diffraction limited.

8.2 Concluding Remarks

Coaxial and triaxial AFM probes provide a host of new capabilities that are fully compatible with the well established AFM techniques that have already played an enormous role in nanotechnology. The next step is the transition from proof-of-principle experiments to performing relevant scientific studies, such as those listed in Section 8.1. The fabrication necessary to produce coaxial and triaxial probes is complex but no more so than what is already necessary to create commercial AFM probes, so the large-scale commercial fabrication of these probes is a possibility. Coaxial and triaxial AFM probes can provide new avenues of imaging and manipulating nanoscale materials to augment the capabilities of AFM.

Bibliography

[1] Technology Working Group. International technology roadmap for semiconductors. Technical report, 2010. Manual Citation.

[2] C.B. Murray, C.R. Kagan, and M. G. Bawendi. Synthesis and characterization of monodisperese nanocrystals and close-packed nanocrystal assemblies. *Annu. Rev. Mater. Sci*, 30, 2000.

[3] C. Thelander, P. Agarwal, S. Brongersma, J. Eymery, L.F. Feiner, A. Forchel, M. Scheffler, W. Riess, B.J. Ohlsson, U. Gosele, and L. Samuelson. Nanowire-based one-dimensional electronics. *Materials Today*, 9, 2006.

[4] F.J. Giessibl. Advances in atomic force microscopy. *Reviews of Modern Physics*, 75, 2003.

[5] G. Binning, C.F. Quate, and C. Gerber. Atomic force microscope. *Physical Review Letters*, 56, 1986.

[6] N. Nonnenmacher, M.P. O'Boyle, and H.K. Wickramasinghe. Kelvin probe force microscopy. *Applied Physics Letters*, 58, 1991.

[7] C. Daniel Frisbie, Lawrence F. Rozsnyai, Aleksandr Noy, Mark S. Wrighton. and Charles M. Lieber. Functional group imaging by chemical force microscopy. *Science*, 265, 1994.

[8] C.L. Degen. M. Poggio, H.J. Mamin, C.T. Rettner, and D. Rugar. Nanoscale magnetic resonance imaging. *PNAS*, 106, 2009.

[9] P. Girard. Electrostatic force microscopy: principles and some applications to semiconductors. *Nanotechnology*, 12, 2001.

[10] S.V. Kalinin, R. Shao, and D.A. Bonnell. Local phenomena in oxides by advanced scanning probe microscopy. *J. Am. Ceram. Soc.*, 88, 2005.

[11] R.A. Oliver. Advances in afm for the electrical characterization of semiconductors. *Rep. Prog. Phys.*, 71, 2008.

[12] S.V. Kalinin and D.A. Bonnell. Imaging mechanism of piezoresponse force microscopy of ferroelectric surfaces. *Phys Rev B Condens Matter*, 65, 2002.

[13] S.V. Kalinin and D.A. Bonnell. Scanning impedance microscopy of electroactive interfaces. *Applied Physics Letters*, 78, 2001.

[14] S. Belaidi, F. Lebon, P. Girard, G. Leveque, and S. Pagano. Finite element simulations of the resolution in electrostatic force microscopy. *Appl. Phys. A*, 66, 1998.

[15] D.S.H. Charrier, M. Kemerink, B.E. Smalbrugge, T. de Vries, and R.A.J. Janssen. Real versus measured surface potentials in scanning kelvin probe microscopy. *ACS Nano*, 2, 2008.

[16] D. M. Eigler and E.K. Schweizer. Positioning single atoms with a scanning tunneling microscope. *Nature*, 344, 1990.

[17] C. Baur, A. Bugacov, B.E. Koel, A. Madhukar, N. Montoya, T.R. Ramachandran, A.A.G. Requicha, and P. Will. Nanoparticle manipulation by mechanical pushing: underlying phenomena and real-time monitoring. *Nanotechnology*, 9, 1998.

[18] T. Junno, S.B. Carlsson, H. Xu, L. Montelius, and L. Samuelson. Fabrication of quantum devices by angstrom-level manipulation of nanoparticles with an atomic force microscope. *Applied Physics Letters*, 72, 1998.

[19] A. A. G. Requicha. Nanorobots, nems, and nanoassembly. *Proceedings of the IEEE*, 91, 2003.

[20] M. Barth, N. Nsse, B. Lchel, and O. Benson. Controlled coupling of a single-diamond nanocrystal to a photonic crystal cavity. *Optics Letters*, 34, 2009.

[21] A. A. Tseng, A. Notargiacomo, and T. P. Chen. Nanofabrication by scanning probe microscope lithography: A review. *J. Vac. Sci. Technol. B*, 23, 2005.

[22] R. D. Piner, J. Zhu, F. Xu, S. Hong, and C. A. Mirkin. "dip-pen" nanolithography. *Science*, 283, 1999.

[23] K. Salaita, Y. Wang, and C. A. Mirkin. Applications of dip-pen nanolithography. *Nature Nanotechnology*, 2, 2007.

[24] H. Xie, D.S. Haliyo, and S Régnier. Parallel imaging/manipulation force microscopy. *Applied Physics Letters*, 94, 2009.

[25] H. Xie, D. S. Haliyo, and S. R´gnier. A versatile atomic force microscope for three-dimensional nanomanipulation and nanoassembly. *Nanotechnology*, 20, 2009.

[26] L.-O. Heim, J. Blum, M. Preuss, and H.J. Butt. Adhesion and friction forces between spherical micrometer-sized particles. *Physical Review Letters*, 83, 1999.

[27] K.L. Johnson. Mechanics of adhesion. *Tribology International*, 31, 1999.

[28] Y.I. Rabinovich, J.J. Adler, M.S. Esayanur, A. Ata, R.K. Singh, and B.M. Moudgil. Capillary forces between surfaces with nanoscale roughness. *Advances in Colloid and Interface Science*, 96, 2002.

[29] K. Komvopoulos. Adhesion and friction forces in microelectromechanical systems: mechanisms, measurement, surface modification techniques, and adhesion theory. *J. Adhesion Sci. Technol.*, 17, 2003.

[30] D.W.v.d. Weide. Localized picosecond resolution with a near-field microwave/scanning-force microscope. *Applied Physics Letters*, 70, 1997.

[31] B.T. Rosner and D.W v.d. Weide. High-frequency near-field microscopy. *Review of Scientific Instruments*, 73, 2002.

[32] M. Tabib-Azar and Y. Wang. Design and fabrication of scanning near-field microwave probes compatible with atomic force microscopy to image embedded nanostructures. *IEEE*, 52, 2004.

[33] K. Lai, M. Nakamura, W. Kundhikanjana, Masashi Kawasaki, Y. Tokura, M.A. Kelly, and Z.X. Shen. Mesoscopic percolating resistance network in a strained manganite thin film. *Science*, 329, 2010.

[34] David P. Burt, N.R. Wilson, J.M.R. Weaver, P.S. Dobson, and J.V. Macpherson. Nanowire probes for high resolution combined scanning electrochemical microscopy - atomic force microscopy. *Nano Lett*, 5, 2005.

[35] B.J. Rodriguez, S. Jesse, K. Seal, A.P. Baddorf, S.V. Kalinin, and P.D. Rack. Fabrication, dynamics, and electrical properties of insulated scanning probe microscopy probes for electrical and electromechanical imaging in liquids. *Applied Physics Letters*, 91, 2007.

[36] P.L.T.M. Frederix, P.D. Bosshart, T. Akiyamma, M. Chami, M.R. Gullo, J.J. Blackstock, K. Dooleweerdt, N.F.d. Rooij, U. Staufer, and A. Engel. Conductive supports for combined afmsecm on biological membranes. *Nanotechnology*, 19, 2008.

[37] J.H. Noh, M. Nikiforov, S.V. Kalinin, A.A. Vertegel, and P.D. Rack. Nanofabrication of insulated scanning probes for electromechanical imaging in liquid solutions. *Nanotechnology*, 21, 2010.

[38] O.Y. Loh, A.M. Ho, and Rim. Electric field-induced direct delivery of proteins by a nanofountain probe. *PNAS*, 105, 2008.

[39] T. P. Hunt and R. M. Westervelt. Dielectrophoresis tweezers for single cell manipulation. *Biomed Microdevices*, 2006.

[40] J.A. Aguilar, T. P. Hunt, A.C. Bleszynski-Jayich, and R. M. Westervelt. Atomic force microscope tip for dielectrophoresis. In *American Physical Society, APS March Meeting*, Denver, CO, 2007.

[41] U. Rabe, K. Janser, and W. Arnold. Vibrations of free and surface-coupled atomic force microscope cantilevers: Theory and experiment. *Review of Scientific Instruments*, 67, 1996. Manual Citation.

[42] John E. Sader, J.W.M. Chon, and P. Mulvaney. Calibration of rectangular atomic force microscope cantilevers. *Review of Scientific Instruments*, 70, 1999.

[43] R. García and R. Pérez. Dynamic atomic force microscopy methods. *Surface Science Reports*, 47, 2002.

[44] H.A. Haus and J.R. Melcher. *Electromagnetic Fields and Energy*, volume 1. Prentice-Hall, Englewood Cliffs, New Jersey, 1989.

[45] A. Castellanos, A. Ramos, A. Gonzlez, N.G. Green, and H. Morgan. Electrohydrodynamics and dielectrophoresis in microsystems: scaling laws. *J. Phys. D: Appl Phys.*, 36, 2003.

[46] D.J Griffiths *Introduction to Electrodynamics.* Prentice Hall. Upper Saddle River, New Jersey, 3 edition, 1999.

[47] X. Wang, X.-B. Wang, and P. R. C. Gascoyne. General expressions for dielectrophoretic force and electrorotational torque derived using the maxwell stress tensor method. *Journal of Electrostatics*, 39, 1997.

[48] T. Heinzel. Mesoscopic electronics in solid state nanostructures. Wiley-VCH, 2007.

[49] R. Pethig and G. H. Markx. Applications of dielectrophoresis in biotechnology. *Trends Biotechnol*, 15, 1997.

[50] X-.B. Wang, Y. Huang, F. F. Becker, and P.R.C. Gascoyne. A unified theory of dielectrophoresis and traveling wave dielectrophoresis. *J. Phys. D: Appl Phys.*, 27, 1994.

[51] I. Ermolina and H. Morgan. The electrokinetic properties of latex particles: comparison of electrophoresis and dielectrophoresis. *Journal of Colloid and Interface Science*, 285, 2005.

[52] R. Jones, H.M. Pollock, J.A.S. Cleaver, and S.H. Hodges. Adhesion forces between glass and silicon surfaces in air studied by afm: Effects of relative humidity, particle size, roughness, and surface treatment. *Langmuir*, 18, 2002.

[53] A Ramos, H. Morgan, G. Green, N, and A Castellanos. Ac electric-field-induced fluid flow in microelectrodes. *Journal of Colloid and Interface Science*, 217, 1999.

[54] D. Stryahilev, A. Sazonov, and A. Nathan. Amorphous silicon nitride deposited at 120c for organic light emitting display-thin film transistor arrays on plastic substrates. *J. Vac. Sci. Technol. A*, 20, 2002.

[55] A. Wallash and L. Levit. Electrical breakdown and esd phenomena for devices with nanometer-to-micron gaps. *SPIE proceedings series*, 4980, 2003.

[56] J.F. Kolb, R.P. Joshi, S. Xiao, and K.H. Schoenbach. Streamers in water and other dielectric liquids. *J. Phys. D: Appl Phys.*, 41, 2008.

[57] M. Li, H.X. Tang, and M.L. Roukes. Ultra-sensitive nems-based cantilevers for sensing, scanned probe and very high-frequency applications. *Nature Nanotechnology*, 2:7, 2007. Manual Citation.

[58] S.C. Minne, S.R. Manalis, and C.F. Quate. Parallel atomic force microscopy using cantilevers with integrated piezoresistive sensors and integrated piezoelectric actuators. *Applied Physics Letters*, 67, 1995.

[59] K. Schwarz, U. Rabe, S. Hirsekorn, and W. Arnold. Excitation of atomic force microscope cantilever vibrations by a schottky barrier. *Applied Physics Letters*, 92, 2008.

[60] S.S. Rao. *Mechanical Vibrations*. Addison-Wesley Publishing Company, 3 edition, 1995.

[61] I Krakovský, T Romijn, and A. Posthuma de Boer A few remarks on the electrostriction of elastomers. *Journal of Applied Physics*, 85, 1999.

[62] Y.M. Shkel and J. Klingenberg. Electrostriction of polarizable materials: Comparison of models with experimental data. *Journal of Applied Physics*, 83, 1997.

[63] H.Y. Lee, Y. Peng, and Y.M. Shkel. Strain-dielectric response of dielectrics as foundation for electrostriction stresses. *Journal of Applied Physics*, 98, 2005.

[64] P.R. Scheeper, J.A. Voorthuyzen, and P. Bergveld. Pecvd silicon nitride diaphragms for condenser microphones. *Sensors and Actuators B*, 4, 1991.

[65] K.D. Mackenzie, D.J. Johnson, M.W. DeVre, R.J. Westerman, and B.H. Reelfs. Stress control of si-based pecvd dielectrics. *Proc. Symp. Silicon Nitride and Silicon Dioxide Thin Insulating Films & Other Emerging Dielectrics VIII*, PV2005-01, 2005.

[66] Michael P. Hughey and Robert F. Cook. Stress development kinetics in plasma-enhanced chemical-vapor-deposited silicon nitride films. *Journal of Applied Physics*, 97, 2005.

[67] M.T. Cuberes, H.E. Assender, G.A.D. Briggs, and O.V. Kolosov. Heterodyne force microscopy of pmma/rubber nanocomposites: nanomapping of viscoelastic response at ultrasonic frequencies. *J. Phys. D: Appl Phys.*, 33, 2000.

[68] H.O. Jacobs, H.F. Knapp, and A. Stemmer. Practical aspects of kelvin probe force microscopy. *Review of Scientific Insruments*, 70, 1999.

[69] S. Belaidi, P. Girard, and G. Leveque. Electrostatic forces acting on the tip in atomic force microscopy: Modelization and comparison with analytic expressions. *J. Appl. Phys.*, 81, 1997.

[70] N.A. Surplice and R.J. D'Arcy. A critique of the kelvin method of measuring work functions. *Journal of Physics E: Scientific Instruments*, 3, 1970.

[71] I.D. Baikie, E. Venderbosch, J.A. Meyer, and P.J. Estrup. Analysis of stray capacitance in the kelvin method. *Review of Scientific Instruments*, 62, 1991.

[72] W. Nabhan, A. Broniatowski, G. De Rosny, and B. Equer. Design and implementation of a kelvin microprobe for contact potential measurements at the submicron scale. *Microsc. Microanal. Microstruct.*, 5, 1994.

[73] W. Nabhan, B. Equer. A. Broniatowski, and G. De Rosny. A high-resolution scanning kelvin probe microscope for contact potential measurements on the 100 nm scale. *Rev. Sci. Instrum.*, 68, 1997.

[74] X.D. Ding, J. An, J.B. Xu, C. Li, and R.Y. Zheng. Improving lateral resolution of electrostatic force microscopy by mltifrequency method under ambient conditions. *Applied Physics Letters*, 94, 2009.

[75] Justin L. Luria, K.A. Schwarz, M.J. Jaquith, R.G. Hennig, and John A. Marohn. Spectroscopic characterization of charged defects in polycrystalline pentacene by time- and wavelength-resolved electric force microscopy. *Adv. Mater.*, 23, 2010.

[76] S. Cunningham, I.A. Larkin, and J.H. Davis. Noncontact scanning probe microscope potentiometry of surface charge patches: Origin and interpretation of time-dependent signals. *Applied Physics Letters*, 73, 1998.

[77] G.N. Parsons, J.H. Souk, and J. Batey. Low hydrogen content stoichiometric silicon nitride films deposited by plasma-enhanced chemical vapor deposition. *Journal of Applied Physics*, 70, 1991.

[78] K.A. Brown, J. Berezovsky, and R. M. Westervelt. Coaxial atomic force microscope probes for imaging with dielectrophoresis. *Applied Physics Letters*, Accepted, 2011.

[79] K.A. Brown, J.A. Aguilar, and R. M. Westervelt. Coaxial atomic force microscope tweezers. *Applied Physics Letters*, 96, 2010.

[80] D.T. Edmonds. The different screening of electric charges and dipoles near a dielectric interface. *Eur Biophys J*, 16, 1988.

[81] C.-C. Lee and W. Hsu. Method on surface roughness modification to alleviate stiction of microsctructures. *J. Vac. Sci. Technol. B*, 21, 2003.

[82] R. Beach, E, G.W. Tormoen, J. Drelich, and R. Han. Pull-off force measurements between rough surfaces by atomic force microscopy. *Journal of Colloid and Interface Science*, 247, 2002.

[83] B. Cappella, P. Baschieri, C. Frediani, P. Miccoli, and C. Ascoli. Force-distance curves by afm. *IEEE*, 1997.

[84] D.J. Müller and Y.F. DuFrêne. Atomic force microscopy as a multifunctional molecular toolbox in nanobiotechnology. *Nature Nanotechnology*, 3:261–269, 2008. Great reveiw of functional Afm probes for bio.

[85] T.B. Jones and G.W. Bliss. Bubble dielectrophoresis. *Journal of Applied Physics*, 48, 1977.

[86] K.A. Brown and R. M. Westervelt. Nanoscale pick-and-place. *NanoTechWeb.org*, Nov 3 2009.

[87] K.A. Brown and R. M. Westervelt. Proposed triaxial atomic force microscope contact-free tweezers for nanoassembly. *Nanotechnology*, 20. 2009.

[88] C. MeiMeinhart2003nhart, D. Wang, and K. Turner. Measurement of ac electrokinetic flows. *Biomed Microdevices*, 5, 2003.

[89] W.M. Deen. *Analysis of Transport Phenomena.* Oxford University Press, New York, New York, 1998.

[90] F. Reif. *Fundamentals of statistical and thermal physics.* McGraw-Hill Companies, Boston, MA, 1965.

[91] R.C. Weast. *CRC Handbook of Chemistry and Physics.* CRC Press Inc., Boca Raton, Florida, 1986.

[92] G. Akerlof. Dielectric constants of some organic solvent-water mixtures at various temperatures. *J Am Chem Soc*, 54, 1932.

[93] L. Cui, D. Holmes, and H. Morgan. The dielectrophoretic levitation and separation of latex beads in microchips. *Electrophoresis*, 22, 2001.

[94] F. Zhang, J. Xu, A. Lakhtakia, S.M. Pursel, and M.W. Horn. Circularly polarized emission from colloidal nanocrystal quantum dots confined in microcavities formed by chiral mirrors. *Applied Physics Letters*, 91, 2007.

[95] K. Hennessy, A. Badolato, M. Winger, D. Gerace, M. Atature, S. Gulde, S. Falt, E. L. Hu, and A. Imamoglu. Quantum nature of a strongly coupled single quantum dot-cavity system. *Nature*, 445, 2007.

[96] L. Zheng, J.P. Brody, and P.J. Burke. Electronic manipulation of dna, proteins, and nanoparticles for potential circuit assembly. *Biosensors and Bioelectronics*, 20, 2004.

[97] G. Loffler, H. Schreiber, and O. Steinhauser. Calculation of the dielectric properties of a protein and its solvent: Theory and a case study. *J. Mol. Biol.*, 270, 1997.

[98] S. Hofinger and T. Simonson. Dielectric relaxation in proteins: A continuum electrostatics model incorporating dielectric heterogeneity of the protein and time-dependent charges. *Journal of Computational Chemistry*, 22, 2001.

[99] A. Knocks and H. Weingartner. The dielectric spectrum of ubiquitin in aqueous solution. *J. Phys. Chem. B*, 105, 2001.

[100] Y. Li, F. Qian, J. Xiang, and C. M. Lieber. Nanowire electronic and optoelectronic devices. *Materials Today*, 9, 2006.

[101] K.A. Brown and R. M. Westervelt. Fabrication of triaxial and coaxial afm probes. *In Preparation*, 2011.

[102] K.A. Brown and R. M. Westervelt. Self-driving capacitive cantilevers for dynamic atomic force microscopy. *In Preparation*, 2011.

[103] K.A. Brown, K.J. Satzinger, and R. M. Westervelt. High spatial resolution kelvin probe force microscopy with coaxial probes. In Preparation, 2011.

[104] K.A. Brown and R. M. Westervelt. Triaxial afm probes for non-contact trapping and manipulation. In Preparation, 2011.

[105] H. Hoppe, T. Glatzel, M. Niggemann, A. Hinsch, M.Ch. Lux-Steiner, and N.S. Sariciftci. Kelvin probe force microscopy study on conjugated polymer/fullerene bulk heterojunction organic solar cells. *Nano Lett*, 5, 2005.

[106] C. Baumgart, M. Helm, and H. Schmidt. Quantitative dopant profiling in semiconductors: A kelvin probe force microscopy model. *Phys Rev B Condens Matter*, 80, 2009.

[107] M. Salmeron. Scanning polarization force microscopy a technique for studies of wetting phenomena at the nanometer scale. *Oil Gas Sci. Technol.*, 56, 2001.

[108] M. Bockrath, N. Markovic, A. Shepard, M. Tinkham, L. Gurevich, L.P. Kouwenhoven, M.W. Wu, and L.L. Sohn. Scanned conductance microscopy of carbon nanotubes and lambda-dna. *Nano Lett*, 2, 2002.

[109] O. Cherniavskaya, L. Chen, V. Weng, L. Yuditsky, and L.E. Brus. Quantitative noncontact electrostatic force imaging of nanocrystal polarizability. *J. Phys. Chem. B*, 107, 2003.

[110] T. P. Hunt, D. Issadore, and R. M. Westervelt. Integrated circuit/microfluidic chip to programmably trap and move cells and droplets with dielectrophoresis. *Lab Chip*, 8, 2008.

[111] D. Issadore, T. Franke, K.A. Brown, and R. M. Westervelt. A microfluidic microprocessor: Controlling biomimetic containers and cells using hybrid integrated circuit / microfluidic chips. *Lab Chip*, 10, 2010.

[112] O. Loh, R. Lam, M. Chen, N. Moldovan, H. Huang, D. Ho, and H.D. Espinosa. Nanofountain-probe-based high-resolution patterning and single-cell injection of functionalized nanodiamonds. *Small*, 5, 2009.

[113] Y. Gan. Invited review article: A review of techniques for attaching micro- and nanoparticles to a probes tip for surface force and near-field optical measurements. *Review of scientific instruments*, 78, 2007.

[114] J.H. Hafner, C.-L. Cheung, A.T. Woolley, and C. M. Lieber. Structural and functional imaging with carbon nanotube afm probes. *Progress in Biophysics & Molecular Biology*, 77, 2001.

[115] M. Zhao, V. Sharma, H. Wei, R.R. Birge, J.A. Stuart, F. Papdimitrakopoulos, and B.D. Huey. Ultrasharp and high aspect ratio carbon nanotube atomic force microscopy probes for enhanced surface potential imaging. *Nanotechnology*, 19, 2008.

[116] M.M. Yazdanpanah, S.A. Harfenist, A. Safir, and R.W. Cohn. Selective self-assembly at room temperature of individual freestanding ag2ga alloy nanoneedles. *Journal of Applied Physics*, 98, 2005.

[117] D.G. Grier. A revolution in optical manipulation. *Nature*, 424, 2003.

[118] J.R. Moffitt, Y.R. Chemla, S.B. Smith, and C. Bustamante. Recent advances in optical tweezers. *Annu. Rev. Biochem.*, 77, 2008.

[119] K. C. Neuman and A. Nagy. Single-molecule force spectroscopy: optical tweezers, magnetic tweezers and atomic force microscopy. *Nature Methods*, 5, 2008.